National Library of Canada
Canadian Theses Service

Ottawa, Canada
K1A 0N4

Bibliothèque nationale du Canada
Service des thèses canadiennes

ISBN 0-315-54970-X

CIRCULAR POLARIZATION FROM A CIRCULAR ARRAY OF LINEARLY POLARIZED RECTANGULAR PATCHES WITH ONE END SHORTED

by

Marc G. W. Opie

A Thesis
Submitted to the Faculty of Graduate Studies
In partial Fulfillment of the Requirements of
the Degree of Master of Science

University of Manitoba
Department of Electrical Engineering
Winnipeg, Manitoba
Canada

July 1989

CIRCULAR POLARIZATION FROM A CIRCULAR ARRAY OF LINEARLY POLARIZED RECTANGULAR PATCHES WITH ONE END SHORTED

BY

MARC G.W. OPIE

A thesis submitted to the Faculty of Graduate Studies of
the University of Manitoba in partial fulfillment of the requirements
of the degree of

MASTER OF SCIENCE

Abstract

This thesis is concerned with the generation of a circularly polarized wave from a circular array of linearly polarized elements. The elements used for this work are rectangular microstrip patch antennas with one end shorted to the ground plane. The patches are investigated theoretically and experimentally for such characteristics as radiation pattern, beam width, side lobe level, input impedance and bandwidth. Experimentally, a four element array is used to generate a circularly polarized wave, while theoretically various numbers of elements are used in the array and investigated in varying configurations.

Acknowledgements

I would like to express my thanks to Dr. L. Shafai, for his guidance during the preparation of this thesis. I would also like to acknowledge my appreciation to Brad Tabachnik for his help during the experimental phases of the work, and to Krzsztof Antoszkiewicz for his advice in the laboratory.

Table of Contents

List of Figures

4.12 Experimental rotating linear radiation patterns for the dimensions listed

4.13 Theoretical radiation patterns for the dimensions listed above

4.14 Theoretical radiation patterns for the dimensions listed above

4.15 Theoretical radiation patterns for the dimensions listed above

Chapter 1

Introduction

1.1 Microstrip Antennas

Microstrip circuits have been in use since the 1950's, while the idea of using a microstrip patch as a radiator has been around since the early seventies. Prior to this, radiation from a microstrip circuit due to discontinuities has been considered undesirable. Wheeler [1] has done much work in the analysis of microstrip circuits, providing the root theory behind most of the models and equations of microstrip circuits and microstrip antennas.

A microstrip patch is an planar electric conductor of arbitrary shape, suspended a height h above a ground plane by a substrate of dielectric constant ε_r as shown in Fig. 1.1. The shapes most often used, and those for which detailed analytical and experimental analyses exist are circular, elliptical, rectangular, annular, and triangular. The present work involves the study of a rectangular patch modified to include a short circuit at one end.

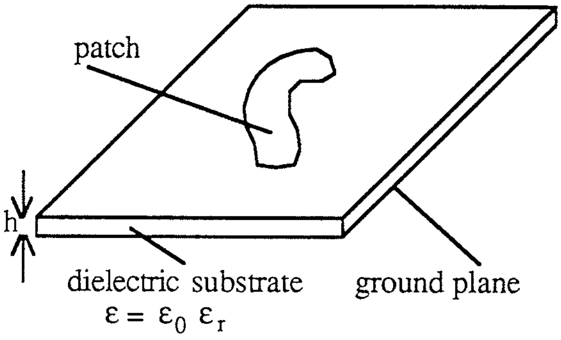

Figure 1.1 A general microstrip patch radiator.

The first model of a microstrip patch as a radiating element was that of a cavity formed by two parallel planar electric conductors of arbitrary shape in the xy-plane [2], separated by a height h with a perpendicular "magnetic wall" occupying the periphery or aperture formed by the two electric conductors (Fig. 1.2).

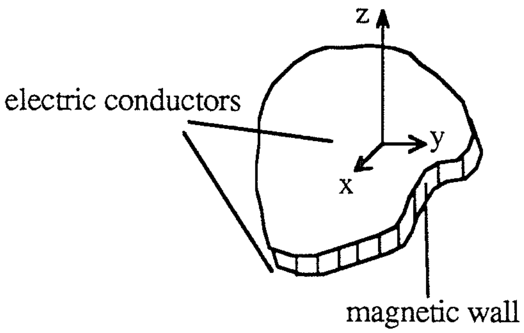

Figure 1.2 Cavity model of the microstrip patch.

The underlying assumption in this model is a z-directed electric field, $E_z(x,y)$, which reaches its maximum at the periphery (with respect to a direction perpendicular to the periphery), resulting in a zero tangential magnetic field (and thus a magnetic wall or magnetic conductor). An additional assumption is an electric field which is invariant in the z direction for values of h which are sufficiently smaller than one wavelength ($\leq .1\ \lambda$).

This model is accurate for calculations of the radiation pattern of the patch, as will be discussed in Chapter 2, but cannot be used to determine the resonant frequency, or the input impedance of the patch. Both of these require a knowledge of the power radiated through the so called aperture, and the effects of the fringing electric field at the aperture and the presence of the current probe used to excite the patch.

Many refinements have been made to the cavity model of the microstrip patch, to account for the effect of the aperture, and the deviations it causes from the pure cavity model. These deviations are the result of:

1) Power flowing through the aperture and radiating into space,

2) The inhomogeneity of the problem (the dielectric does not occupy all of space), which results in a resonant frequency and an input impedance, which depend on an "effective" dielectric constant whose value depends on the geometry of the problem, and on the true dielectric of the substrate, and

3) The wave structure in the region beneath the patch will not be purely TEM (considering the patch as a transmission line discussed below).

Wheeler [1] attempted to account for 2) in a paper using conformal mapping. The analysis was not done on a microstrip patch since there was no ground plane, however, the mircostrip patch over an infinite ground plane may be replaced by two microstrips using image theory. Wolff and Knoppik [3] attempted to bridge the difference between Wheeler's work and a microstrip patch over a ground plane.

Another model used for the microstrip patch, is to treat it as a transmission line, with a characteristic impedance, a velocity of propagation, and an inductance and capacitance per unit length. The jump from a cavity model to a transmission line model is a natural step for a rectangular patch, whose characteristics are invariant with the direction of propagation of the travelling waves. For an annular shaped patch however, the jump is not as natural and certain modifications to the concepts of line voltage and line current must be made. Bhattacharrya [4] has made the necessary modifications.

When treating the patch as a transmission line, the parameters of the line, such as phase velocity and wave impedance must be defined in terms of the patch geometry and the value of ε_r. Were it not for the inhomogeneity of the dielectric medium (the substrate does not exist over all space), the structure would be readily analyzed, and would be capable of supporting a pure TEM wave. If the substrate occupied all of the space, the expressions for the wave impedance and phase velocity would be

$$v_d = \frac{c}{\sqrt{\varepsilon_r}}, \text{ and } Z_d = \frac{\eta_0}{\sqrt{\varepsilon_r}}$$

where c = velocity of light in free space

η_0 = impedance of free space

When the substrate fills only part of the space, the values for v_d and Z_d lie somewhere between the values obtained using the above expressions with ε_r set to the dielectric constant of the substrate (as if the substrate occupied all space), and the values obtained by setting ε_r to unity (free space everywhere).

Despite the electrical disadvantages of microstrip antennas, there has been a great deal of interest in them in the past twenty years. The reason for this interest lies in the mechanical characteristics of microstrip antennas. They are light weight, have a low profile, and can be made to conform to objects' surfaces (suitable for mounting on airborne vehicles). In addition to this, they are easily and cheaply constructed. Where they fail is in their electrical characteristics, and it is towards improving these characteristics that the majority of the research has been devoted. Microstrip antennas, due to their cavity nature are inherently low bandwidth devices, at least with respect to their input impedance. In general the larger the substrate thickness, the smaller the Quality factor, and hence the larger the bandwidth. This is easily seen as the Q factor is related to the ratio between the energy stored in the region beneath the patch, and the power dissipated (through dielectric losses or copper losses), and radiated. For a given voltage applied across the length of a current probe, the electric field strength will vary inversely with the substrate thickness, h, and the energy density will vary inversely with the square of h (since energy density is proportional to the square of the electric field strength). The volume of the region between the patch and the ground plane will of course be proportional to h, and hence the total energy stored beneath the patch will vary as the reciprocal of h. The radiated power, which is in general much greater than the dissipated power is insensitive to the value of h. Increasing h has the opposing effects of decreasing the strength of the electric field at the aperture (and therefore, as will be shown in Chapter 3, decreasing the fictitious magnetic current density along the aperture), and increasing the size of the aperture. Thus the total magnetic current will be the same, and the power flow through the aperture will remain unchanged as h is increased. The Q factor therefore depends almost entirely on the energy stored under and in a region around the patch. Thus one method of improving the bandwidth of the microstrip patch antenna is to increase the thickness, h, thereby decreasing the energy stored under the patch.

1.2 The Rectangular Microstrip Antenna with One End Shorted

The type of microstrip antenna, or patch, selected for this work is a rectangular one with one end shorted, as shown in Fig. 1.3. The dimensions of the antenna are shown as having width a, length b, and a substrate thickness h. (Note that the substrate is not shown in Fig. 1.3, it lies between the patch and the ground plane). Now consider a rectangular microstrip antenna of the same width, but twice the length, with no short as shown in Fig. 1.4. For the larger patch, it may be noted that for the odd modes the field is zero at the centre of the patch, and hence a short may be placed there. Thus it may be concluded that the smaller patch is equivalent to the larger patch excited with the odd modes and only half of the patch radiating.

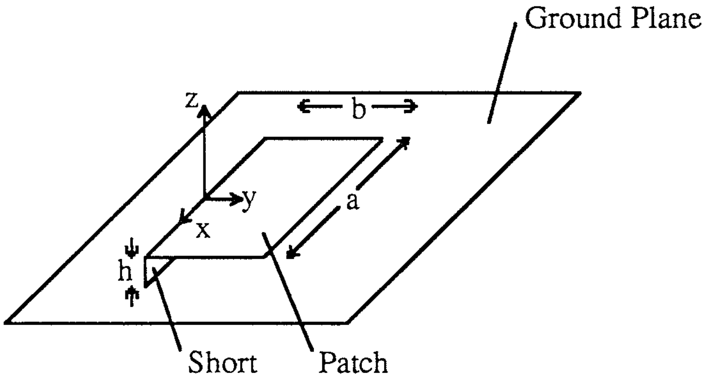

Figure 1.3 Rectangular patch with one end shorted.

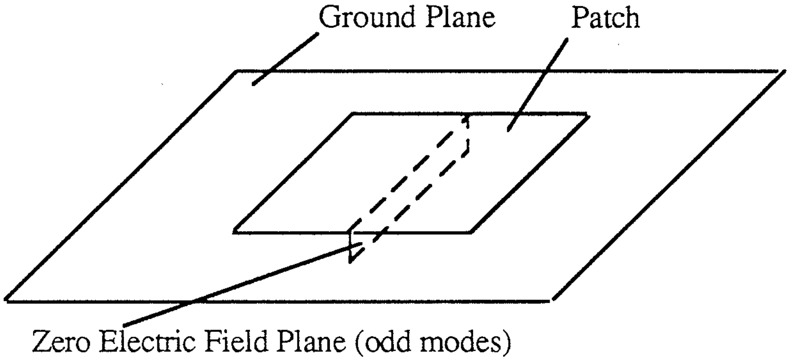

Figure 1.4 Rectangular patch showing plane of zero electric field for odd modes.

1.3 Circular Polarization

The object of the present work is to obtain a circularly polarized propagating wave using only microstrip patches which generate linearly polarized propagating waves. As will be discussed in detail in Chapter 4, a linearly polarized wave is a wave whose fields oscillate sinusoidally in only one direction, while a circularly polarized wave is one in which two spatially independent fields, both in the plane perpendicular to the direction of propagation, oscillate in phase quadrature to produce the wave.

Huang [5] has shown that good circular polarization (as discussed in Chapter 4) in the principal planes may be obtained in a four element circular array of linearly polarized elements by feeding the elements with a phasing of 0°, 90°, 0°, 90°, or 0°, 90°, 180°, 270°. In the boresight direction ($\theta = 0°$), the axial ratio will be exactly unity.

The principle applied is that of feeding two elements which are in spatial quadrature with a phasing also in quadrature. The elements will thus produce field vectors which are also in both spatial quadrature (in the plane of the array), and phase quadrature.

1.4 Scope of the Present Work

In the present work the individual patches are tested theoretically and experimentally for their input impedance as a function of frequency. The antennas are operated in the lowest order mode, TE_{01}, where there is no variation in the field along the width of the patch, and a sinusoidal variation along the length of the patch (in general if the patch is operated in the TE_{nm} mode, the expression for the electric field is $E_z(x,y) = A_{nm} \cos (\frac{n\pi}{a}x) \sin (\frac{(2m-1)\pi}{b}y)$). To determine the input impedance of the patch antenna, the mode method is used, which requires an exact solution of the field structure under a patch, accounting for the presence of the current probe used to feed the patch, with the assumption that the magnetic field variation in the x-direction is minimum at the sides of the patch, (and thus no radiation of power takes place through the sides of the patch, i.e. the aperture admittance is zero). In the mode method it is assumed that all modes are present under the patch. There are three boundary conditions which are satisfied by each of the modes (the short circuit at one end of the patch, the radiating aperture at the other end, and the open circuits at the two sides), and a fourth satisfied collectively by the modes (the presence of an electric current due to the probe). Once the values of A_{nm} have been determined for all values of n and m, the electric field at the probe is determined by summing each mode.

The mode method is attempted using two types of probe feeds which lead to analytic solutions of the electric field. The first type is an infinitely thin probe, carrying a current I_0, which requires an infinite current density at the location of the probe. The electric field required to support this condition is also infinite at the probe, with the result that the reactive portion of the calculated impedance is infinite. This is of course what must occur since the inductance of an infinitely thin probe is itself infinite. In order to better estimate the impedance of the probe-fed patch, the imaginary part of the resulting series is truncated after one term, while the real part (which converges), is not. To account for the impedance of a probe of finite thickness, the impedance evaluated by truncating the series is added to the approximate expression for the impedance of the probe.

The second type of feed used is a infinitely thin strip running along the width of the patch. The current in the strip is equal to I_0, while the width of the strip is set equal to the circumference of the probe used in the experiments.

Theoretical results are evaluated over a range of frequencies, as well as for various locations of the probe, and compared with the experimental measurements.

The radiation patterns for a circular array of the antennas are calculated for a variety of configurations. The parameters of interest are the number of the antenna's elements in the array, the spatial and feeding arrangements of the elements, the distance of the elements from the origin, etc. The radiation patterns are plotted and examined for gain, beamwidth, and quality of circular polarization. The theoretical calculations are based on the cavity model of the patch, excited in the lowest order mode.

Experimentally the antennas are tested for a restricted number of configurations and compared with the theoretical predictions.

Chapter 2

Radiation Pattern For a Single Patch

2.0 Introduction

In this chapter the integral expressions for the radiation pattern of a single patch are developed and evaluated. Maxwell's equations are used to determine the electric field structure under the patch on the assumption of a magnetic wall surrounding the periphery of the patch (discussed in Chapter 1). The equivalence principle [6] is used to replace the field external to the patch region with magnetic currents on the periphery, which are then used to evaluate the electric vector potential from which the far fields may be calculated.

Figure 2.1 shows the geometry used in calculating the radiation pattern for a single patch. The short end is on the x axis.

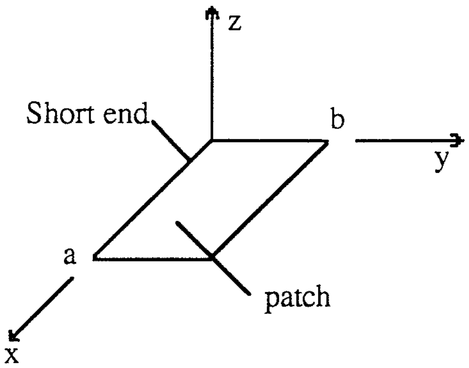

Figure 2.1 Geometry for determining the radiation pattern of a single patch.

2.1 Electric Field Structure Under the Patch

The vector differential equation for $\vec{E}$ is (assuming a time factor $e^{-j\omega t}$)

$$\nabla \times \nabla \times \vec{E} = \omega^2 \mu \varepsilon \vec{E} \tag{2.1}$$

Noting that there is only a z component of the electric field, and that all differentials with respect to the z direction are zero, (for a substrate thickness much smaller than the wavelength), the following differential equation for E_z results:

$$\frac{\partial^2 E_z}{\partial x^2} + \frac{\partial^2 E_z}{\partial y^2} + \omega^2 \mu\varepsilon E_z = 0 \qquad (2.2)$$

Using separation of variables,

$$E_z\,(x,y) = X(x)\,Y(y) \qquad (2.3)$$

and

$$k^2 = \omega^2\mu\varepsilon \qquad (2.4)$$

The resulting ordinary differential equations for X and Y are:

$$\frac{X''}{X} = -k_x^2\,,\ \frac{Y''}{Y} = -k_y^2 \qquad (2.5)$$

where

$$k_x^2 + k_y^2 = k^2 \qquad (2.6)$$

and the solutions are:

$$X = A\cos k_x x + B\sin k_x x \qquad (2.7a)$$

$$Y = C\cos k_y y + D\sin k_y y \qquad (2.7b)$$

To solve for the coefficients, the boundary conditions must be used. They are:

$E_z = 0$ at $y=0$ (electric short)

$H_x = 0$ at $y=b$ (magnetic short)

$H_y = 0$ at $x=0$ (magnetic short) and

$H_y = 0$ at $x=a$ (magnetic short)

The electric short is due to the metal conductor shorting the patch to the ground plane, while the magnetic shorts are due to the "magnetic conductors" . The magnetic conductors model the E-field as it reaches its maximum amplitude at the boundaries. A spatial maximum in the electric field corresponds to a minimum in the magnetic field since the two are related by spatial derivatives.

$$\nabla \times \vec{E} = -j\omega\mu\vec{H} \tag{2.8}$$

or

$$H_x = \frac{j}{\omega\mu}\frac{\partial E_z}{\partial y}, \quad H_y = -\frac{j}{\omega\mu}\frac{\partial E_z}{\partial x} \tag{2.9 a, b}$$

where $\partial/\partial t$ has been replaced by $-j\omega$.

At x=0, the boundary conditions yield

$$X'Y = 0 \tag{2.10}$$

and since $Y \neq 0$,

$$X'\,(x=0) = X'\,(x=a) = 0 \tag{2.11}$$

which results in

$$X(x) = A \cos \frac{n\pi}{a}x \quad , \text{for } n = 0,\ 1,\ 2,... \tag{2.12a}$$

Applying the boundary conditions to Y(y) yields

$$Y(y) = D \sin \frac{(2m-1)\pi}{2b}y \quad , \text{for } m = 1,\ 2,\ 3,\ ... \tag{2.12b}$$

Combining the two constants, and summing over all combinations of n and m gives

$$E_z(x,y) = \sum_{n=0}^{\infty} \sum_{m=1}^{\infty} A_{nm} \cos\left(\frac{n\pi}{a}x\right) \sin\left[\frac{(2m-1)\pi}{2b}y\right] \tag{2.13}$$

$$k_x = \frac{n\pi}{a} \text{ and } k_y = \frac{(2m-1)\pi}{2b} \tag{2.14a,b}$$

$$k^2 = k_x^2 + k_y^2 = \omega^2 \mu\varepsilon \tag{2.15}$$

and since $\omega = 2\pi f$, the expression for the resonant frequency of the structure is:

$$f_r = \frac{1}{2\sqrt{\mu\varepsilon}} \sqrt{\left(\frac{n}{a}\right)^2 + \left(\frac{2m-1}{2b}\right)^2} \tag{2.16}$$

2.1.1 Equivalent Magnetic Current at the Periphery of the Patch

In order to calculate the radiation pattern of the microstrip patch we may apply the equivalence principle, which states that we may replace the fields within some region with null fields provided equivalent electric and magnetic current densities are placed on the boundary separating the given region from the remainder of space. The current densities on the boundary must be such that they result in the discontinuities created by replacing the fields within the region by null fields. Given the electric and magnetic current densities on the boundary, the magnetic and electric vector potentials may be calculated and used to calculate the electric and magnetic fields.

In the present case, the tangential magnetic field at the open circuited boundaries is zero, and hence no discontinuity in the magnetic field results when setting the magnetic field within the boundary to zero. There is however a non-zero electric field resulting in a discontinuity when the internal electric field is set to zero. The result is an imaginary magnetic current density which gives rise to an electric vector potential. The expression for the current density is given by

$$\vec{M} = (\vec{E}^1 - \vec{E}^2) \times \hat{n}_{21} \tag{2.17}$$

where

$\vec{E}^1$ is the electric field outside the patch region

$\vec{E}^2$ is the electric field inside the patch region

$\hat{n}_{21}$ is a unit vector perpendicular to the boundary, and pointing from the inside region to the outside region.

If we define the three radiating apertures or walls as: *wall 1* x=a from y=0 to y=b, *wall 2* y=b from x=0 to x=a, and *wall 3* x=0 from y=0 to y=b, the resulting expressions for the magnetic current densities are:

Wall 1: $x=a,\ 0 \leq y \leq b$

$$\hat{n}_{21} = \hat{a}_x \tag{2.18a}$$

$$\vec{E}^1 = \cos n\pi \sin\left[\frac{(2m-1)\pi}{2b} y\right] \hat{a}_z \tag{2.18b}$$

$$\vec{M}_1 = (-1)^n \sin\left[\frac{(2m-1)\pi}{2b} y\right] \hat{a}_y \tag{2.18c}$$

Wall 2: $y=b,\ 0 \leq x \leq a$

$$\hat{n}_{21} = -\hat{a}_y \tag{2.19a}$$

$$\vec{E}^2 = \cos\left[\frac{n\pi}{a} x\right] \sin\left[\frac{(2m-1)\pi}{2}\right] \hat{a}_z$$

$$= (-1)^{m+1} \cos\left[\frac{n\pi}{a} x\right] \hat{a}_z \tag{2.19b}$$

$$\vec{M}_2 = (-1)^m \cos\left[\frac{n\pi}{a} x\right] \hat{a}_x \tag{2.19c}$$

Wall 3 *x=a, 0≤y≤b*

$$\hat{n}_{21} = -\hat{a}_x \tag{2.20a}$$

$$\vec{E}^3 = \sin\left[\frac{(2m-1)\pi}{2b} y\right] \hat{a}_z \tag{2.20b}$$

$$\vec{M}_3 = -\sin\left[\frac{(2m-1)\pi}{2b} y\right] \hat{a}_y \tag{2.20c}$$

The general expression for the electric vector potential is

$$\vec{F} = \frac{\varepsilon_0}{4\pi} \int_s \frac{\vec{M}\exp\left(-jk_0|\vec{r}-\vec{r}'|\right)}{|\vec{r}-\vec{r}'|} dS \tag{2.21}$$

as r approaches ∞, (far field), the expression for $\vec{F}$ is

$$\vec{F} \cong \frac{\varepsilon_0}{4\pi r} \exp\left(-jk_0 r\right) \int_s \vec{M}\exp(jk_0 r' \sin\theta \cos(\phi-\phi'))\, dS \tag{2.22}$$

where

$\vec{r}$,r are the vector and scalar distances to the observation point

r′ is the scalar distance to the source point in the integral

$\varepsilon_\circ$ is the permittivity of free space

$k_\circ$ is the wave number of free space

s is the surface over which the magnetic current densities exist

and θ,θ′,ϕ,ϕ′ are the usual coordinates in the spherical system.

2.2 Determining the Far Field Radiation Pattern

2.2.1 Evaluating the Integral for the Three Walls

Wall 1: For wall 1 the following simplifications are made

$$r' = \sqrt{a^2+y^2}$$

$dS = h\,dy$ where h is the distance from the ground plane to the patch, (i.e. the substrate thickness)

$\phi' = \tan^{-1}\frac{y}{a}$

$\cos(\phi - \phi') = \cos\phi\cos\phi' - \sin\phi\sin\phi'$

$\cos\phi' = \frac{a}{r'}\ ,\ \sin\phi' = \frac{y}{r'}$

thus $r'\cos(\phi - \phi') = a\cos\phi + y\sin\phi$

and

$$\vec{F}_1 = \frac{h\varepsilon_0\exp(-jk_0r)}{4\pi r}\int_{y=0}^{b}(-1)^n\sin\left[\frac{(2m-1)\pi}{2b}y\right]\exp\left[jk_0\sin\theta\left(a\cos\phi + y\sin\phi\right)\right]dy\,\hat{a}_y$$

$$= \frac{h\varepsilon_0\exp(-jk_0r)(-1)^n\exp(jk_0a\sin\theta\cos\phi)}{4\pi r}\ \bullet$$

$$\int_{y=0}^{b}\sin\left[\frac{(2m-1)\pi}{2b}y\right]\exp(jk_0\sin\theta\cos\phi y)dy\,\hat{a}_y \qquad (2.23)$$

Evaluating this integral yields:

$$\frac{1}{k_0}\frac{(-1)^{m+1}j\sin\theta\sin\phi\exp\left(jk_0b\sin\theta\sin\phi\right) + \frac{2m-1}{2k_0b}\pi}{-\sin^2\theta\sin^2\phi + \left(\frac{2m-1}{2k_0b}\pi\right)^2} \qquad (2.24)$$

Similarly the integral for wall 2 is:

$$\frac{1}{k_0}\frac{(-1)^n j\sin\theta\cos\phi\exp\left(jk_0\sin\theta\cos\phi b\right) - j\sin\theta\cos\phi}{-\sin^2\theta\cos^2\phi + \left(\frac{n\pi}{k_0a}\right)^2} \qquad (2.25)$$

The integral for wall 3 is the same as for wall 1.

Accounting for the vector nature of the integrals, and the constants in front of the integrals, as well as the distance between the walls and the origin, the resulting values for the electric vector potentials are,

due to *wall 2:*

$$F_x = \frac{(-1)^m h\varepsilon_0 \exp(-jk_0 r)}{4\pi r k_0} j\sin\theta\cos\phi\exp\left(jk_0 b\sin\theta\sin\phi\right) \bullet$$

$$\left\{\frac{(-1)^n \exp\left(jk_0 a\sin\theta\cos\phi\right) - 1}{\left(\frac{n\pi}{k_0 a}\right)^2 - \sin^2\theta\cos^2\phi}\right\} \qquad (2.26)$$

due to *walls 1* and *3:*

$$F_y = \frac{h\varepsilon_0 \exp(-jk_0 r)}{4\pi r k_0}\left\{(-1)^n \exp\left(jk_0 a\sin\theta\cos\phi\right) - 1\right\} \bullet$$

$$\left\{\frac{(-1)^{m+1} j\sin\theta\sin\phi\exp\left(jk_0 b\sin\theta\sin\phi\right) + \frac{2m-1}{2k_0 b}\pi}{\left(\frac{2m-1}{2k_0 b}\pi\right)^2 - \sin^2\theta\sin^2\phi}\right\} \qquad (2.27)$$

In the far zone the components of the electric vector are related to those of the vector potential as:

$$E_\theta = -j\omega\eta_0 F_\phi \qquad (2.28a)$$

$$E_\phi = -j\omega\eta_0 F_\theta \qquad (2.28b)$$

After converting the spherical components to Cartesian ones, the above relationships become:

$$E_\theta = j\omega\eta_0 \sin\phi F_x - j\omega\eta_0 \cos\phi F_y \qquad (2.29a)$$

$$E_\phi = j\omega\eta_0 \cos\theta\cos\phi F_x + j\omega\eta_0 \cos\theta\sin\phi F_y \qquad (2.29b)$$

Replacing for F_x and F_y, the far field components take the forms

$$E_\theta = j\omega\eta_0 \frac{h\varepsilon_0 \exp(-jk_0r)}{4\pi r k_0} \Bigg[(-1)^m j\sin\theta\sin\phi\cos\phi\exp\left(jk_0 b\sin\theta\sin\phi\right) \cdot$$

$$\left\{ \frac{(-1)^n\exp\left(jk_0 a\sin\theta\cos\phi\right)-1}{\left(\frac{n\pi}{k_0 a}\right)^2 - \sin^2\theta\cos^2\phi} \right\} +$$

$$\cos\phi\left\{1 - (-1)^n\exp\left(jk_0 a\sin\theta\cos\phi\right)\right\} \cdot$$

$$\left\{ \frac{(-1)^{m+1} j\sin\theta\sin\phi\exp\left(jk_0 b\sin\theta\sin\phi\right) + \frac{2m-1}{2k_0 b}\pi}{\left(\frac{2m-1}{2k_0 b}\pi\right)^2 - \sin^2\theta\sin^2\phi} \right\} \Bigg] \tag{2.30}$$

$$E_\phi = j\omega\eta_0 \frac{h\varepsilon_0 \exp(-jk_0r)}{4\pi r k_0} \Bigg[(-1)^m j\sin\theta\cos\theta\cos^2\phi\exp\left(jk_0 b\sin\theta\sin\phi\right) \cdot$$

$$\left\{ \frac{(-1)^n\exp\left(jk_0 a\sin\theta\cos\phi\right)-1}{\left(\frac{n\pi}{k_0 a}\right)^2 - \sin^2\theta\cos^2\phi} \right\} +$$

$$\cos\theta\sin\phi\left\{(-1)^n\exp\left(jk_0 a\sin\theta\cos\phi\right) - 1\right\} \cdot$$

$$\frac{(-1)^{m+1} j\sin\theta\sin\exp\left(jk_0 b\sin\theta\sin\phi\right) + \frac{2m-1}{2k_0 b}\pi}{\left(\frac{2m-1}{2k_0 b}\pi\right)^2 - \sin^2\theta\sin^2\phi} \Bigg] \tag{2.31}$$

Operating in the lowest order mode where $n = 0$ and $m = 1$, the resulting expressions become:

$$E_\theta = j\omega\eta_0 \frac{h\varepsilon_0 \exp(-jk_0r)}{4\pi r k_0} \Bigg[-j\sin\phi\exp\left(jk_0 b\sin\theta\sin\phi\right) \cdot$$

$$\left\{\frac{1-\exp\left(jk_0 a\sin\theta\cos\phi\right)}{\sin\theta\cos\phi}\right\}+$$

$$\cos\phi\left\{1-\exp\left(jk_0 a\sin\theta\cos\phi\right)\right\}\bullet$$

$$\left.\left\{\frac{+j\sin\theta\sin\phi\exp\left\{jk_0\sin\theta\sin\phi b\right\}+\frac{\pi}{2k_0b}}{\left(\frac{\pi}{2k_0b}\right)^2-\sin^2\theta\sin^2\phi}\right\}\right] \qquad (2.32a)$$

$$E_\phi = j\omega\eta_0\frac{h\varepsilon_0\exp(-jk_0r)}{4\pi rk_0}\left[-j\cos\theta\exp\left(jk_0 b\sin\theta\sin\phi\right)\right.$$

$$\left\{\frac{1-\exp\left(jk_0 a\sin\theta\cos\phi\right)}{\sin\theta}\right\}-$$

$$\cos\theta\sin\phi\left\{1-\exp\left(jk_0 a\sin\theta\cos\phi\right)\right\}\bullet$$

$$\left.\left\{\frac{j\sin\theta\sin\phi\exp\left(jk_0 b\sin\theta\sin\phi\right)+\frac{\pi}{2k_0b}}{\left(\frac{\pi}{2k_0b}\right)^2-\sin^2\theta\sin^2\phi}\right\}\right] \qquad (2.32b)$$

For angles where the denominators become zero, the expressions may be evaluated correctly by taking their limits (the result is the same as if the integrals were performed using the parameters which cause the denominators to go to zero).

If the patch centre is moved to the coordinate origin, the above equations modify to:

$$E_\theta = j\omega\eta_0\frac{h\varepsilon_0\exp(-jk_0r)}{4\pi k_0 r}\left[-j\exp\left(jk_0\left(\frac{b}{2}\sin\phi-\frac{a}{2}\cos\phi\right)\sin\theta\right)\sin\phi\right.\bullet$$

$$\left\{\frac{1-\exp\left(jk_0 a\sin\theta\cos\phi\right)}{\sin\theta\cos\phi}\right\}+$$

$$\cos\phi \exp\left(-jk_0\left(\frac{b}{2}\sin\phi + \frac{a}{2}\cos\phi\right)\sin\theta\right)\left\{1 - \exp\left(jk_0 a\sin\theta\cos\phi\right)\right\} \bullet$$

$$\left.\left\{\frac{j\sin\theta\sin\phi\exp\left(jk_0 b\sin\theta\sin\phi\right) + \frac{\pi}{2k_0 b}}{\left(\frac{\pi}{2k_0 b}\right)^2 - \sin^2\theta\sin^2\phi}\right\}\right] \qquad (2.33a)$$

$$E_\phi = j\omega\eta_0\frac{h\varepsilon_0\exp(-jk_0 r)}{4\pi k_0 r}\left[-j\exp\left(jk_0\left(\frac{b}{2}\sin\phi - \frac{a}{2}\cos\phi\right)\sin\theta\right)\cos\theta \bullet\right.$$

$$\left\{\frac{1 - \exp\left(jk_0 a\sin\theta\cos\phi\right)}{\sin\theta}\right\} -$$

$$\cos\theta\sin\phi\exp\left(-jk_0\left(\frac{b}{2}\sin\phi + \frac{a}{2}\cos\phi\right)\sin\theta\right)\left\{1 - \exp\left(jk_0 a\sin\theta\cos\phi\right)\right\} \bullet$$

$$\left.\left\{\frac{j\sin\theta\sin\phi\exp\left(jk_0 b\sin\theta\sin\phi\right) + \frac{\pi}{2k_0 b}}{\left(\frac{\pi}{2k_0 b}\right)^2 - \sin^2\theta\sin^2\phi}\right\}\right] \qquad (2.33b)$$

2.2.2 Determining the Gain of the Antenna

In general, the radiation pattern is defined to be independent of the power flowing through the feed into the antenna, and thus any calculation made in regard to the field patterns must be related to some predefined reference. In this thesis, all theoretical radiation patterns use the 'gain over isotropic' definition of radiation pattern, where the power density at a given set of coordinates is related to the average power radiated by the antenna, or the power density of the antenna at any given angle were it to radiate equally in all directions, i.e. isotropically. In order to make this relationship, the power density must be defined, and the total power radiated must be evaluated. The power density is defined as follows:

$$\vec{S} = \vec{E} \times \vec{H}^* \tag{2.34}$$

where

$\vec{S}$ is the complex poynting vector, representing the power flow density

$\times$ is the vector curl operation and

* denotes the complex conjugate

Only the radial component of $\vec{S}$ need be considered, since the other components which represent power flowing around the antenna, are due to fields which vary as $\frac{1}{r^2}$, while the fields resulting in the radial component $\vec{S}$ vary as $\frac{1}{r}$, and thus for large r, the ratio of the axial to radial components of of $\vec{S}$ approaches zero.

$$S_r = E_\phi H_\theta^* - E_\theta H_\phi^* \tag{2.35}$$

The electric and magnetic fields, which form a plane wave in the far field, are related by the free space wave impedance

$$H_\theta = \frac{E_\phi}{\eta_0}, \; H_\phi = -\frac{E_\theta}{\eta_0} \tag{2.36}$$

Thus

$$S_r = \frac{1}{\eta_0}\left\{|E_\phi|^2 + |E_\theta|^2\right\} \tag{2.37}$$

The average power over the entire 2π steradians of the hemisphere is given by

$$P_{avg} = \frac{1}{4\pi\eta_0}\int_{\theta=0}^{\frac{\pi}{2}}\int_{\phi=0}^{\phi=2\pi}\left\{|E_\phi|^2 + |E_\theta|^2\right\} r^2 \sin\theta \,\partial\phi\partial\theta \tag{2.38}$$

This integral was evaluated numerically using Simpson's rule. The integrals were divided into 21 segments each (i.e. the entire hemisphere was divided into 21 by 21 = 441 elements). The outer integral is evaluated between $\theta = 0$ and $\theta = \frac{\pi}{2}$, the upper hemisphere, since the patch is assumed to be over an infinite ground plane, radiating into only the half space above the plane.

Figures (2.2) and (2.3) show the radiation pattern (both theoretical and experimental) of a single patch in the two principal planes, as well as in the plane $\phi = 45°$. The peak gain figures in Fig. 2.3 give the level of the top of the graph in dB. The theoretically calculated patterns used the following parameters

$a = 3$ cm

$b = 1.5$ cm

$\varepsilon_r = 2.52$

As calculated using (2.16), the resonant frequency is found to be 3.14 GHz. This is the resonant frequency of the cavity only, and does not account for the current probe or the fringing effect at the open end of the cavity. Experimentally the resonant frequency was measured to be 2.75 GHz. As will be discussed in the next chapter, the fringing electric fields, which extend beyond the edge of the patch opposite to the short circuited end, will affect the resonant frequency. This effect can be modelled by modifying the parameters above to account for the deviations in the resonant frequency. The effective parameters will be such that the structure is a half wavelength by quarter wavelength in dimension.

Note that $\theta=0°$ describes a single point independent of ϕ, and thus the value of the electric field should be independent of ϕ. The direction of the unit vectors $\hat{a}_\theta$ and $\hat{a}_\phi$ are dependant upon the value of ϕ and thus the values of E_θ and E_ϕ will depend on ϕ. For example in Fig. (2.1a) where $\phi = 0$, the θ and ϕ directed unit vectors are in the x and y directions respectively, and thus $E_x = E_\theta \cong 4$dB and $E_y = E_\phi = 0$ (Shown as -10 dB at the bottom of the plot), both for $\theta = 0°$.

Single patch centered at the origin

$a = 3.00$ cm
$b = 1.50$ cm
$f = 3.15$ GHz
$h = 0.16$ cm
$\varepsilon_r = 2.52$

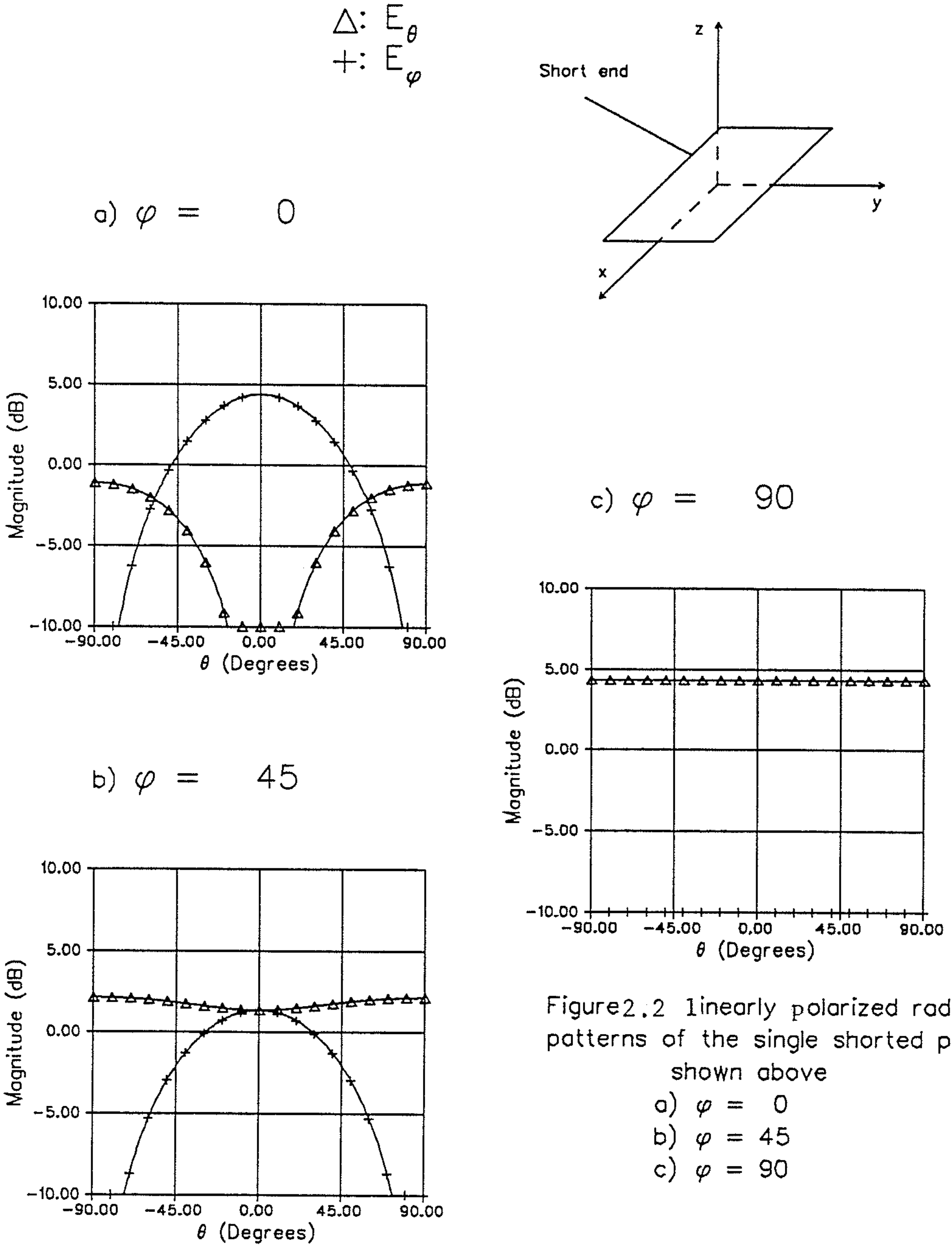

Figure2.2 linearly polarized radiation patterns of the single shorted patch shown above
a) φ = 0
b) φ = 45
c) φ = 90

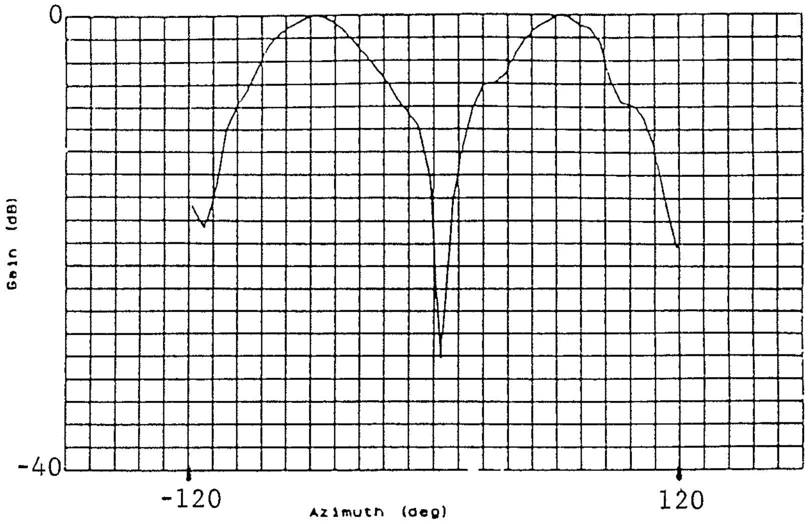

a) E_θ 12 degrees per division
Peak Gain = −0.28 dB, 2dB per division

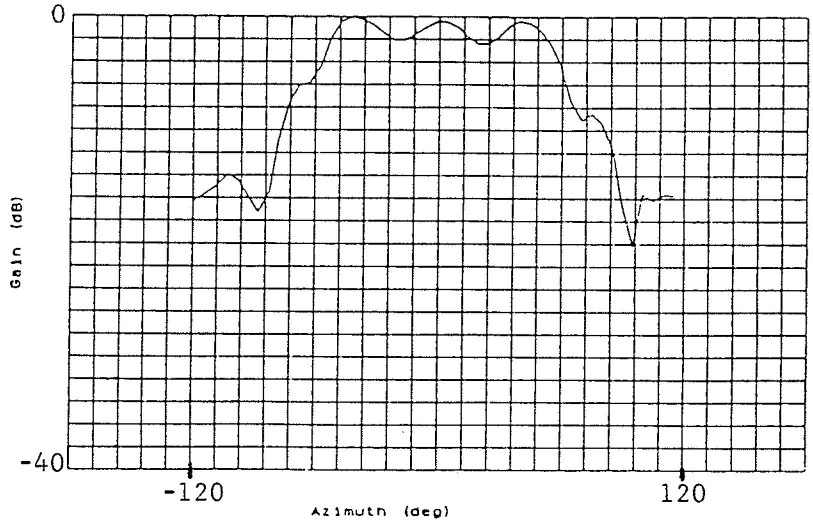

b) E_ϕ 12 degrees per division
Peak Gain = 1.44 dB, 2dB per division

Figure 2.3
Experimental linearly polarized radiation
patterns for the dimensions listed at φ = 0
a) E_θ
b) E_ϕ

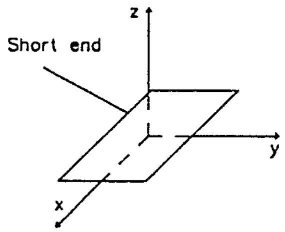

$a = 3.00$ cm
$b = 1.50$ cm
$h = .16$ cm
$f = 2.75$ GHz
$\varepsilon_r = 2.52$

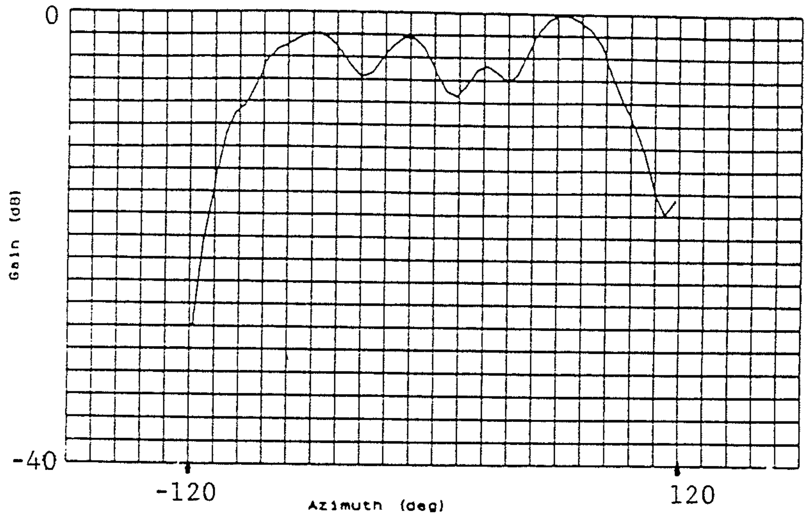

c) E_θ 12 degrees per division
Peak Gain = 4.49 dB, 2dB per division

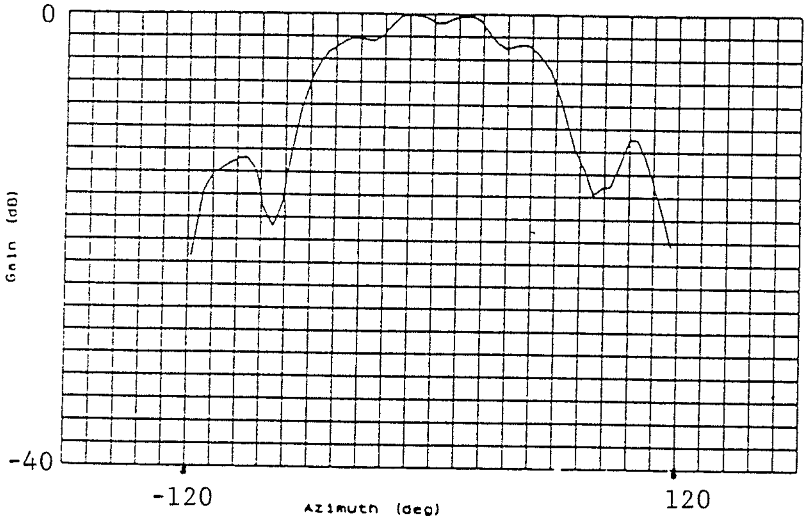

d) E_ϕ 12 degrees per division
Peak Gain = −1.80 dB, 2dB per division

Figure2.3 –
Experimental linearly polarized radiation
patterns for the dimensions listed at φ = 45
c) E_θ
d) E_ϕ

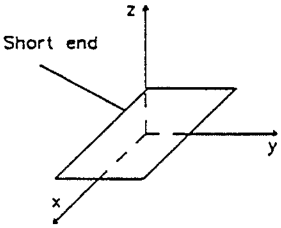

a = 3.00 cm
b = 1.50 cm
h = .16 cm
f = 2.75 GHz
ε_r = 2.52

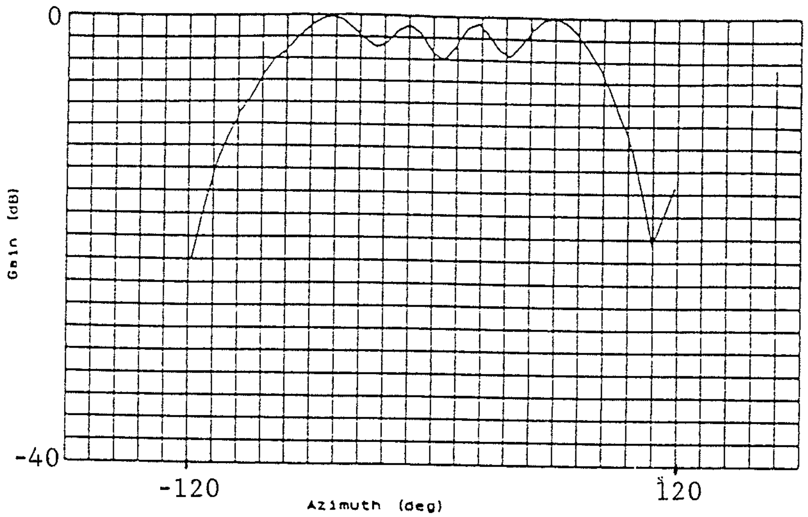

e) E_θ 12 degrees per division
Peak Gain = 5.03 dB, 2dB per division

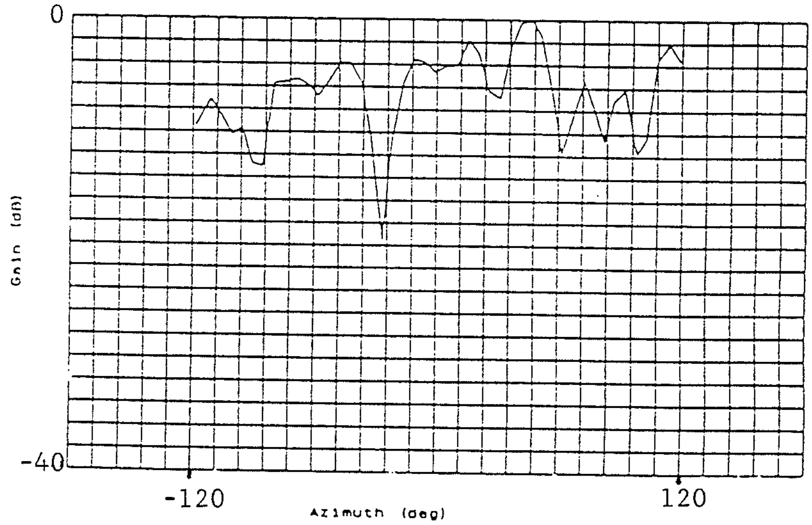

f) E_ϕ 12 degrees per division
Peak Gain =−16.64 dB, 2dB per division

Figure2.3
Experimental linearly polarized radiation
patterns for the dimensions listed at φ = 90

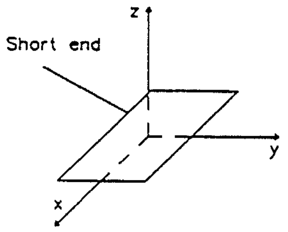

e) E_θ
f) E_ϕ

a = 3.00 cm
b = 1.50 cm
h = .16 cm
f = 2.75 GHz
ε_r = 2.52

Figures 2.3 a) and b), show the measured values of E_θ and E_ϕ in the $\phi = 0°$ plane. The theoretical value of E_ϕ in this plane at $\theta = 0°$ is approximately 4 dB, while the measured value is significantly lower. This discrepancy can be accounted for by noting that the measured pattern for E_θ in the $\phi = 90°$ plane (Figs. 2.3 e and f), although reaching values as high as 5.0 dB, has variations of as much as 4 dB. The measured value of E_θ in this plane at $\theta = 0°$ is much lower that the theoretical value of 4 dB. Since $\theta = 0°$ is a common point in all planes, the measured field components in all planes at $\theta = 0°$ will be lower than predicted. The variations in E_θ in the $\phi = 0°$ plane can be accounted for by asymmetries in the construction of the patch which produces asymmetries in the radiation pattern. As will be discussed in Chapter 4, the short was effected with the use of shorting pins, and was hence not a perfect short.

Evaluating E_θ and E_ϕ in the limit as θ approaches zero, yields

$$E_\theta = -j\omega\eta_0 \frac{h\varepsilon_0 \exp(-jk_0r)}{4\pi k_0 r} k_0 a \sin\phi \tag{2.39a}$$

$$E_\phi = -j\omega\eta_0 \frac{h\varepsilon_0 \exp(-jk_0r)}{4\pi k_0 r} k_0 a \cos\phi \tag{2.39b}$$

The x and y field components are related to the θ and ϕ components by

$$E_x = \{\cos\phi\, E_\theta - \sin\phi\, E_\phi\} \tag{2.40a}$$

$$E_y = \{\sin\phi\, E_\theta + \cos\phi\, E_\phi\} \tag{2.40b}$$

Thus E_x and E_y are given by

$$E_x = -j\omega\eta_0 \frac{h\varepsilon_0 \exp(-jk_0r)}{4\pi k_0 r} k_0 a \{\cos\phi \sin\phi - \sin\phi \cos\phi\} = 0 \tag{2.41a}$$

$$\begin{aligned} E_y &= -j\omega\eta_0 \frac{h\varepsilon_0 \exp(-jk_0r)}{4\pi k_0 r} k_0 a \{\sin^2\phi + \cos^2\phi\} \\ &= -j\omega\eta_0 \frac{h\varepsilon_0 \exp(-jk_0r)}{4\pi k_0 r} k_0 a \end{aligned} \tag{2.41b}$$

Figure 2.2 a) shows that at $\theta = 0°$, the electric field vector is in fact y directed. For $\phi = 0$, $E_\theta = 0$ and $E_\phi \neq 0$, thus $E_x = 0$ and $E_y \neq 0$. A similar analysis gives the same results for E_x and E_y for angles of ϕ other than zero.

By knowing the radiation patterns for a single patch in the hemisphere, it is possible to evaluate the radiation pattern of a circular array composed of several patches. In subsequent chapters variously configured circular arrays will be both theoretically and experimentally tested. The parameters which will be varied in the configurations will be the number of patches in the array, the physical size of the array (i.e. the distance of the elements to the origin), and the feeding arrangement of the array. The radiation patterns will show that very good circular polarization can be obtained by selecting proper configurations. Characteristics of the arrays will be shown to be easily varied by a simple change in the feeding arrangement, which may be performed electronically.

Chapter 3

Input Impedance of a Probe Fed Patch

3.0 Introduction

This chapter describes the mode method of evaluating the input impedance of a probe-fed patch when the probe is placed midway along the width, a, of the patch (see Fig. 3.1). Unlike Chapter 2, where the field structure under the patch was idealized to that of a cavity with magnetic walls, the field structure is determined using the various modifications to the cavity model discussed. The mode method requires the analytic solution of the electric field for all modes of wave propagation under the patch, as a function of the probe current, the probe location, the patch dimensions and the frequency. The simplifying assumptions used in Chapter 2 must be modified in order that the parameters of interest, i.e. the resonant frequency and the input impedance, may be calculated. It is inherent in the assumption of a magnetic field surrounding the periphery of the patch that the power flow away from the probe is zero (assuming a lossless dielectric, and lossless conductors for the patch and ground plane), resulting in an impedance whose real part is zero, and thus at least as far as the calculation of the real part of this impedance goes, the concept of aperture admittance must be invoked.

3.1 Calculating the Input Impedance of a Probe Fed Patch

To calculate the input impedance, one has to calculate the exact field structure under the patch, accounting for the current probe, and the non-zero admittance of the apertures or side walls. The electric field at the feed location is then evaluated in terms of the feed current, I_0, and the impedance may be determined. Yano and Ishimaru [7] use the following expression for determining the input impedance

$$Z_{in} = \frac{2}{I_0 I_0^*}\left\{-\frac{hI_0}{4\pi}\int_{\phi=0}^{2\pi} E_z\, d\phi\right\} \qquad (3.1)$$

where

I_0 is the input probe current

h is the thickness of the dielectric and

ϕ is the angular displacement along the periphery of the probe

It has been assumed that the current in the probe is approximately constant throughout the length of the probe. By setting I_0 to unity, the expression simplifies to

$$Z_{in} = -\frac{h}{2\pi}\int_{\phi=0}^{2\pi} E_z\, d\phi \qquad (3.2)$$

Because most of the power radiates through the aperture opposite to the short, it will be assumed that the aperture admittance of the two side walls is zero. In solving for the electric field, the patch is divided into two regions, $y \leq y'$, and $y \geq y'$, where y' is the location of the current probe in the y-direction, as shown in Fig. 3.1.

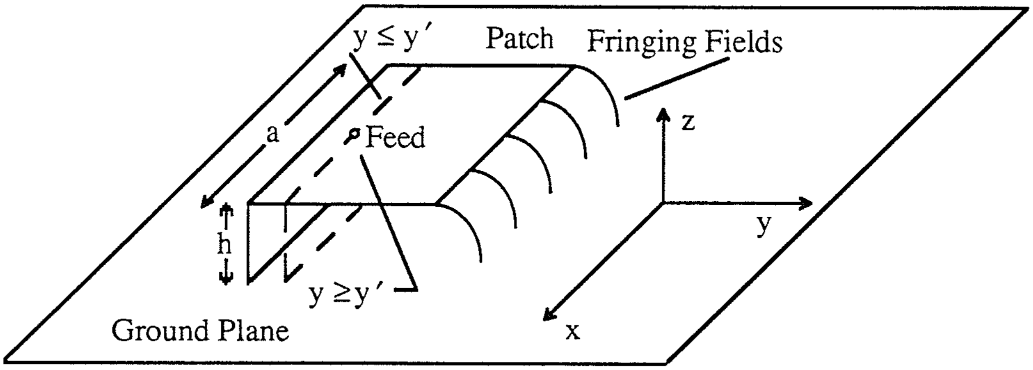

Figure 3.1 Patch divided into the two regions $y \leq y'$, and $y \geq y'$. The fringing fields are also shown.

The electric field, after solving Maxwell's Equations is defined for the two regions as

$$E_z^1 = \{A\ \cos k_{yn}y + B \sin k_{yn}y\}\ \{C \cos k_{xn}x + D \sin k_{xn}x\} \qquad (3.3a)$$

$$E_z^2 = \{A' \cos k_{yn}y + B' \sin k_{yn}y\}\ \{C' \cos k_{xn}x + D' \sin k_{xn}x\} \qquad (3.3b)$$

where k_{xn} and k_{yn} have been defined in Chapter 2. Region 1 is $y \leq y'$ and region 2 is $y \geq y'$.

Because it has been assumed that the side apertures have an admittance of zero, i.e., the cavity is finite, the values of k_{xn} are discreet, and hence the values of k_{yn} will also be discreet. If the admittance of the side walls were assumed to be non-zero, both k_{xn} and k_{yn} would assume a continuum of values, the only restriction being that $k_{xn}^2 + k_{yn}^2 = k^2$. Upon using the boundary conditions at x=0 and x=a, the expressions for the electric field in the two regions become:

$$E_z^1 = \sum_{n=0}^{\infty} \{A \cos k_{yn}y + B \sin k_{yn}y\} \cos \frac{n\pi}{a}x \qquad (3.4a)$$

$$E_z^2 = \sum_{n=0}^{\infty} \{A' \cos k_{yn}y + B' \sin k_{yn}y\} \cos \frac{n\pi}{a}x \qquad (3.4b)$$

where

$$k_{yn}^2 = k^2 - \left(\frac{n\pi}{a}\right)^2 \qquad (3.5)$$

and k is the wave number for the medium. The remaining boundary conditions used to solve for the four remaining constants are

$$1)\ \text{at } y = b \quad H_x^1 = y_n E_z^1 \qquad (3.6a)$$

$$2)\ \text{at } y = 0 \quad E_z^2=0 \tag{3.6b}$$

$$3)\ \text{at } y = y' \quad H_x^1-H_x^2 = -I_0\delta(x-x') \tag{3.6c}$$

$$4)\ \text{at } y = y' \quad E_z^1=E_z^2 \tag{3.6d}$$

where

y_n is the aperture admittance for the n^{th} mode

I_0 is the current on the probe

δ is the Dirac delta function

which yield

$$1)\ H_x = \frac{j}{\omega\mu_0}\frac{\partial E_z}{\partial y} = \frac{-jk_{yn}}{\omega\mu_0}\{A_n\sin k_{yn}b - B_n\cos k_{yn}b\}$$

$$= y_n\{A_n\cos k_{yn}b + B_n\sin k_{yn}b\} \tag{3.7a}$$

$$2)\ A_n' = 0 \tag{3.7b}$$

$$3)\ \sum_{n=0}^{\infty}\frac{-jk_{yn}}{\omega\mu_0}\{A_n\sin k_{yn}y' - B_n\cos k_{yn}y' + B_n'\cos k_{yn}y'\}\cos\frac{n\pi}{a}x$$

$$= -I_0\,\delta\,(x-x') \tag{3.7c}$$

$$4)\ A_n\cos k_{yn}y' + B_n\sin k_{yn}y'$$

$$= B_n'\sin k_{yn}y' \tag{3.7d}$$

where ω is the angular frequency, and μ_0 is the permeability of free space.

Since the thickness of the substrate is assumed to be much less than the wavelength λ, the current will be approximately constant throughout the length of the probe. By applying orthogonality of the cosine function, boundary condition (3.7c) becomes

$$A_n\sin k_{yn}y' - B_n\cos k_{yn}y' + B_n'\cos k_{yn}y' = \frac{-j\sigma_n I_0\omega\mu_0}{k_{yn}a}\cos\frac{n\pi}{a}x' \tag{3.7e}$$

where

$$\sigma_n = 1 \text{ for } n=0 \tag{3.8a}$$

$$\sigma_n = 2 \text{ for } n\geq 1 \tag{3.8b}$$

There are thus three equations, and three unknowns.

3.1.1 Evaluating the Aperture Admittance

The assumption that the electric field has only a z-component will in general not be true. At all points, including points along the aperture, the electric field will have some horizontal component which will extend to a small region beyond the patch. This horizontal component results in an energy storage in the region which must be accounted for by some reactive load. Similarly, the tangential portion of the magnetic field at the aperture will not be identically zero, and hence power will flow through the aperture away from the patch. This power is a real power and must be accounted for by a resistive load. The aperture may thus be represented by a complex impedance, whose value influences the input impedance and therefore the resonant frequency of the patch.

Defining the aperture admittance as $y_n = g_n + jb_n$, the conductive and susceptive parts are given in [7] as follows

$$g_n = \frac{P_r}{\frac{1}{2}\int_{\text{aperture}} |E_z|^2 dS}, \quad b_n = \frac{-P_i}{\frac{1}{2}\int_{\text{aperture}} |E_z|^2 dS} \tag{3.9a,b}$$

where P_r is the radiated power from the aperture, and P_i is the imaginary power in the region in all of the space outside of the patch region, but largely confined to a small region near the aperture. The denominator is integrated over the aperture.

3.1.1.1 Power Radiated for a Single Mode

The power that is radiated for a given mode may be calculated by integrating the power density pattern for that mode, over the half space above the patch (since an infinite ground plane is assumed). Thus

$$P_r = \frac{1}{2\eta_0} \int_{\phi=0}^{2\pi} \int_{\theta=0}^{\pi/2} \left\{ |E_\theta|^2 + |E_\phi|^2 \right\} r^2 \sin\theta \, d\theta \, d\phi \tag{3.10}$$

$$P_r = \frac{h^2}{32\pi^2\eta_0} \int_{\phi=0}^{2\pi} \int_{\theta=0}^{\pi/2} \frac{\sin^3\theta\cos^2\phi}{\left\{ \left(\frac{n\pi}{ka}\right)^2 - \sin^2\theta\cos^2\phi \right\}^2}$$

$$\left|(-1)^n \exp(jka\sin\theta\cos\phi) - 1\right|^2 \left\{ \sin^2\phi + \cos^2\theta\cos^2\phi \right\} d\theta \, d\phi \tag{3.11}$$

where

h is the dielectric thickness and

η_0 is the impedance of free space, 377 Ω.

3.1.1.2 Reactive Power for a Single Mode

The reactive power in any region is related to the rate of change of the electric and magnetic energies stored in that region as follows:

$$P_i = -2\omega \left\{ W_e - W_h \right\} \tag{3.12}$$

$$= -2\omega \left\{ \int_{\Delta v} \left\{ \frac{\varepsilon |E_z|^2}{4} - \frac{\mu_0 \left(|H_x|^2 + |H_y|^2 \right)}{4} \right\} dV \right\} \tag{3.13}$$

where

W_e is the electrical energy stored in the region

W_h is the magnetic energy stored in the region

ε is the permittivity of the dielectric and

Δv is the fringe region containing the circulating electric and magnetic energies

Δv is a volume and may be considered to be an annular cylinder, whose cross sectional area is determined by Δl below

$$\int_{\Delta v} \frac{\varepsilon}{4} |E_z|^2 dv = \frac{\varepsilon h \Delta l}{4} \int_{x=0}^{a} |E_z|^2 dx = \frac{\varepsilon h \Delta l}{4} \frac{a}{\sigma_n} \tag{3.14}$$

where

Δl is the extent to which the field extends laterally beyond the edge of the patch

a is the width of the patch

$$H_x = \frac{j}{\omega\mu} \frac{\partial E_z}{\partial y} = \frac{j}{\omega\mu} \cos \frac{n\pi}{a} x \, \frac{2m-1}{2b} \pi \cos \frac{(2m-1)\pi}{2b} y, \ = 0 \ \text{at } y=b \tag{3.15a}$$

$$H_y = \frac{-j}{\omega\mu} \frac{\partial E_z}{\partial x} = \frac{j}{\omega\mu} \frac{n\pi}{a} \sin \frac{n\pi}{a} x \sin \frac{(2m-1)\pi}{2b} y \tag{3.15b}$$

$$|H_y|^2 = \frac{(n\pi)^2}{(\omega\mu a)^2} \sin^2 \frac{n\pi}{a} x \ \text{ at } y=b \tag{3.15c}$$

$$\int_{\Delta v} \frac{\mu_0}{4} |H_y|^2 dv = \frac{h \Delta l (n\pi)^2}{8\omega^2 \mu_0 a} \tag{3.15d}$$

thus

$$P_i = -\frac{\omega h \Delta l}{2} \left\{ \frac{\varepsilon a}{\sigma_n} - \frac{(n\pi)^2}{2\omega^2 \mu_0 a} \right\} \tag{3.16}$$

and

$$b_n = \frac{\omega \Delta l \sigma_n}{a} \left\{ \frac{\varepsilon a}{\sigma_n} - \frac{(n\pi)^2}{2\omega^2 \mu_0 a} \right\} \tag{3.17}$$

In order to determine the reactive power, the fringe capacitance, or the extent to which the electric and magnetic field lines extend beyond the aperture, Δl, must be known. James, Hall and Wood [2] give an empirical expression for Δl as follows

$$\frac{\Delta l}{h} = 0.412\left(\frac{\varepsilon_e + .3)}{\varepsilon_e - .258)}\right)\left[\frac{\frac{a}{h} + .264}{\frac{a}{h} + .8}\right] \tag{3.18a}$$

where

h is the substrate thickness

a is the width of the patch, and

ε_e is the "effective" relative permittivity of the substrate as described below.

The equations that have been used to this point are based on the assumption that the dielectric which occupies the space below the microstrip patch, occupies all space. This has the effect of yielding values of resonant frequency and wavelength which are less than measured values, and as a result the concept of effective permittivity is generally used to account for the differences. Expressions which are used for calculating the effective relative permittivity are found in [2] and are shown below

$$\varepsilon_e = \frac{1}{2}\left\{\varepsilon_r + 1 + (\varepsilon_r - 1)\left(1 + \frac{10h}{w}\right)^{-\frac{1}{2}}\right\} \tag{3.18b}$$

$$\varepsilon_e\,(f) = \varepsilon_r - \frac{\varepsilon_r - \varepsilon_e}{1 + F_1\left\{\frac{f}{f_p}\right\}} \tag{3.18c}$$

$$f_p = \frac{0.4\ Z_m}{h\ (\mathrm{mm})}\ [\mathrm{GHz}]\ ,\quad F_1 \cong 0.6 + 0.009\ Z_m \tag{3.18d,e}$$

$$Z_m = \frac{\eta_0}{2\sqrt{\varepsilon_r}}\left\{\frac{a}{2h} + 0.441 + 0.082\left(\frac{\varepsilon_r - 1}{\varepsilon_r^2}\right) + \left(\frac{\varepsilon_r + 1}{2\pi\varepsilon_r}\right)\left(1.451 + \ln\left(\frac{a}{2h} + 0.94\right)\right)\right\}^{-1}$$

(3.18f)

Equation (3.18b), gives the effective permittivity at zero frequency, while (3.18c,d,e) give the permittivity as a function of frequency, in terms of the transmission line impedance, which is calculated using (3.18f).

Using the following parameters,

$a = 3$ cm

$b = 1.5$ cm

$h = .15875$ cm ($\frac{1}{16}$ inch)

$\varepsilon_r = 2.52$ and

f = (using 2.16 to estimate the resonant frequency) 3.14 GHz,

the effective patch parameters at 3.0 GHz may be calculated. Note that because of the insensitivity of (3.18c) to changes in f, it is reasonable to use a value of f which is close to the true value when calculating ε_e.

$\varepsilon_e = 2.29$ at $f = 0$ GHz (using (3.18b))

$Z_m = 20.14\ \Omega$ (using (3.18f))

$\varepsilon_e = 2.34$ at $f = 3.0$ GHz (using (3.18d,e and c)

Δl is .0786 cm (using (3.18a))

$b_e = 1.5$ cm + .0786 cm = 1.5786 cm

where b_e is the effective length of the patch which accounts for the fringing electric fields at the edge of the patch.

Figures 3.2 to 3.8 show the aperture admittance, both as a function of order (or mode), at three different frequencies, and as a function of frequency, at four different orders.

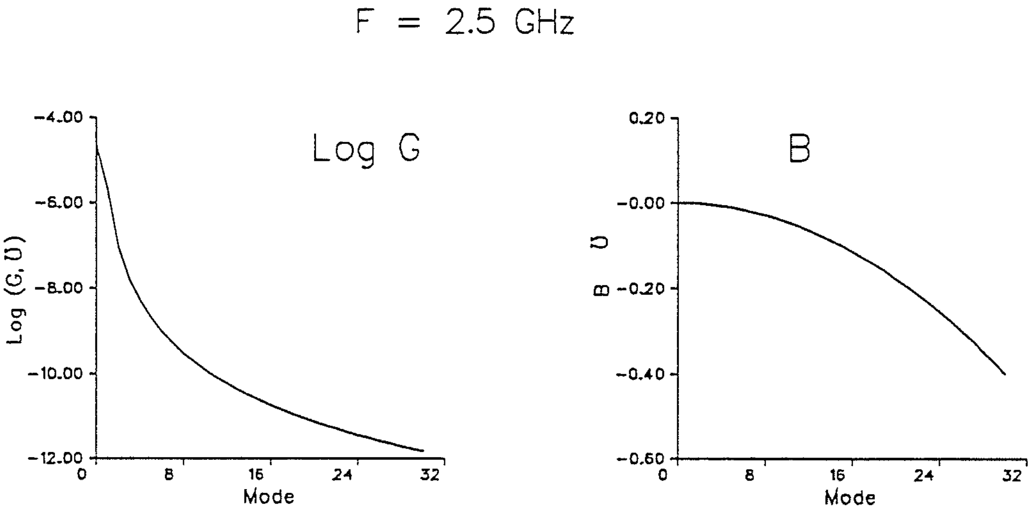

Figure 3.2
Aperture admittance as a function of mode for a patch of dimensions 3 cm by 1.5 cm, with one end shorted at 2.5 Ghz

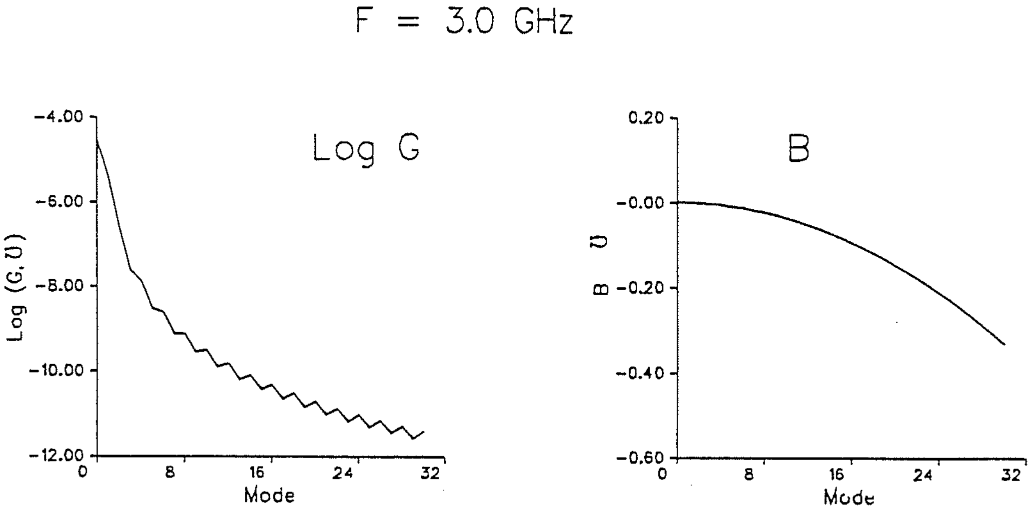

Figure 3.3
Aperture admittance as a function of mode for a patch of dimensions 3 cm by 1.5 cm, with one end shorted at 3.0 Ghz

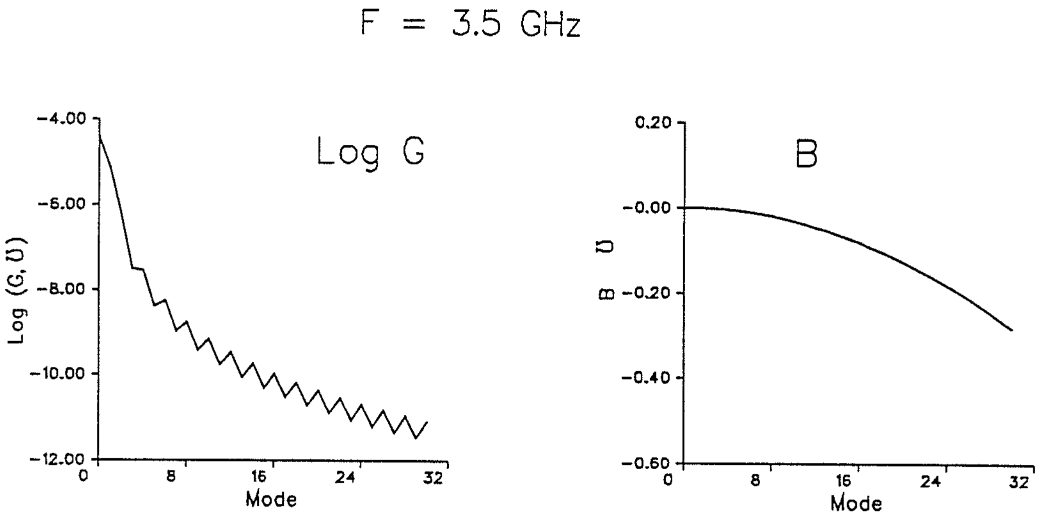

Figure 3.4
Aperture admittance as a function of mode for a patch of dimensions 3 cm by 1.5 cm, with one end shorted at 3.5 Ghz

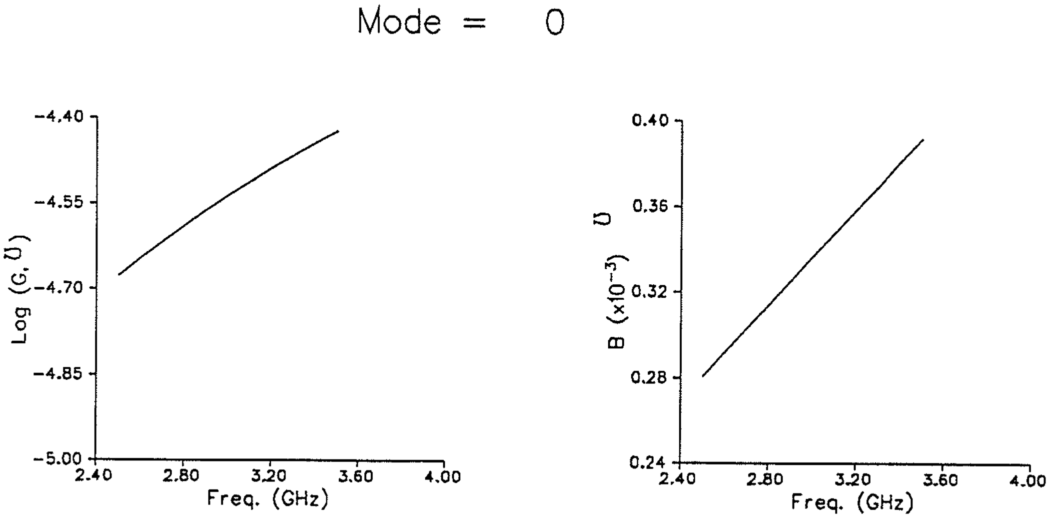

Figure 3.5
Aperture admittance of the 0th mode as a function of frequency for a patch of dimensions 3 cm by 1.5 cm, with one end shorted

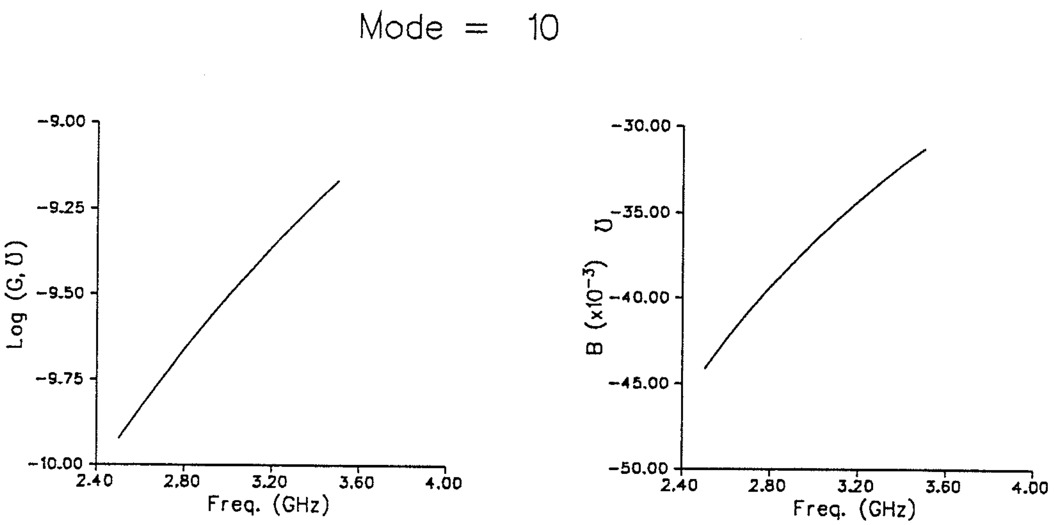

Figure 3.6
Aperture admittance of the 10th mode as a function of frequency for a patch of dimensions 3 cm by 1.5 cm, with one end shorted

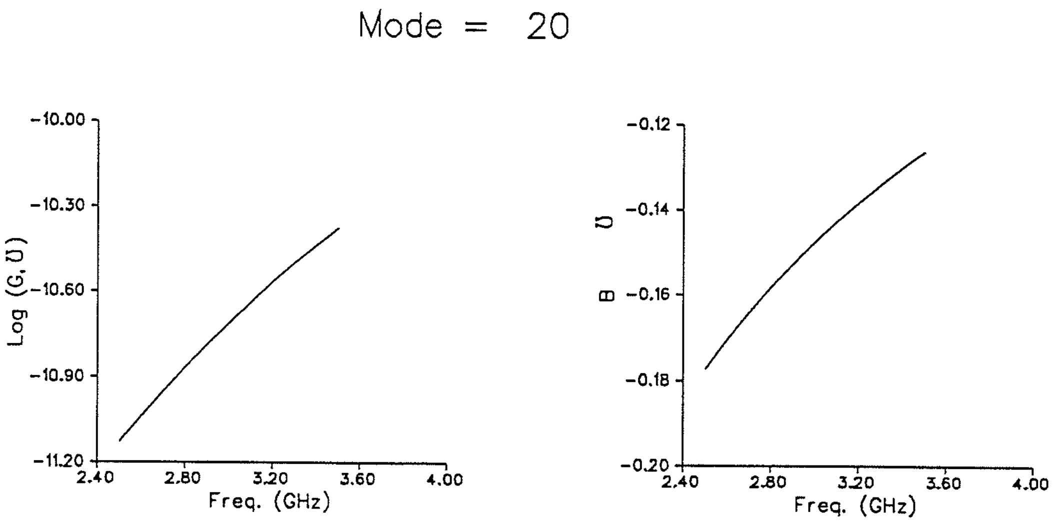

Figure 3.7
Aperture admittance of the 20th mode as a function of frequency for a patch of dimensions 3 cm by 1.5 cm, with one end shorted

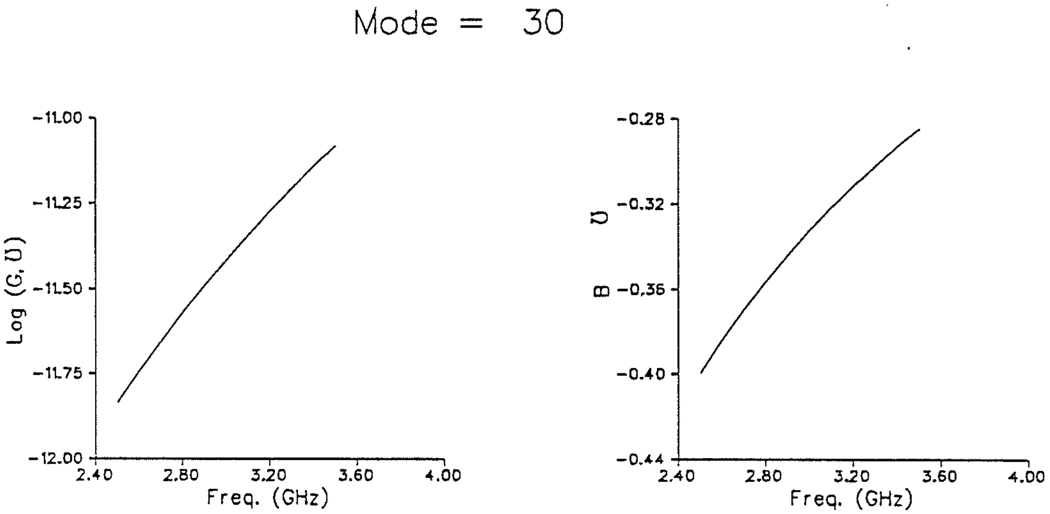

Figure 3.8

Aperture admittance of the 30th mode as a function of frequency for a patch of dimensions 3 cm by 1.5 cm, with one end shorted

The resulting matrix equation used to calculate the unknown coefficients is

$$\begin{bmatrix} \sin k_{yn}y' & -\cos k_{yn}y' & \cos k_{yn}y' \\ \dfrac{jk_y \sin k_{yn}b}{\omega\mu} - y_n \cos k_{yn}b & \dfrac{jk_y \cos k_{yn}b}{\omega\mu} - y_n \sin k_{yn}b & 0 \\ \cos k_{yn}y' & \sin k_{yn}y' & -\sin k_{yn}y' \end{bmatrix}$$

$$\begin{bmatrix} A_n \\ B_n \\ B'_n \end{bmatrix} = \begin{bmatrix} \dfrac{j\sigma_n \omega\mu \cos k_{xn}x'}{k_{yn}a} \\ 0 \\ 0 \end{bmatrix} \qquad (3.19)$$

Since the field required is the field at the boundary between the two regions, the resulting expression for the electric field in either of the regions may be used. Thus solving this matrix equation for B'_n, and substituting the values of x' and y' in the resulting expression for E_z is

$$E_z = \frac{\sigma_n \omega\mu \; k_{yn}\left[\sin k_{yn}b - \cos k_{yn}y' \sin k_{yn}(b-y')\right] - jy_n \omega\mu\left[\cos k_{yn}b - \cos k_{yn}y' \cos k_{yn}(b-y')\right] \cos^2 k_{xn}x}{ak_{yn}\{jk_{yn}\cos k_{yn}b - \omega\mu y_n \sin k_{yn}b\}} \qquad (3.20)$$

This expression must be summed from n = zero to infinity, with k_{xn} and k_{yn} defined previously. Noting that for large enough n, k_{yn} becomes imaginary, resulting in an expression with hyperbolic functions. For large enough values of n, the expression may be simplified by noting that for sufficiently large x,

$$\sinh x \cong \cosh x \cong .5 \exp x \qquad (3.21)$$

and for all x

$$\sinh jx = j \sin x, \text{ and } \cosh jx = \cos x \qquad (3.22)$$

Making this approximation the expression becomes $\frac{\sigma_n \omega \mu}{2ak_{yn}} \cos^2 k_{xn}x$ and since for large n, k_{yn} approaches $j\frac{n\pi}{a}$ the series for E_Z is divergent (because of the $\frac{1}{n}$ form of the terms). However it is only the imaginary part of the series which is of this form, the real part tending to a finite value.

Having calculated the electric field, the impedance of the patch may be evaluated. However, thus calculated, the impedance will not include the effects of the current probe which adds a reactive element to the input impedance of the patch, in accordance with its height (i.e. the thickness of the substrate), and its thickness. Dearnley, Russell, and Bard [8] give an approximate expression for the reactance due to the probe as

$$X_{Feed} = \frac{\eta_0 \omega h}{2\pi c} \ln \left\{ \frac{4c}{\zeta \omega d \sqrt{\varepsilon_r}} \right\} \qquad (3.23)$$

where

c is the velocity of light in a vacuum

d is the diameter of the feed and

$\zeta = 1.781072$, the natural log of Euler's number

This expression must be evaluated, and added to the impedance of the patch, as calculated using the mode method.

3.2 Construction of a Single Patch

Figure 3.9 shows the construction of the single patch. Note that instead of a shorting plane at one end, nine shorting pins were used. These pins were spaced 3 mm apart, and since the wavelength in the medium was approximately 6 cm, they closely approximated a perfect short. The deviation from a short can be quantified by noting that the posts will have some inductance when taken together. This inductance means that there is an "effective short" at a distance $\Delta l'$ from the location of the pins. James, Hall and Woods [2] calculate $\Delta l'$ as follows

$$\frac{\Delta l'}{a} = \frac{1}{2\pi}\left\{\ln\left(\frac{a}{2\pi r}\right) - \frac{4\pi^2 r^2}{a^2} + .601\,\frac{a^2}{\lambda'^2}\right\} \qquad (3.24)$$

where a and r are shown in Fig. 3.9, and λ' is the wavelength in the medium. Using a value of 3.0 GHz for the operating frequency and the dimensions given below, $\Delta l'$ is calculated to be on the order of 1 mm. It was found that a 1 mm change in the location of the feed probe has a significant effect on the measured impedance, and so this value of $\Delta l'$ could not be neglected. It is noted however that while the formula applies to posts of circular cross section, the shorting pins used were in fact of rectangular cross section. The value of r used was that of a circle with area equal to the area of the rectangular cross section of the pins.

In order to estimate the resonant frequency, the effect of an imperfect short, as quantified by (3.24), along with the effects of the fringing field as discussed in Section 3.1.1.2, and quantified in equations (3.18), must be taken into account. The shorting pins used in the experiment were of dimensions .66mm by .67mm, and had a centre to centre separation of a=.3cm. A circle of radius r=.38mm has an area equal to the area of the cross section of the pins. Using these values the new effective patch parameters may be calculated as follows (using a frequency of 3.0 GHz)

$\lambda' = 6.30$ cm

$\Delta l' = -.0193$ cm (using (3.24))

$b_e = 1.5 \text{ cm} + \Delta l\ (= .0786) + \Delta l'\ (= -.0193) = 1.5593$ cm where Δl as calculated in the previous section has been added to determine the 'overall' effective value for the patch length, b_e.

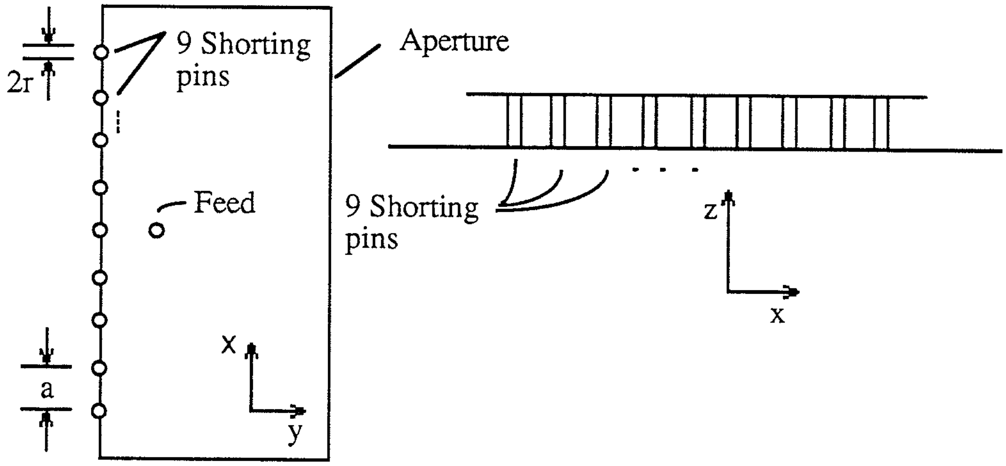

Figure 3.9 Construction of a single patch.

This negative value of $\Delta l'$ implies that the effective short due to the pins is closer to the open end than the pins themselves. Substituting this value for b in equation (2.16), along with the value calculated for the effective relative permittivity, the resonant frequency for the n=0, m=1 mode is approximately 3.14 GHz. (Note that this is the cavity frequency, accounting for the fringing effects of the field at the end of the patch, but for neither the probe impedance, nor the aperture admittance.)

Figure 3.10 a) to e) show the input impedance as a function of frequency and position of the feed from the short circuit, as calculated using the mode method. As discussed in Chapter 1, two types of feeds were used in the calculations of the input impedance. It was determined that the impedance did not vary significantly between the two types of feeds. The results shown were calculated using the infinitely thin feed, and truncating the imaginary part of the series after one term. The figure gives a table showing the symbols used to indicate the various frequencies, and the range over which those symbols are valid. In all cases the frequency increases in a clockwise direction. Figures 3.11 a) to c) show the input impedance of the patch as measured in the laboratory. The frequencies are shown on the plots. For both the theoretical and experimental results, the feed was placed midway between the two side walls (each of length b), at varying distances from the shorting pins.

The parameters used in evaluating the theoretical impedance are:

$a = 3$ cm

$b = 1.5$ cm

$\varepsilon_r = 2.52$

λ_m (the medium wavelength)= 6 cm (thus the patch is a quarter wave by half wave structure).

f = (using 2.16 to estimate the resonant frequency) 3.14 GHz.

Experimentally, the resonant frequency was found to be 2.79 GHz, thus λ_m was 6.87 cm.

The figures show a discrepancy between the measured and theoretical resonant frequency of less than one percent.

Using the results for the feed placed at .3 cm from the short, the impedance bandwidth, using a criterion of a VSWR ≤ 2, can be estimated. The criterion may be expressed in terms of the reflection coefficient, as $/\rho/ \leq 1/3$. For the theoretical results, this corresponds to a frequency range of 2.815 GHz to 2.83 GHz, or a bandwidth of 0.5%. For the experimental results, the frequency range is 2.77 GHz to 2.82 GHz, or a bandwidth of 1.8%.

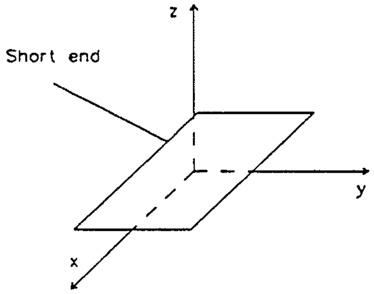

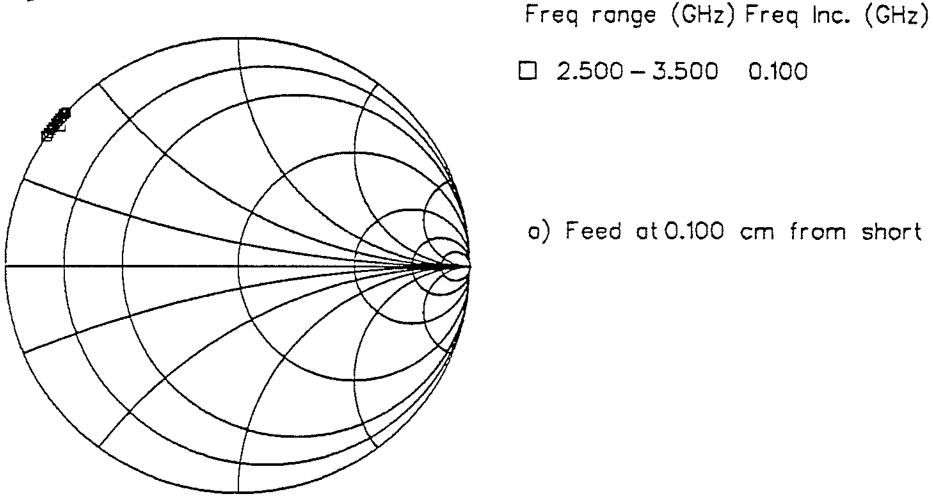

a) Feed at 0.100 cm from short

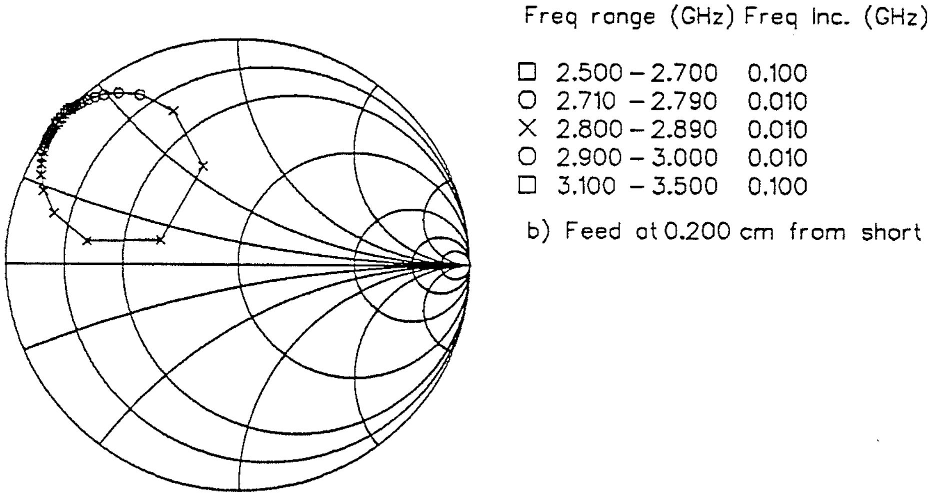

b) Feed at 0.200 cm from short

Figure 3.10 a,b) Input impedance for a patch of dimensions 3 cm by 1.5 cm, with a substrate thickness of .15875 cm and ε_r 2.52, (shown above) for various positions of the input feed, as calculated using the mode method.

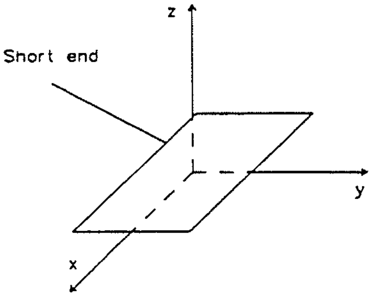

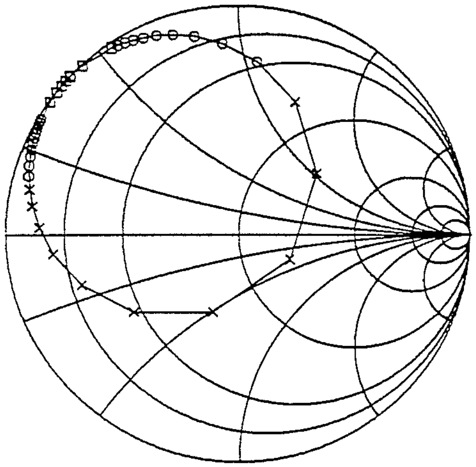

	Freq range (GHz)	Freq Inc. (GHz)
□	2.500 – 2.700	0.100
○	2.710 – 2.790	0.010
×	2.800 – 2.890	0.010
○	2.900 – 3.000	0.010
□	3.100 – 3.500	0.100

c) Feed at 0.300 cm from short

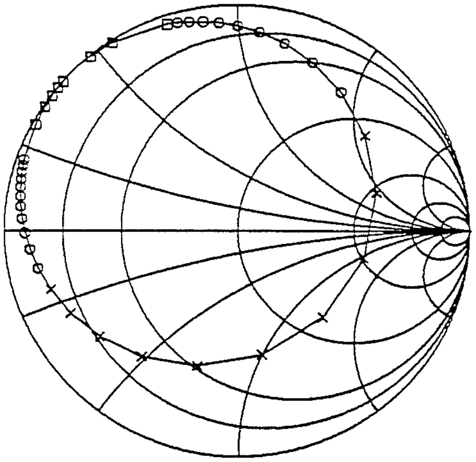

	Freq range (GHz)	Freq Inc. (GHz)
□	2.500 – 2.700	0.100
○	2.710 – 2.790	0.010
×	2.800 – 2.890	0.010
○	2.900 – 3.000	0.010
□	3.100 – 3.500	0.100

d) Feed at 0.400 cm from short

Figure 3.10 c,d) Input impedance for a patch of dimensions 3 cm by 1.5 cm, with a substrate thickness of .15875 cm and ε_r 2.52, (shown above) for various positions of the input feed, as calculated using the mode method.

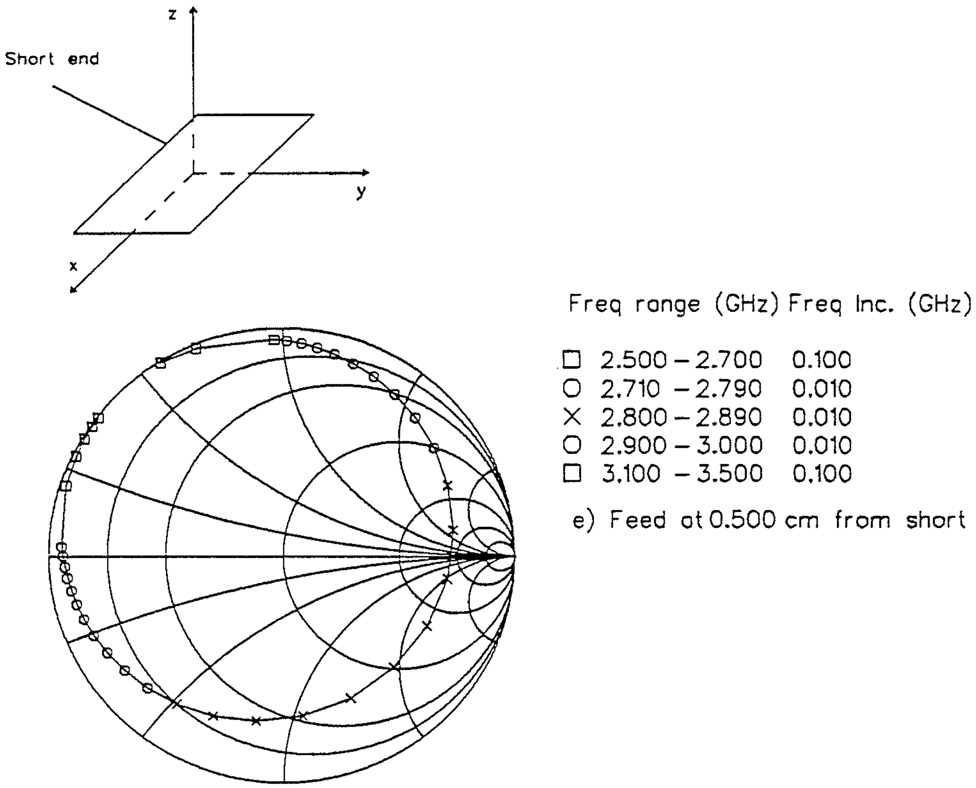

Figure 3.10 e) Input impedance for a patch of dimensions 3 cm by 1.5 cm, with a substrate thickness of .15875 cm and ε_r 2.52, (shown above) for various positions of the input feed, as calculated using the mode method.

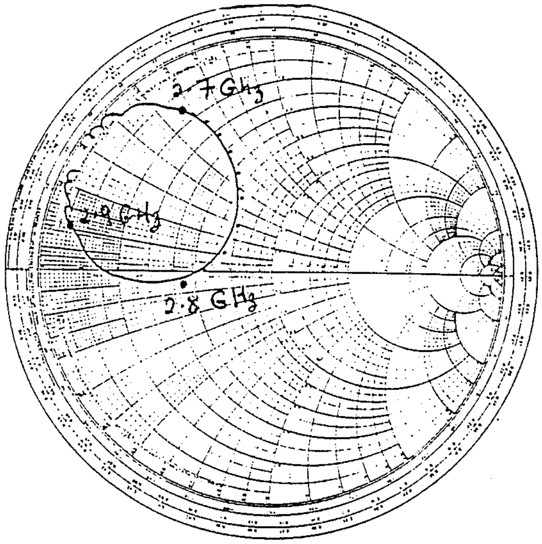

a) Feed at .2 cm from short

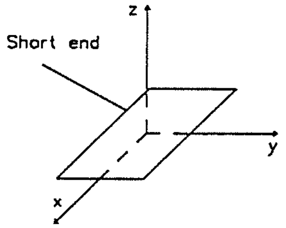

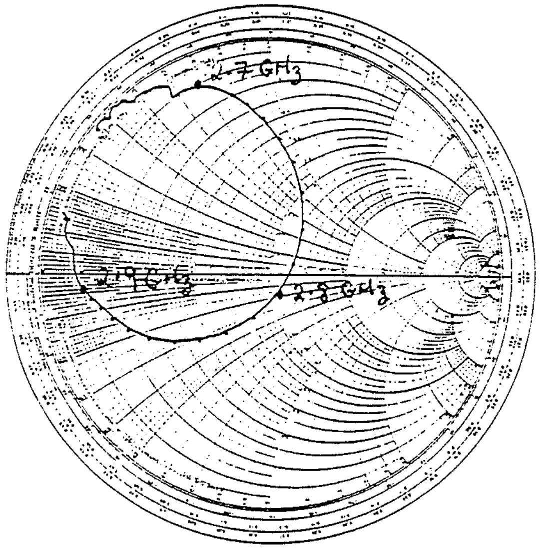

b) Feed at .3 cm from short

Figure3.11 a,b) Experimental input impedance for a patch of dimensions of 3 cm by 1.5 cm, with a substrate thickness of .15875 cm and ε_r 2.52, (shown above) for various postions of the input feed.

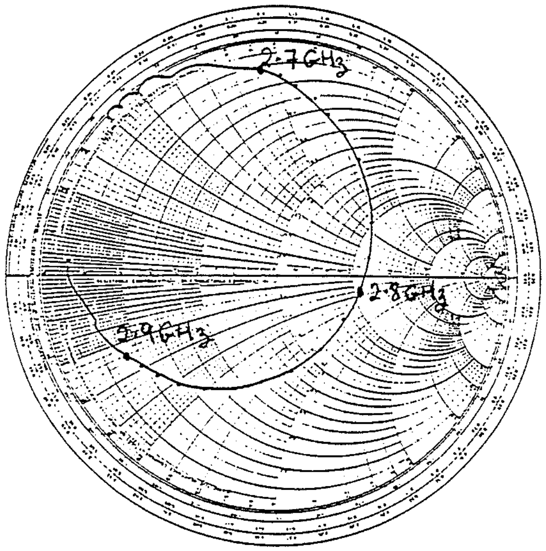

c) Feed at .4 cm from short

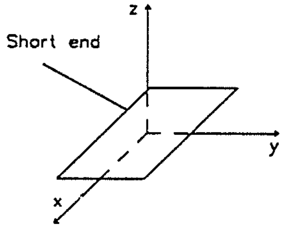

Figure 3.11c) Experimental input impedance for a patch of dimensions of 3 cm by 1.5 cm, with a substrate thickness of .15875 cm and ε_r 2.52, (shown above) for various postions of the input feed.

Chapter 4

Results

4.0 Introduction

This chapter of the thesis gives a description of a circularly polarized wave (or more generally an elliptically polarized wave), and various methods by which it may be generated, specifically, the method used in this thesis. Included are the results, experimental and theoretical, as well as a description of the experimental set up and methods, and the theoretical methods. The theoretical results include radiation patterns at the resonant frequency as calculated from (2.16), assuming a perfect short, and the dimensions of the individual patches given in the plots (Figs. 4.7, 4.9 and 4.11). The frequency was varied from 80% to 120% of the resonant frequency in 10% steps (with the patterns shown for 100%), and the pattern characteristics such as main beam and sidelobe power levels and beamwidths, as well as ranges of acceptable axial ratios are plotted.

4.1 Elliptically Polarized Waves

Electromagnetic waves may be classified according to their type of polarization. There are three classifications, elliptic, circular and linear, the latter two being special cases of the first. This classification describes the path traced by the electric field during a single cycle of oscillation. The vector representing the electric field of an elliptically polarized wave traces an ellipse during a single cycle of oscillation. The ellipse may be characterized according to the 'axial ratio' or the ratio of the major and minor axes. In the special case of a circularly polarized wave, the axial ratio is unity (or 0 dB), while in the case of a linearly polarized wave the axial ratio is infinite, and the electric field vector varies only in one direction. Figure 4.1 shows two of the polarization types.

Elliptically or circularly polarized waves may be further classified into two groups which designate the direction of rotation with respect to the direction of propagation, or the 'sense' of the rotation. In most instances it is desirable to generate a circularly polarized wave for a variety of reasons. It is possible for a linearly polarized antenna to receive power from circularly polarized wave independent of the attitude of the receiving antenna in the plane of circular polarization. Generally, when elliptical polarization is desired, it is the special case of circular polarization which is the optimum propagation type, and all elliptically polarized waves are quantified according to their approximation to a circularly polarized wave. The axial ratio is the measure by which the wave is compared to the ideal, a ratio of unity being perfect. If the ratio is taken to be that of the major to minor axes, (and hence by definition greater than or equal to unity), then a ratio of less than 1.414 or 3 dB, is generally deemed to be sufficiently circularly polarized.

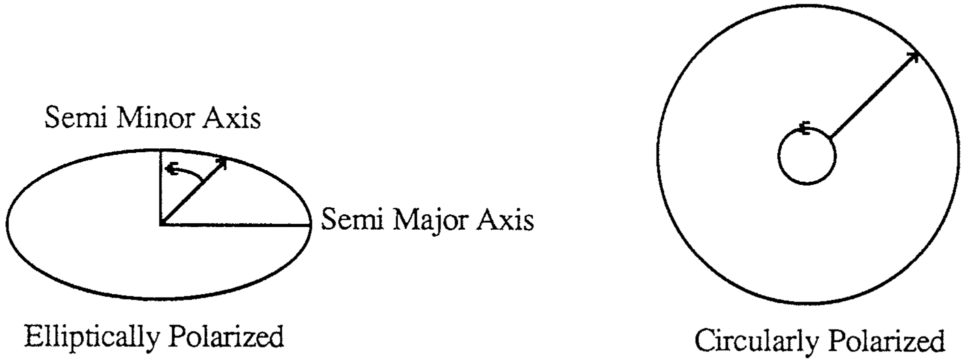

Figure 4.1 Elliptical and circular polarization.

4.2 Obtaining Circularly Polarized Waves

Many attempts have been made to produce circularly polarized from a single element, or an array of linearly polarized elements. Shen [9], has described an elliptically shaped antenna of low eccentricity (almost circular), which gives good circular polarization, and a bandwidth of 1 to 2 percent, for a feed located at 45°

with respect to the axes. The sense of the polarization depends whether the 45° angle is above or below the major axis. Huang [5] has shown that good circular polarization may be obtained in a four element circular array of linearly polarized elements, by feeding the elements with a phase pattern of 0°, 90°, 0°, 90°, or 0°, 90°, 180°, 270° for patterns measured in the ϕ=45° plane (i.e. the plane which bisects the 90° angle between any two adjacent elements). In the boresight direction, where the energy propagating away from the antenna is due to electric and magnetic fields in a plane parallel to the plane of the array (θ=0°) the quality of the circularly polarized wave is ideal (an axial ratio of unity). This can be demonstrated using an example of a two element array located on the xy-plane, and using simple slot antennas for the elements. The geometry of the array is shown in Fig. 4.2. The field expressions for a single element centered at the origin are given in [10] as follows

$$E_\phi = - A \sin\phi \cos\theta \frac{\cos\left(\frac{\pi}{2}\sin\phi \sin\theta\right)}{1 - \sin^2\phi \sin^2\theta} \tag{4.1a}$$

$$E_\theta = A \cos\phi \frac{\cos\left(\frac{\pi}{2}\sin\phi \sin\theta\right)}{1 - \sin^2\phi \sin^2\theta} \tag{4.1b}$$

where A is a complex constant.

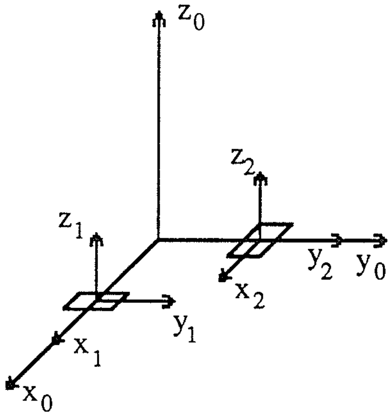

Figure 4.2 Geometry of a two element slot array.

Each of the elements is located on, and is parallel to, the xy-plane. With each element may be associated a local frame of reference and a local set of coordinate axes S_i consisting of the axes x_i, y_i and z_i and the three local, spherical coordinates r_i, ϕ_i, and θ_i. The main set of axes, x_0, y_0, z_0, may be labelled S_0. To determine the electric field due to the two elements, the electric field due to each element in the main coordinate system must be evaluated. Equations (4.1) give the electric field due to each slot in terms of the local set of spherical coordinates, thus these equations must be expressed in terms of the main coordinate system. In order to accomplish this the following observations are made regarding the transformation of S_0 to S_i.

1) The transformation consists of a rotation in the ϕ direction (i.e. the direction of the z-axis is unchanged), and a translation in the xy-plane

2) Because we are concerned with the far fields, (that is the distance from the antenna array to an observation point is much larger than the dimensions of the array) any observation point will have a θ_i component which is the same in any of the coordinate systems. (For example, if the observation point is on the z_0-axis, the value of θ_0 will be 0, i.e. the observation point is directly overhead. However, because the value of z for the observation point is large, the value of θ_i will also be approximately 0.) This is shown in Fig. (4.3), with $\theta=60°$.

3) If the x-axis of S_i is rotated an amount α_i with respect to the x-axis of S_0, the ϕ_i component of an observation point in the S_i system is given as $\phi_i = \phi - \alpha_i$.

4) With reference to the origin of S_0, the phase delay of any propagating waves introduced by the increased distance from the origin of S_i, (i.e. the center of slot i), to an observation point over the distance from the origin of S_0 to the same observation point is given as

$$- jk_0d' = -jk_0d \sin \theta \cos (\phi-\phi_i)$$

where d is the distance between the origin of S_0 and the center of the slot and d′ is the additional distance travelled by the wave when the patch is not centered at the origin. Figure 4.3 shows an example of this phase delay for values of $\phi_i = 0°$, $\alpha_i = 0°$, $\theta = 60°$ and $\phi = 45°$. The view is from the -y axis.

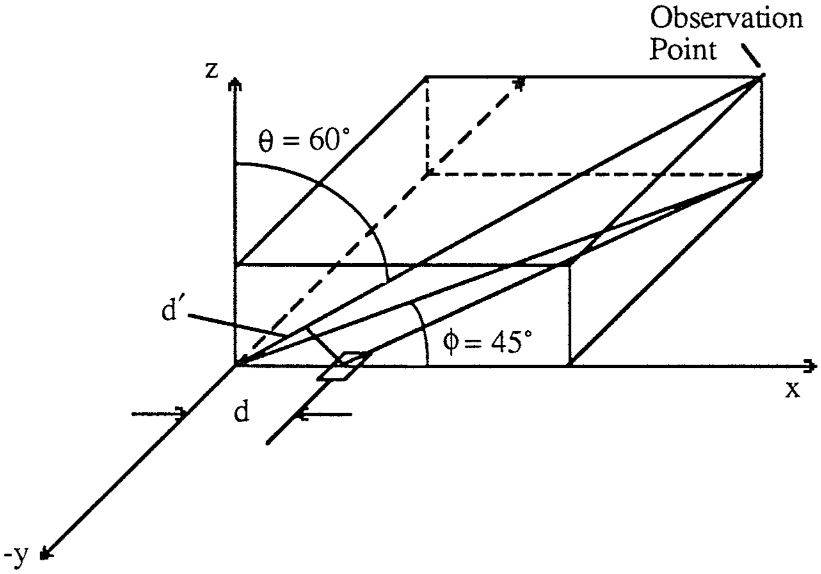

Figure 4.3 Phase delay for a patch not centered on the origin.

For $\theta = 0°$ equations (4.1 a and b) reduce to

$$E_\phi = - A \sin \phi \qquad (4.2a)$$

$$E_\theta = A \cos \phi \qquad (4.2b)$$

According to observation 2) above, for each element the value of ϕ in (4.2) must be $(\phi - \alpha_i)$. From Fig. (4.2) $\alpha_1 = 0°$ and $\alpha_2 = 90°$. Thus the components E_ϕ and E_θ are given by

$$E_\phi = -A \sin \phi - B\sin (\phi-90°) = -A\sin \phi + B\cos \phi \qquad (4.3a)$$

$$E_\theta = A\cos \phi + B\cos (\phi-90°) = A\cos \phi + B\sin \phi \qquad (4.3b)$$

where B is a complex constant, and the ratio of A to B depends on the ratio of the input feed currents of the two elements. Noting that at $\theta = 0°$, the Cartesian representation of the fields are given in terms of the spherical representations as

$$E_x = -\sin\phi\, E_\phi + \cos\phi\, E_\theta = A \tag{4.4a}$$

$$E_y = \sin\phi\, E_\theta + \cos\phi\, E_\phi = B \tag{4.4b}$$

If the elements are fed 90° out of phase, but with equal magnitudes (i.e. $B = jA$), then equations (4.4 a and b) become

$$E_x = A \tag{4.5a}$$

$$E_y = jA \tag{4.5b}$$

Reintroducing the suppressed $e^{j\omega t}$ factor and taking the real part of the result the expression for the electric field becomes

$$\vec{E} = A\,(\cos(\omega t)\ \hat{a}_x - \sin(\omega t)\,\hat{a}_y) \tag{4.6}$$

$$E_x = \cos(\omega t) \tag{4.7a}$$

$$E_y = -\sin(\omega t) \tag{4.7b}$$

$$E_x^2 + E_y^2 = 1 \tag{4.8}$$

and

$$\alpha = \tan^{-1}\left(\frac{-\sin\omega t}{\cos\omega t}\right) = -\omega t \tag{4.9}$$

thus the magnitude of the electric field is unity (or some constant), and the direction, α, of the field is linear with time. The electric vector traces a circle.

This analysis will yield the same result regardless of the form of equations (4.1 a and b) (The expressions for E_θ and E_ϕ in terms of θ and ϕ). Intuitively this is correct, since if an element is rotated by 90° in the xy-plane, (as is the case in Fig. 4.2), then the components of the field it produces parallel to the xy-plane will also be rotated by 90°. Two identical elements in both spatial and phase quadrature, will thus produce components of a field which are also in both spatial and phase quadrature.

At angles $\theta \neq 0°$, the following happens. The direction of energy propagation away from the array is no longer due to electric and magnetic fields which lie in a plane parallel to the plane of the array, and thus even though the distance to the observation point may be the same for both elements in a two element circular array, (as is the case for $\phi=45°$), the spatial relationship between the two fields will not be the required 90°. The result of this is a degradation in the axial ratio and a radiation pattern which is perfectly polarized in the boresight direction but becoming more and more elliptic as θ approaches 90°.

Huang [5] gives some reasoning behind using a feeding pattern of 0°, 90°, 180°, 270°, to achieve better circular polarization than that offered by 0°, 90°, 0°, 90°.

Schaubert et al [11] were able to generate a circularly polarized wave of satisfactory axial ratio for a beamwidth of 90°, using shorting pins in a rectangular patch. By strategically locating symmetrical pairs of posts, it is possible to select the resonant frequencies of X or Y-directed modes. If the frequencies are chosen to be approximately the same but not identical, by exciting the patch at an intermediate one, the wave impedances for the two modes will be such that one is inductive, and the other capacitive, and a circularly polarized wave may be generated. The following equations demonstrate this. Assuming that the wave impedances for the X-directed mode and the Y-directed mode are given as

$$z_x = r + jx \quad \text{and} \quad z_y = r - jx \tag{4.10a,b}$$

respectively, the voltage on the loads is given by

$$V_x = 1 + \Gamma_x \tag{4.11a}$$

$$V_y = 1 + \Gamma_y \tag{4.11b}$$

where Γ_x and Γ_y are the reflection coefficients for the loads z_x and z_y respectively, given by,

$$\Gamma_x = \frac{(r+jx) - 1}{(r+jx) + 1} \text{ and } \Gamma_y = \frac{(r-jx) - 1}{(r-jx) + 1} \qquad (4.12a,b)$$

and thus

$$V_x = \frac{2r^2 + 2r + 2x^2}{(r+1)^2+x^2} + j\frac{2x}{(r+1)^2+x^2}, \; V_y = \frac{2r^2 + 2r + 2x^2}{(r+1)^2+x^2} - j\frac{2x}{(r+1)^2+x^2} \qquad (4.13a,b)$$

The excitation current for the two modes is thus given by

$$I_x = \frac{V_x}{r+jx} = \frac{2r^3 + 2r^2 + 2rx^2 + 2x^2}{(r^2+x^2)((r+1)^2+x^2)} - j\frac{2xr^2 + 2x^3}{(r^2+x^2)((r+1)^2+x^2)} \qquad (4.14a)$$

$$I_y = \frac{V_y}{r-jx} = \frac{2r^3 + 2r^2 + 2rx^2 + 2x^2}{(r^2+x^2)((r+1)^2+x^2)} + j\frac{2xr^2 + 2x^3}{(r^2+x^2)((r+1)^2+x^2)} \qquad (4.14b)$$

The phase between these two currents is given by

$$\phi = 2 \tan^{-1}\left(\frac{xr^2 + x^3}{r^3 + r^2 + rx^2 + x^2}\right) \qquad (4.15)$$

Thus by selecting x, which is done by separating the resonant frequencies appropriately, ϕ may be set to 90°, thus generating two field vectors in spatial and phase quadrature.

4.3 Resolving an Elliptically Polarized Wave into Right and Left Hand Circularly Polarized Waves

The two components of an electric field perpendicular to the direction of propagation may be resolved into a right and left handed circularly polarized waves. The resulting electric field is identical whether expressed as the sum of the two linearly polarized components, or as the sum of the two circularly polarized components. To determine the relationship between the linear components of the fields and the circularly polarized components, the latter should be defined. These definitions are

$$\hat{a}_r = \frac{\hat{a}_\theta - j\hat{a}_\phi}{\sqrt{2}}, \qquad \hat{a}_l = \frac{\hat{a}_\theta + j\hat{a}_\phi}{\sqrt{2}} \tag{4.16a,b}$$

Each of these unit circularly polarized components is a vector which traces a circle as time progresses.

Thus if the electric field vector is given as

$$\vec{E} = E_\theta\, \hat{a}_\theta + E_\phi\, \hat{a}_\phi = E_r\, \hat{a}_r + E_l\, \hat{a}_l \tag{4.17}$$

the E_r and E_l components are calculated as

$$E_r = \frac{E_\theta + jE_\phi}{\sqrt{2}}, \quad E_l = \frac{E_\theta - jE_\phi}{\sqrt{2}} \tag{4.17a,b}$$

For example if $\vec{E}$ is given by $A\,\hat{a}_\theta + B\,\hat{a}_\phi$, where A and B are both complex numbers, it would be resolved into right and left hand circularly polarized components as

$$\begin{aligned} \vec{E} &= \frac{A + jB}{\sqrt{2}}\,(\hat{a}_\theta + j\hat{a}_\phi) + \frac{A - jB}{\sqrt{2}}\,(\hat{a}_\theta - j\hat{a}_\phi) \\ &= \quad E_r\,(\hat{a}_\theta + j\hat{a}_\phi) \quad + \quad E_l\,(\hat{a}_\theta - j\hat{a}_\phi) \end{aligned} \tag{4.18}$$

4.4 Theoretical and Experimental Procedures

This thesis is concerned with the application of Huang's method to generate circularly polarized waves. Two phasing arrangements for feeding the elements of the circular array are used, one where the phasing of the elements was identical to their spatial arrangement, the other where the elements were grouped into two pairs, each pair having the same phases. In a four element array the phasing required was thus 0°, 90°, 180°, 270° or 0°, 90°, 0°, 90°.

4.4.1 Theoretical Implementation of the Circular Array

Unlike a linear array of elements, there is no array factor which may be multiplied by the single element pattern to obtain the radiation pattern of the entire array. A sum must be evaluated, each term of which contains the phase delay factor due to the positioning of the individual elements, a phasing factor due to the differences in the phase of the power entering the individual elements, as well as a factor to account for the rotation of the individual elements.

If it is assumed that a reference element is located at the origin, in regards to the phase delay (i.e. the phase lead or lag due to the positioning of the individual elements is related to the reference element at the origin), then the expression for the field due to all elements is

$$\vec{E}_{\theta,\phi} = \sum_{i=1}^{n} e^{j\beta_i} \; e^{jk_0 d_i \sin\theta_i \cos(\phi-\phi'_i)} \, \vec{E}_{\theta,\phi,i} \, (\theta,\phi-\alpha_i) \tag{4.19}$$

where

θ and ϕ define the observation point

ϕ'_i and d_i define the location of the i^{th} element

α_i defines the orientation of the i^{th} element

β_i feed phasing of the i^{th} element

n is the number of elements and

$\vec{E}_{\theta,\phi,i}\,(\theta,\phi)$ is the radiation pattern (θ or ϕ component) of the i^{th} element

In evaluating the radiation pattern of both the linearly polarized and circularly polarized components of the wave, it was necessary to compute the power density due to each component separately, and relate it to the 'isotropic' power density as discussed in Chapter 2. The average power of a linearly polarized wave is given simply by $\frac{A^2}{2\eta_0}$, where A is the amplitude of the wave. For the circularly polarized wave the average power density is given as

$$P_{avg} = \frac{1}{2\pi\eta_0} \int_{\omega t=0}^{2\pi} \left| A \frac{1}{\sqrt{2}} (\sin\omega t \, \hat{a}_\theta + \cos\omega t \, \hat{a}_\phi) \right|^2 d(\omega t)$$

$$= \frac{A^2}{2\eta_0} \qquad (4.20)$$

Thus in evaluating the radiation patterns for each of the four components (E_θ, E_ϕ, E_r, and E_l) the above expressions relating power to the amplitude of the components are evaluated, and related to the isotropic power reference.

4.4.2 Experimental Implementation of the Circular Array

The circular array was implemented using three phase shifters, two hybrid (0°, 90°) and a rat race (0°, 0° or 0°, 180°). Figure 4.4 shows a block diagram detailing the arrangement. When the rf is fed into the difference or delta port of the rat race, the output ports are 180° apart and the resulting phasing arrangement for the four patches is 0°, 90°, 180°, 270°. When feeding rf to the summation port of the rat race, the output ports are in phase and the feeding arrangement is 0°, 90°, 0°, 90°.

In order to construct a four element circular array, four patches were constructed, and matched to each other with respect to resonant frequency and input impedance. There were three parameters which determined both the resonant frequency, and the input impedance as follows

1) The exact location of the shorting pins
2) The exact location of the current probe (feed) and
3) The exact dimensions of the patch

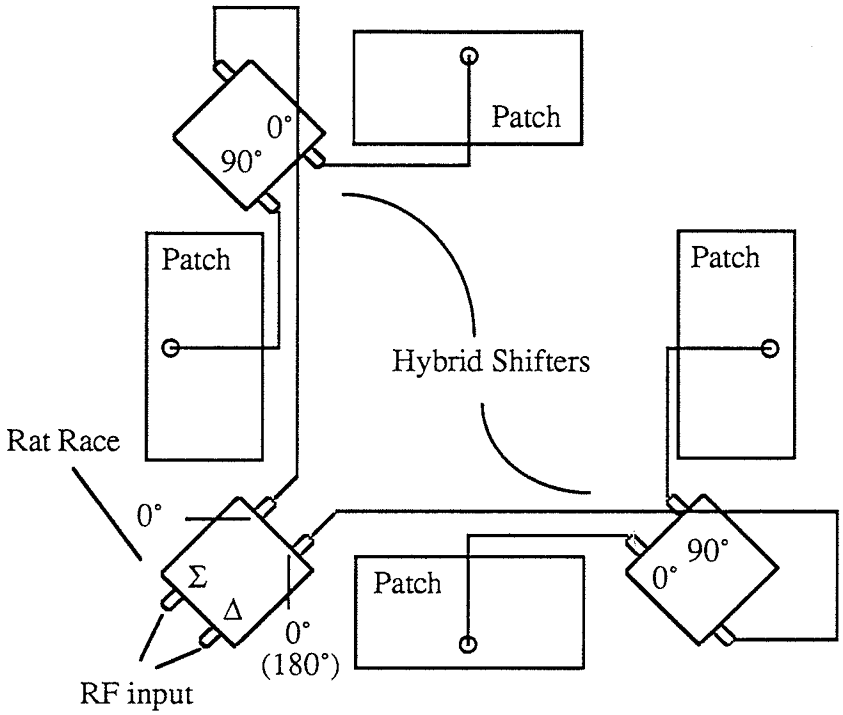

Figure 4.4 Block diagram of the feeding arrangement for four patches.

It was discovered experimentally that in order to achieve an input impedance of 50Ω, the location of the feed should be placed approximately 2.8 mm from the shorting pins and that this value of 2.8 mm was almost independent of the length of the patch. In order to match all of the patches for their resonant frequencies, and to have an impedance as close to 50 Ω as possible the following procedure was followed. First the probe was place in accordance with the location of shorting pins. Then the length of the patch was adjusted in order to match the resonant frequency with the other three patches, i.e. the distance from the open end of the patch to the location of the shorting pins (which possibly varied from patch to patch), had to be the same on all patches. This adjustment of the patch length was implemented using the copper tape available in the laboratory.

Once patches were matched, (the criterion used to determine matching was a reflection coefficient, Γ, less than .3 at one specified frequency, 2.75 GHz), they were placed on a 15 cm by 15 cm ground plane. Figure 4.5 shows the construction of the ground plane. The ground plane was made of aluminum, and had four slots cut out of it in the form of a cross, enabling the patches to be placed at different distances from the center of the plane. The coax feeds of the patches were placed through the slots, enabling the microwave circuits used for setting up the phasing arrangement to be placed on the side of the plane opposite the patches.

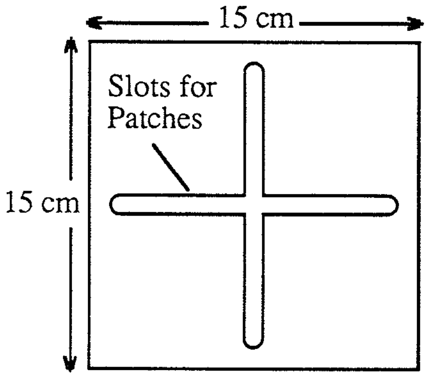

Figure 4.5 Construction of ground plane showing slots used to secure the patches.

4.5 Radiation Pattern

4.5.1 Radiation Pattern at Resonant Frequency

Figure 4.6 shows the schematic diagram of the circular array, with the geometry and symbols defined. Figures 4.7 to 4.12 show the theoretical and experimental results for six different configurations of the array (two phasing arrangements for each of the three values of d_i, the distance of the elements to the origin), in two different planes. Thus twelve sets of results are shown. The theoretical results, Figs. 4.7, 4.9 and 4.11, contain three plots for each of the eight configurations, one plot of the magnitude of both right and left hand circular polarization, one plot of the magnitude of the two components of the electric field,

E_θ and E_ϕ and one plot of the axial ratio. The third plot is on a separate page. Each page contains the plot or plots for each of the phasing arrangements. The corresponding experimental results, Figs. 4.8, 4.10 and 4.12 respectively, consist of the recorded radiation pattern obtained in a linear rotating measurement of the circular array. The frequency used for the measurements was 2.75 GHz. The theoretically calculated resonant frequency of the patches was, 2.81 GHz, based on a quarter wavelength by half wavelength patch. The distance d_i, in free space wavelengths, used in evaluating the theoretical results was based on the experimental value of d_i, and the experimental resonant frequency. (The program used in evaluating the theoretical results takes as input the value of d_i in free space wavelengths). Figure 4.13 shows the theoretical results for one configuration of the circular array, using eight elements, while Figs. 4.14 and 4.15 show the theoretical results for configurations of the array with 3 and 6 elements respectively.

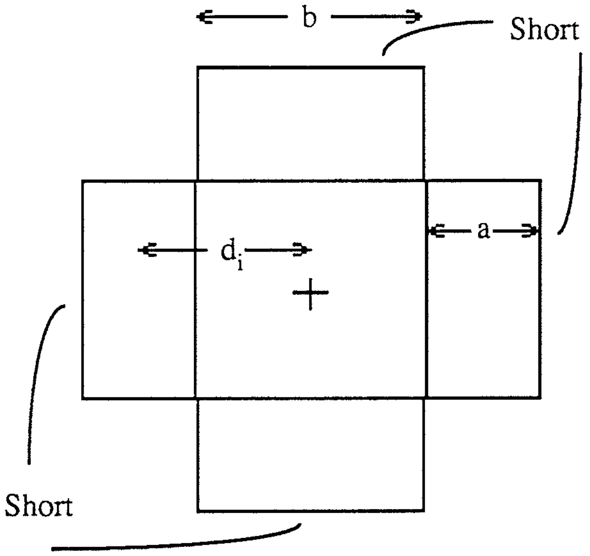

Figure 4.6 Four-element circular array set up.

a = 3.0 cm
b = 1.5 cm
h = 0.16 cm
f = 3.15 GHz
d_i = 2.7 cm = 0.28 λ_0
ε_r = 2.52

△: E_θ
+: E_φ
Ψ: E_r
$\Join$: E_l

φ = 0

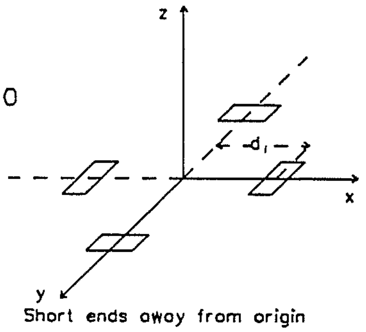

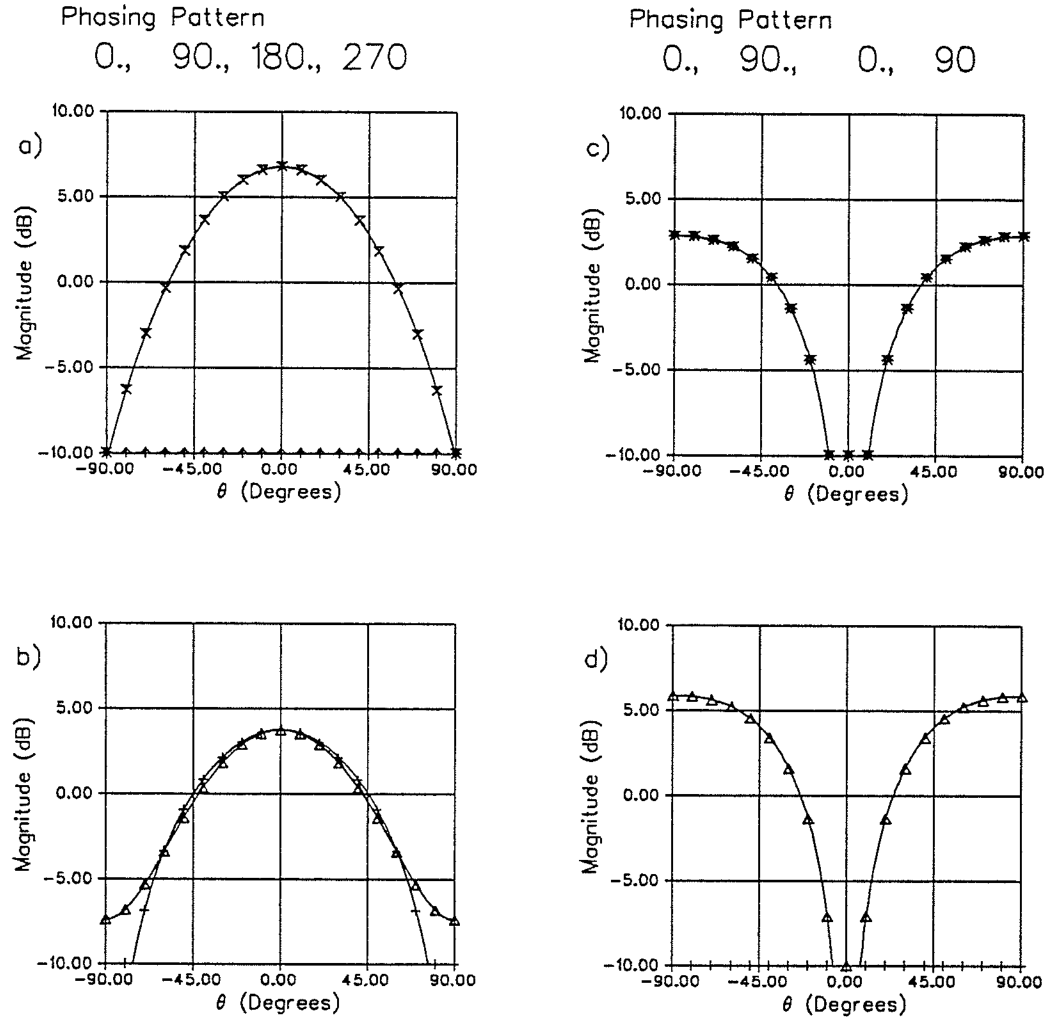
Phasing Pattern
0., 90., 180., 270

Phasing Pattern
0., 90., 0., 90

Figure 4.7 Theoretical radiation patterns for the dimensions listed above

a) φ = 0, circularly polarized pattern, 0, 90, 180, 270 feeding pattern
b) φ = 0, linearly polarized pattern, 0, 90, 180, 270 feeding pattern
c) φ = 0, circularly polarized pattern, 0, 90, 0, 90 feeding pattern
d) φ = 0, linearly polarized pattern, 0, 90, 0, 90 feeding pattern

$a = 3.0$ cm
$b = 1.5$ cm
$h = 0.16$ cm
$f = 3.15$ GHz
$d_i = 2.7$ cm $= 0.28\ \lambda_0$
$\varepsilon_r = 2.52$
◇axial ratio
$\varphi = 0$

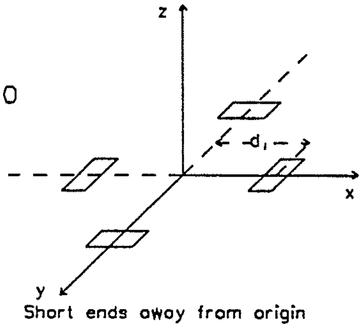

Phasing Pattern
0., 90., 180., 270

e)

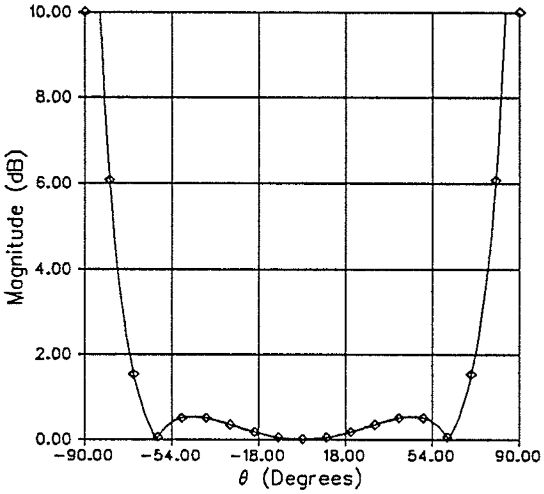

Phasing Pattern
0., 90., 0., 90

f)

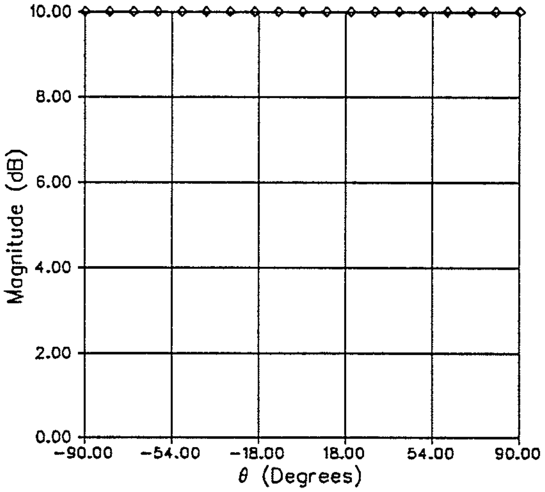

Figure 4.7 Theoretical radiation patterns for the dimensions listed above

e) $\varphi =$ 0, Axial ratios for 0, 90, 180, 270 feeding pattern
f) $\varphi =$ 0, Axial ratios for 0, 90, 0, 90 feeding pattern

$a = 3.0$ cm
$b = 1.5$ cm
$h = 0.16$ cm
$f = 3.15$ GHz
$d_i = 2.7$ cm $= 0.28\ \lambda_0$
$\varepsilon_r = 2.52$

△: E_θ
+: E_φ
✢: E_r
⧖: E_l

$\varphi = 45$

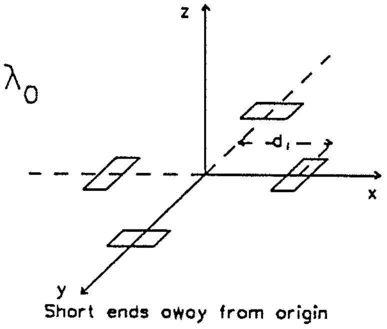

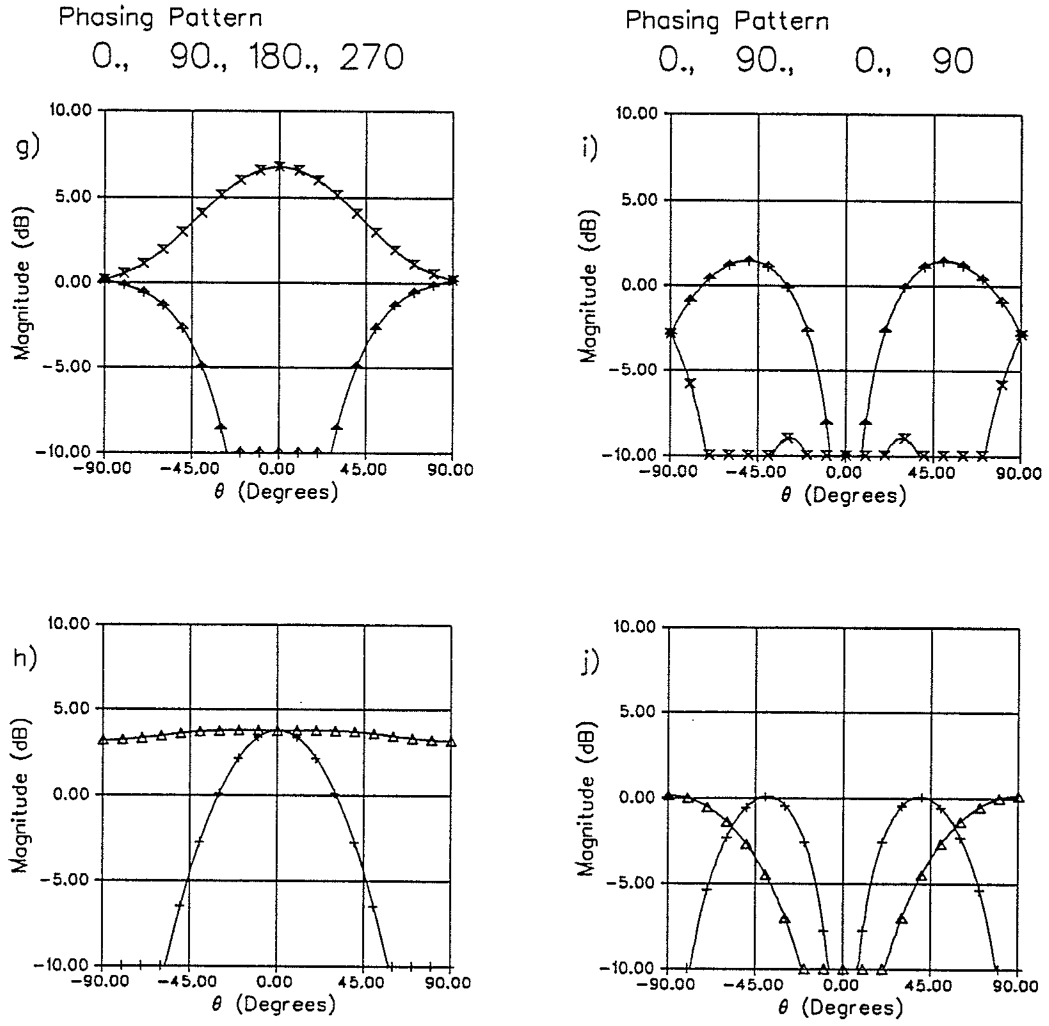
Phasing Pattern
0., 90., 180., 270

Phasing Pattern
0., 90., 0., 90

Figure 4.7 Theoretical radiation patterns for the dimensions listed above
g) φ = 45, circularly polarized pattern, 0, 90, 180, 270 feeding pattern
h) φ = 45, linearly polarized pattern, 0, 90, 180, 270 feeding pattern
i) φ = 45, circularly polarized pattern, 0, 90, 0, 90 feeding pattern
j) φ = 45, linearly polarized pattern, 0, 90, 0, 90 feeding pattern

$a = 3.0$ cm
$b = 1.5$ cm
$h = 0.16$ cm
$f = 3.15$ GHz
$d_i = 2.7$ cm $= 0.28\ \lambda_0$
$\varepsilon_r = 2.52$
◇axial ratio
$\varphi = 45$

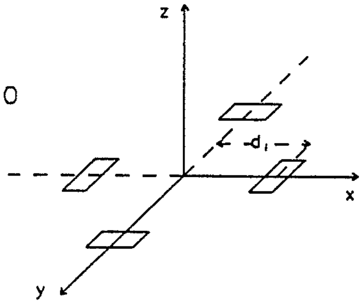

Short ends away from origin

Phasing Pattern
0., 90., 180., 270

k)

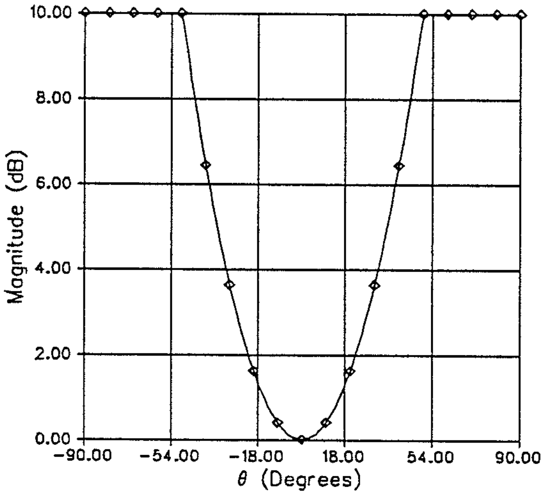

Phasing Pattern
0., 90., 0., 90

l)

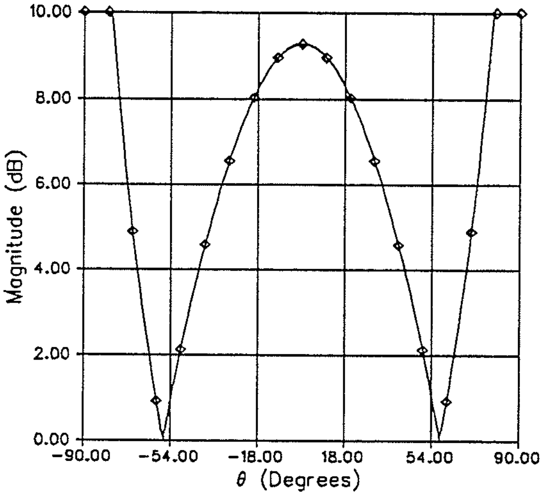

Figure 4.7 Theoretical radiation patterns for the dimensions listed above
k) $\varphi = 45$, Axial ratios for 0, 90, 180, 270 feeding pattern
l) $\varphi = 45$, Axial ratios for 0, 90, 0, 90 feeding pattern

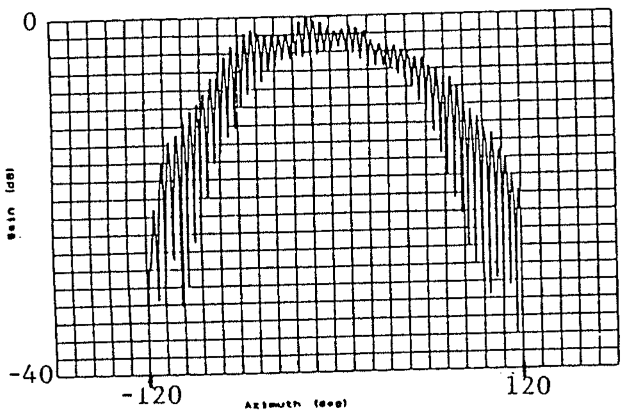

a) φ = 0, 12 degrees per division
Peak Gain = 1.84 dB, 2dB per division

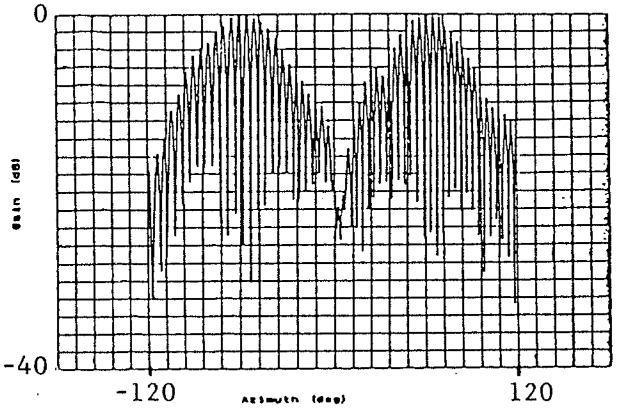

b) φ = 0, 12 degrees per division
Peak Gain = 0.61 dB, 2dB per division

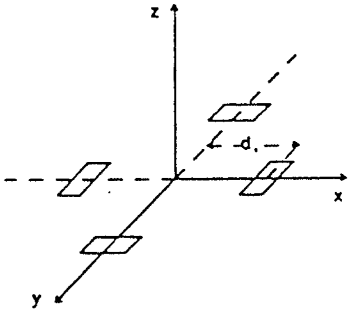

Short ends away from origin

$a = 3.00$ cm
$b = 1.50$ cm
$h = .16$ cm
$f = 2.75$ GHz
$d_i = 2.7$ cm
$= .28\ \lambda_0$
$\varepsilon_r = 2.52$

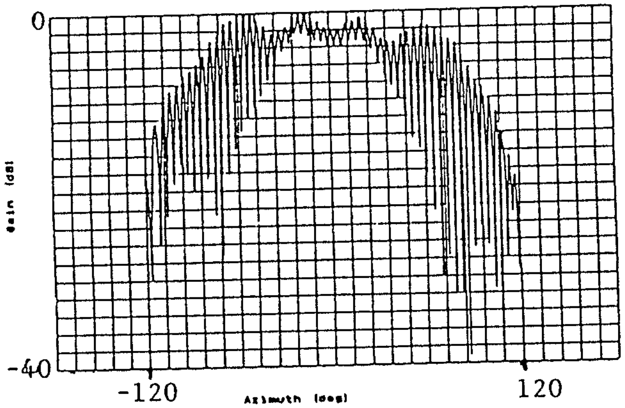

c) φ = 45, 12 degrees per division
Peak Gain = 2.13 dB, 2dB per division

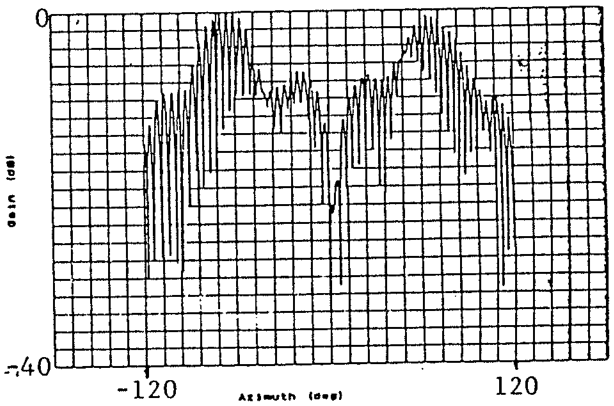

d) φ = 45, 12 degrees per division
Peak Gain = −2.19 dB, 2dB per division

Figure4.8 – Experimental rotating linear radiation patterns for the dimensions listed
a) φ = 0: 0, 90, 180, 270 feed pattern b) φ = 0: 0, 90, 0, 90 feed pattern
c) φ = 45: 0, 90, 180, 270 feed pattern d) φ = 45: 0, 90, 0, 90 feed pattern

$a = 3.0$ cm
$b = 1.5$ cm
$h = 0.16$ cm
$f = 3.15$ GHz
$d_i = 5.1$ cm $= 0.53\ \lambda_0$
$\varepsilon_r = 2.52$

△: E_θ
+: E_φ
⊕: E_r
⊠: E_l

$\varphi = 0$

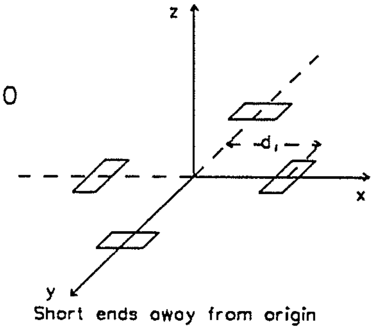

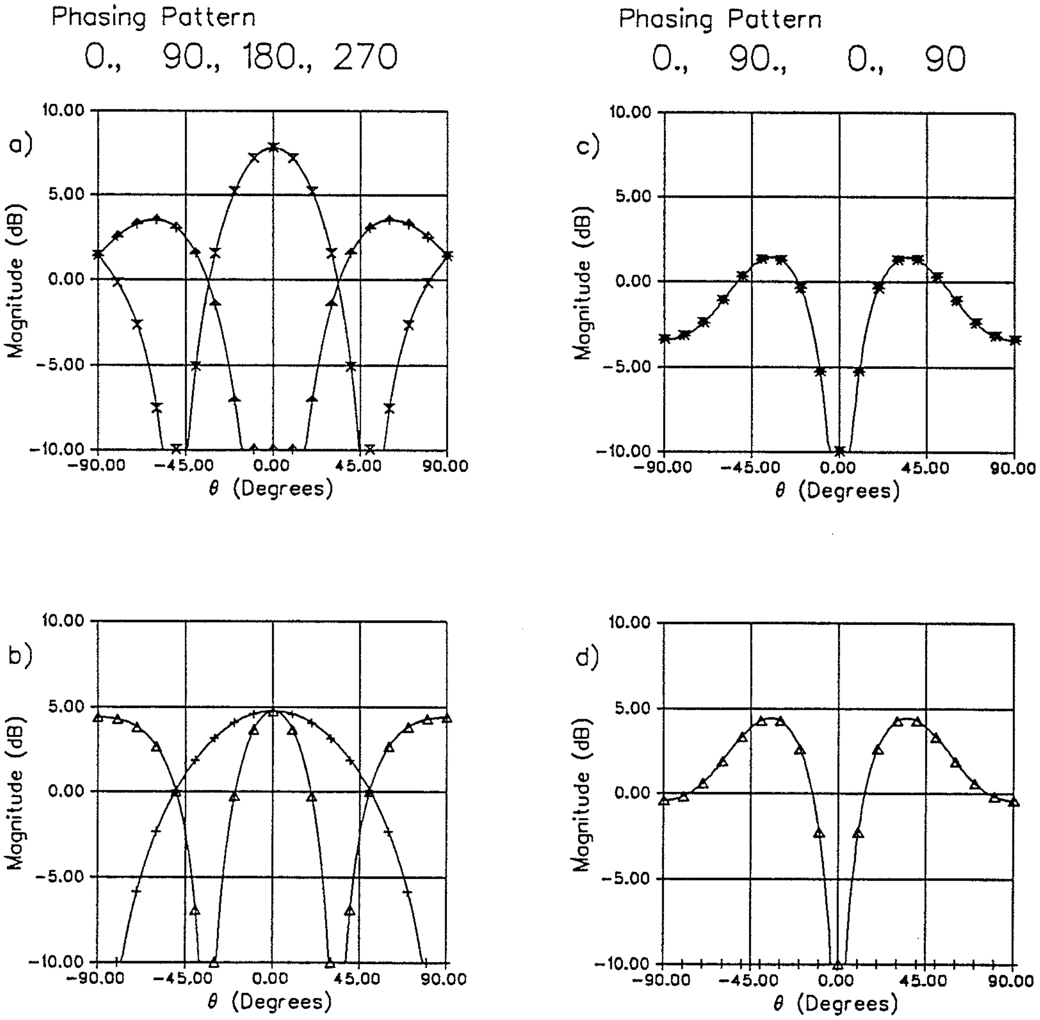
Phasing Pattern
0., 90., 180., 270

Phasing Pattern
0., 90., 0., 90

Figure 4.9 Theoretical radiation patterns for the dimensions listed above

a) $\varphi =$ 0, circularly polarized pattern, 0, 90, 180, 270 feeding pattern
b) $\varphi =$ 0, linearly polarized pattern, 0, 90, 180, 270 feeding pattern
c) $\varphi =$ 0, circularly polarized pattern, 0, 90, 0, 90 feeding pattern
d) $\varphi =$ 0, linearly polarized pattern, 0, 90, 0, 90 feeding pattern

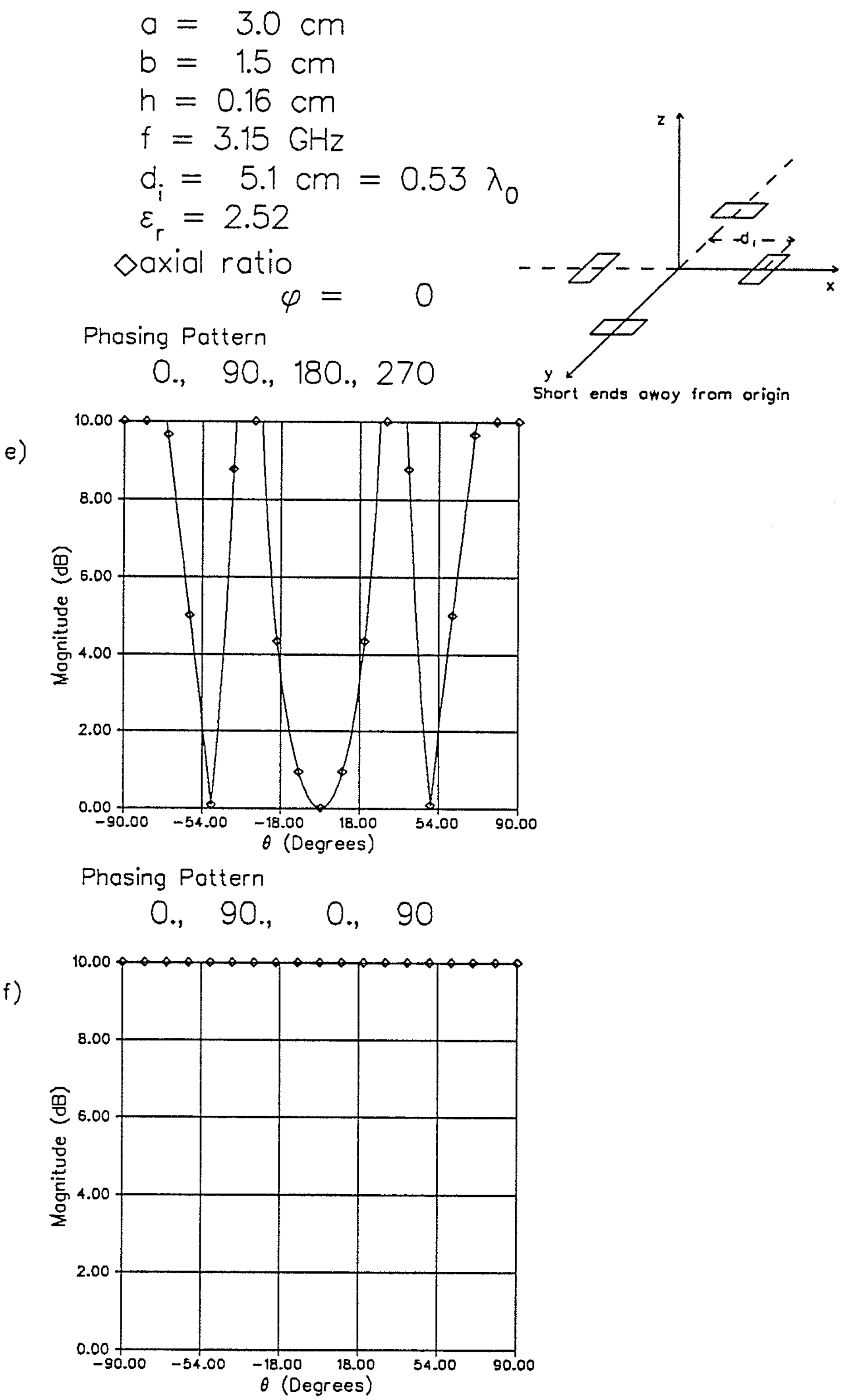

Figure 4.9 Theoretical radiation patterns for the dimensions listed above

e) φ = 0, Axial ratios for 0, 90, 180, 270 feeding pattern

f) φ = 0, Axial ratios for 0, 90, 0, 90 feeding pattern

$a = 3.0$ cm
$b = 1.5$ cm
$h = 0.16$ cm
$f = 3.15$ GHz
$d_i = 5.1$ cm $= 0.53\ \lambda_0$
$\varepsilon_r = 2.52$

Δ: E_θ
+: E_φ
✱: E_r
⊠: E_l

$\varphi = 45$

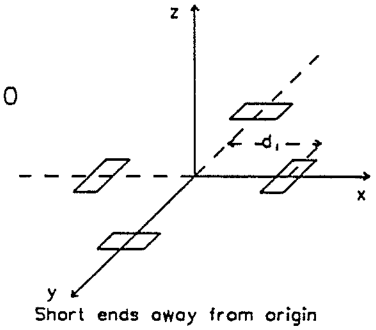

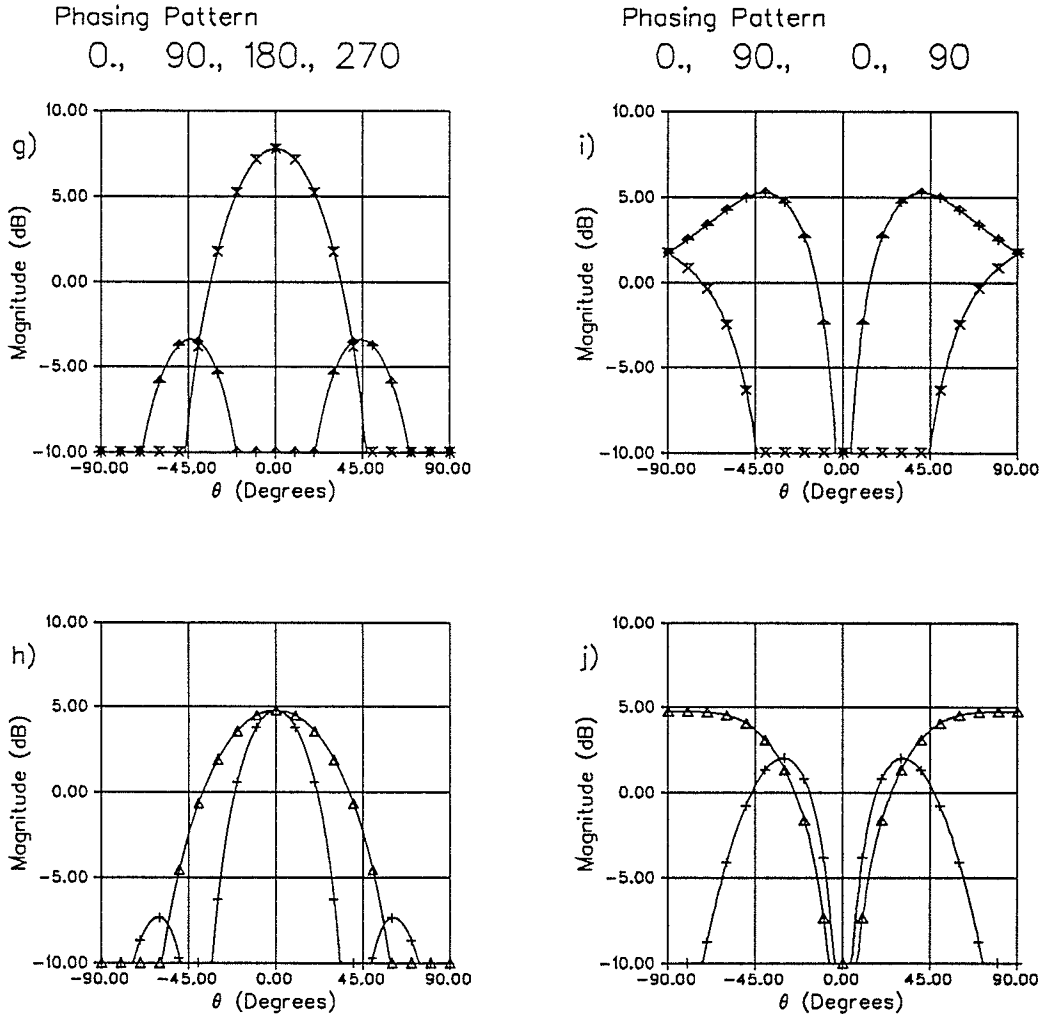

Figure 4.9 Theoretical radiation patterns for the dimensions listed above

g) φ = 45, circularly polarized pattern, 0, 90, 180, 270 feeding pattern
h) φ = 45, linearly polarized pattern, 0, 90, 180, 270 feeding pattern
i) φ = 45, circularly polarized pattern, 0, 90, 0, 90 feeding pattern
j) φ = 45, linearly polarized pattern, 0, 90, 0, 90 feeding pattern

$a = 3.0$ cm
$b = 1.5$ cm
$h = 0.16$ cm
$f = 3.15$ GHz
$d_i = 5.1$ cm $= 0.53\ \lambda_0$
$\varepsilon_r = 2.52$
◇axial ratio
$\varphi = 45$

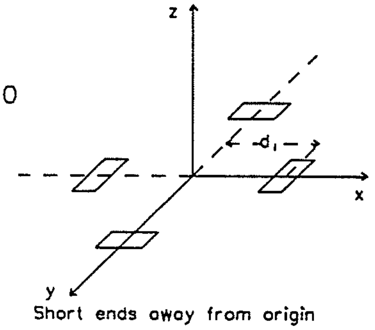

Phasing Pattern
0., 90., 180., 270

k)

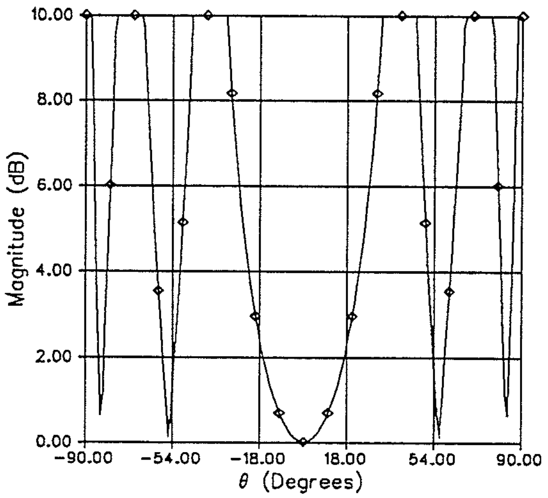

Phasing Pattern
0., 90., 0., 90

l)

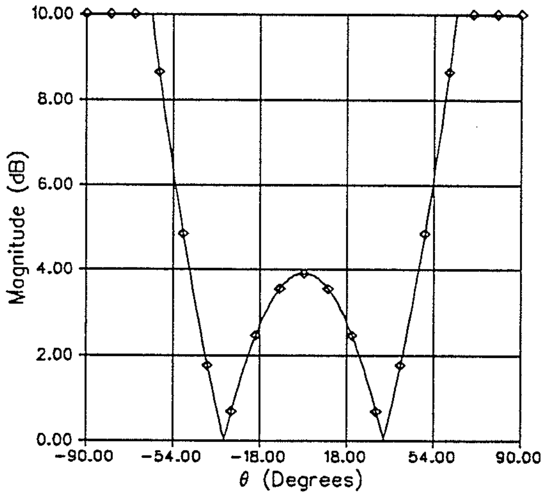

Figure 4.9 Theoretical radiation patterns for the dimensions listed above

k) $\varphi = 45$, Axial ratios for 0, 90, 180, 270 feeding pattern
l) $\varphi = 45$, Axial ratios for 0, 90, 0, 90 feeding pattern

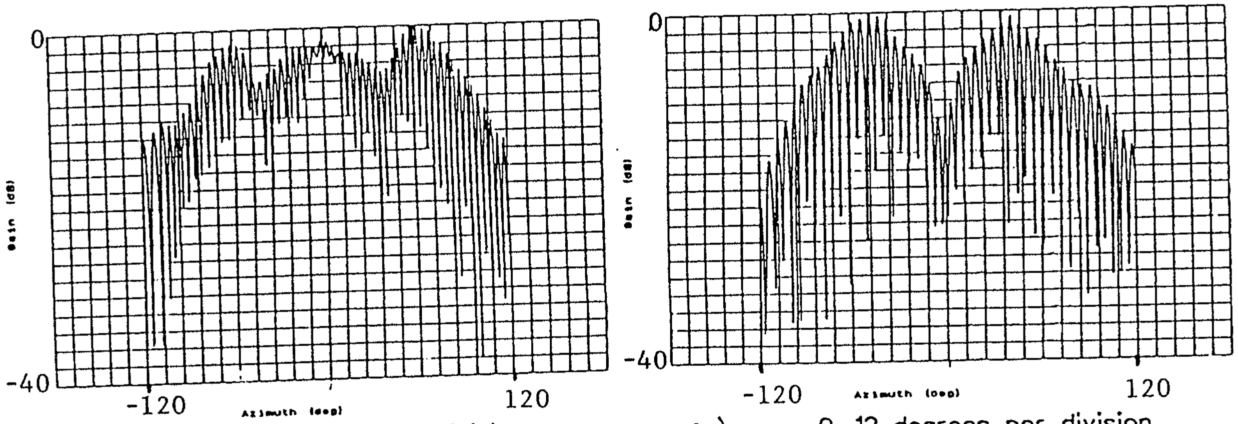

a) φ = 0, 12 degrees per division
Peak Gain = 2.92 dB, 2dB per division

b) φ = 0, 12 degrees per division
Peak Gain = 1.79 dB, 2dB per division

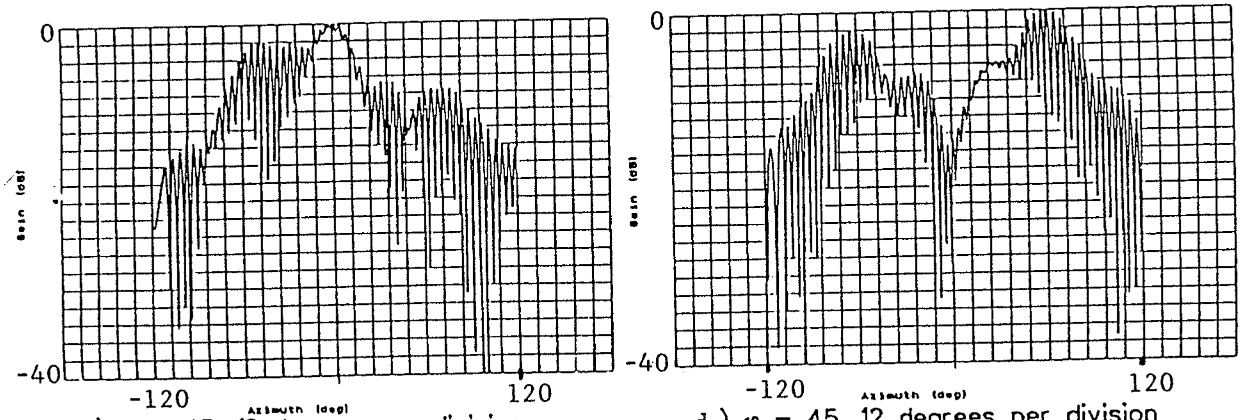

c) φ = 45, 12 degrees per division
Peak Gain = 1.74 dB, 2dB per division

d) φ = 45, 12 degrees per division
Peak Gain = 3.07 dB, 2dB per division

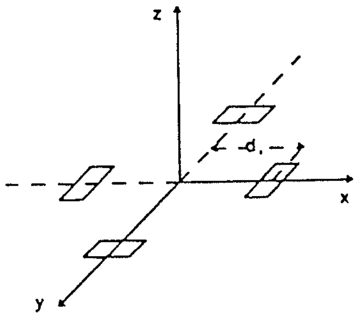

Short ends away from origin

$a = 3.00$ cm
$b = 1.50$ cm
$h = .16$ cm
$f = 2.75$ GHz
$d_i = 5.1$ cm
$= .53\ \lambda_0$
$\varepsilon_r = 2.52$

Figure 4.10 Experimental rotating linear radiation patterns for the dimensions listed
a) φ = 0: 0, 90, 180, 270 feed pattern b) φ = 0: 0, 90, 0, 90 feed pattern
b) φ = 45: 0, 90, 180, 270 feed pattern d) φ = 45: 0, 90, 0, 90 feed pattern

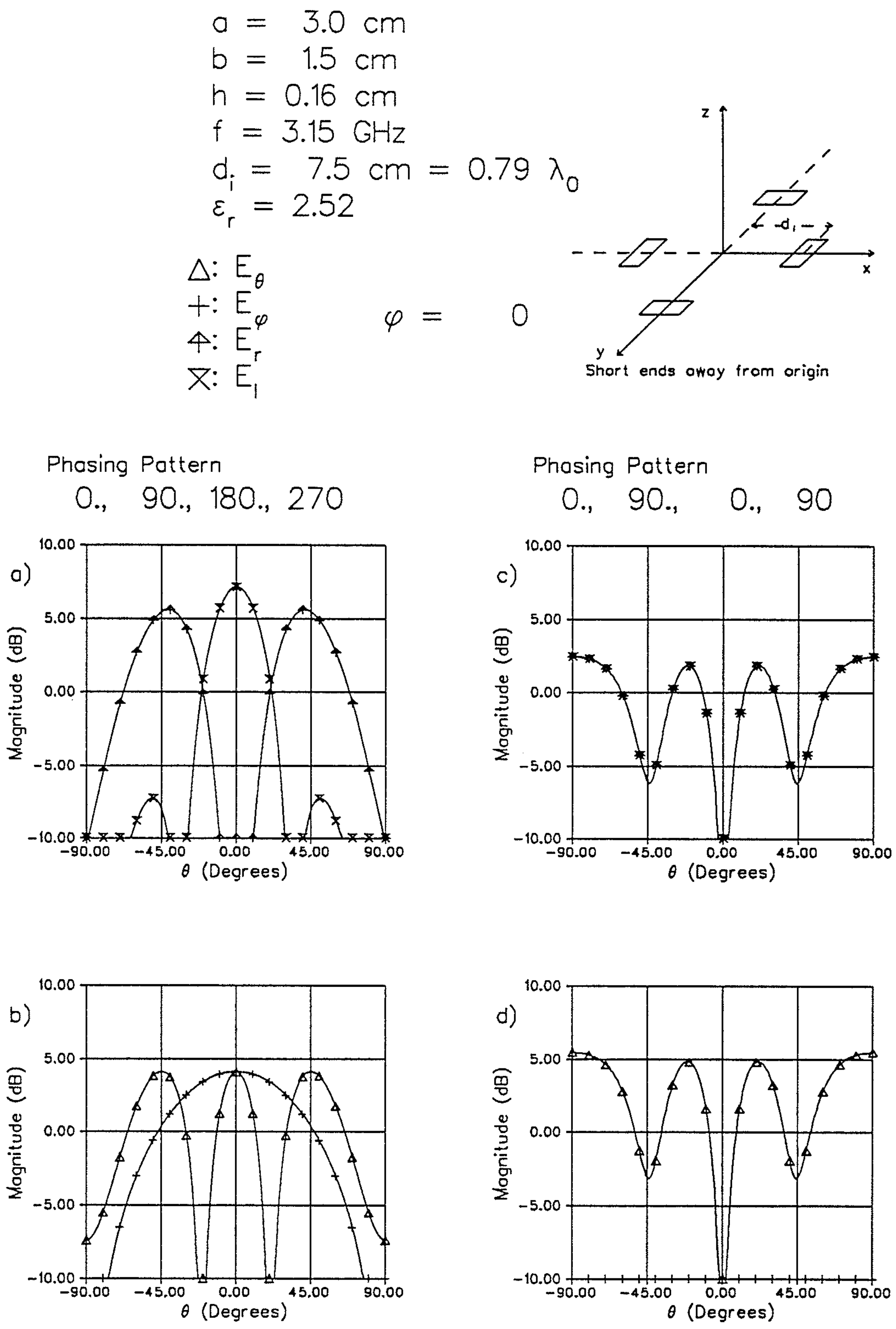

Figure 4.11Theoretical radiation patterns for the dimensions listed above

a) φ = 0, circularly polarized pattern, 0, 90, 180, 270 feeding pattern
b) φ = 0, linearly polarized pattern, 0, 90, 180, 270 feeding pattern
c) φ = 0, circularly polarized pattern, 0, 90, 0, 90 feeding pattern
d) φ = 0, linearly polarized pattern, 0, 90, 0, 90 feeding pattern

$a = 3.0$ cm
$b = 1.5$ cm
$h = 0.16$ cm
$f = 3.15$ GHz
$d_i = 7.5$ cm $= 0.79\ \lambda_0$
$\varepsilon_r = 2.52$
◇axial ratio
$\varphi = 0$

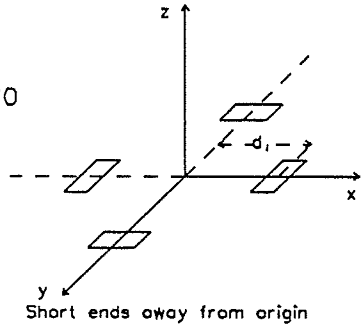

Phasing Pattern
0., 90., 180., 270

e)

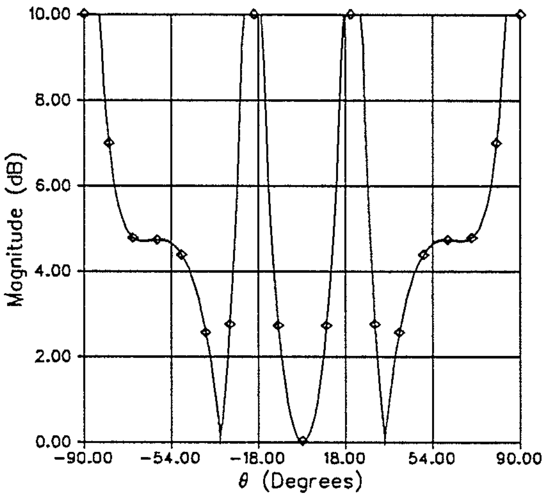

Phasing Pattern
0., 90., 0., 90

f)

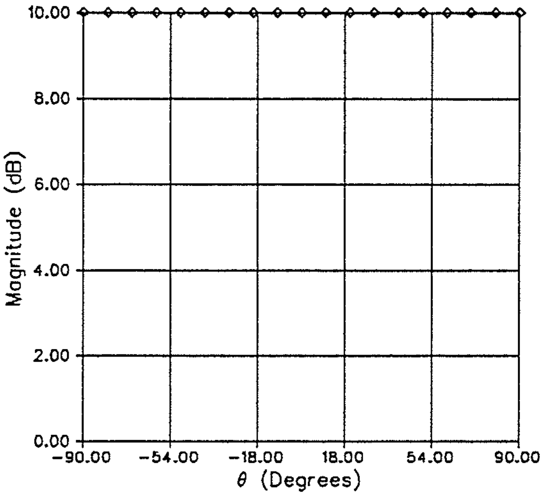

Figure 4.11Theoretical radiation patterns for the dimensions listed above

e) $\varphi =$ 0, Axial ratios for 0, 90, 180, 270 feeding pattern
f) $\varphi =$ 0, Axial ratios for 0, 90, 0, 90 feeding pattern

$a = 3.0$ cm
$b = 1.5$ cm
$h = 0.16$ cm
$f = 3.15$ GHz
$d_i = 7.5$ cm $= 0.79\ \lambda_0$
$\varepsilon_r = 2.52$

△: E_θ
+: E_φ
✢: E_r
⊠: E_l

$\varphi = 45$

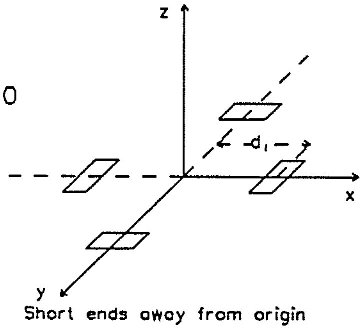

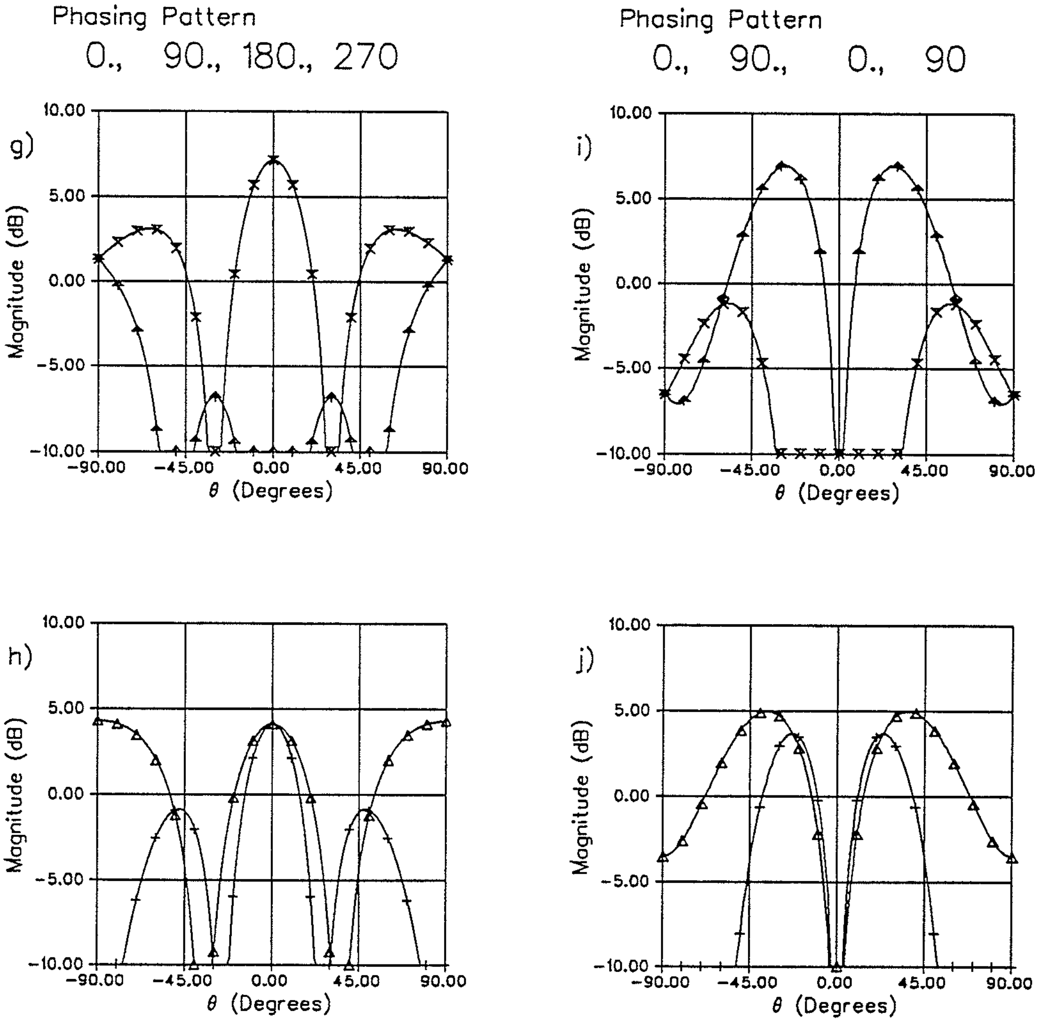

Figure 4.11 Theoretical radiation patterns for the dimensions listed above

g) $\varphi = 45$, circularly polarized pattern, 0, 90, 180, 270 feeding pattern
h) $\varphi = 45$, linearly polarized pattern, 0, 90, 180, 270 feeding pattern
i) $\varphi = 45$, circularly polarized pattern, 0, 90, 0, 90 feeding pattern
j) $\varphi = 45$, linearly polarized pattern, 0, 90, 0, 90 feeding pattern

$a = 3.0$ cm
$b = 1.5$ cm
$h = 0.16$ cm
$f = 3.15$ GHz
$d_i = 7.5 \text{ cm} = 0.79\ \lambda_0$
$\varepsilon_r = 2.52$
◇axial ratio
$\varphi = 45$

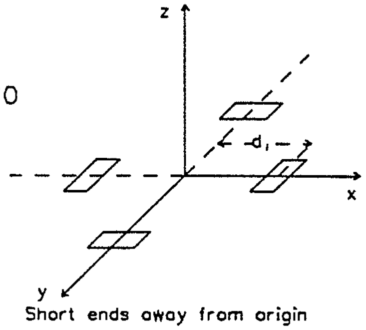

Phasing Pattern
0., 90., 180., 270

k)

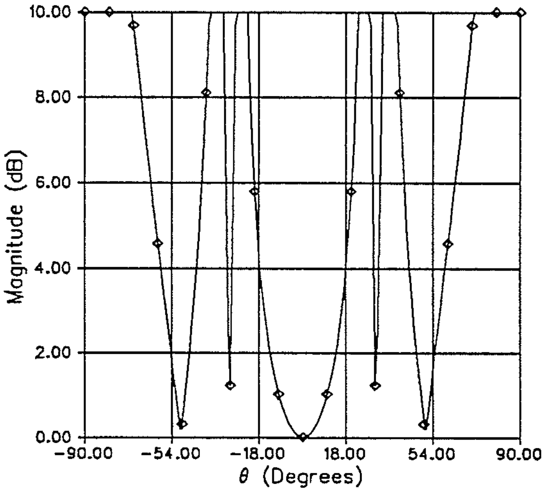

Phasing Pattern
0., 90., 0., 90

l)

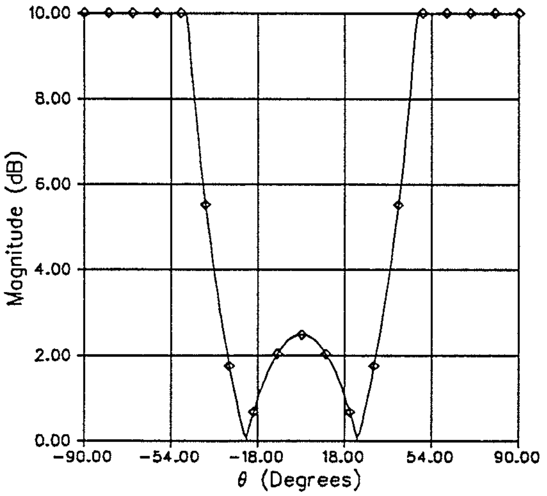

Figure4.11 Theoretical radiation patterns for the dimensions listed above

k) $\varphi = 45$, Axial ratios for 0, 90, 180, 270 feeding pattern
l) $\varphi = 45$, Axial ratios for 0, 90, 0, 90 feeding pattern

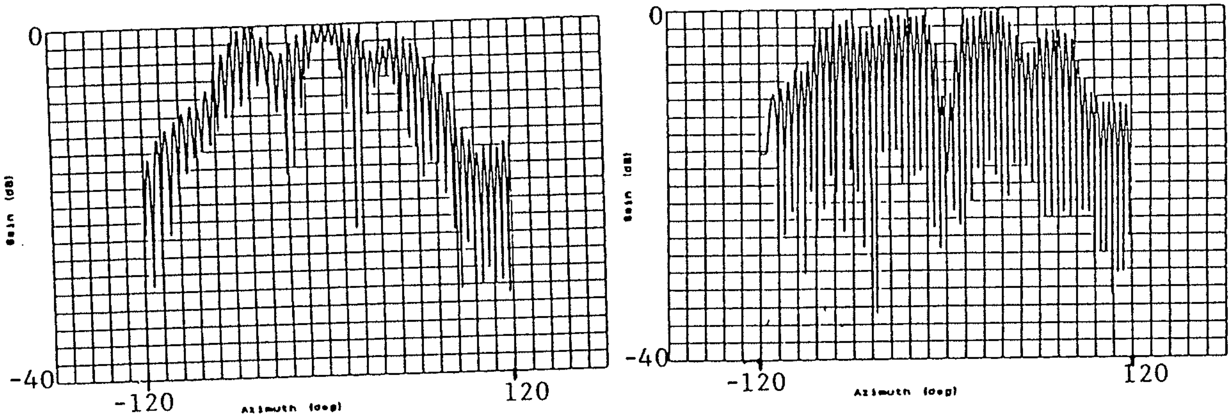

a) φ = 0, 12 degrees per division
Peak Gain = 1.94 dB, 2dB per division

b) φ = 0, 12 degrees per division
Peak Gain = 1.35 dB, 2dB per division

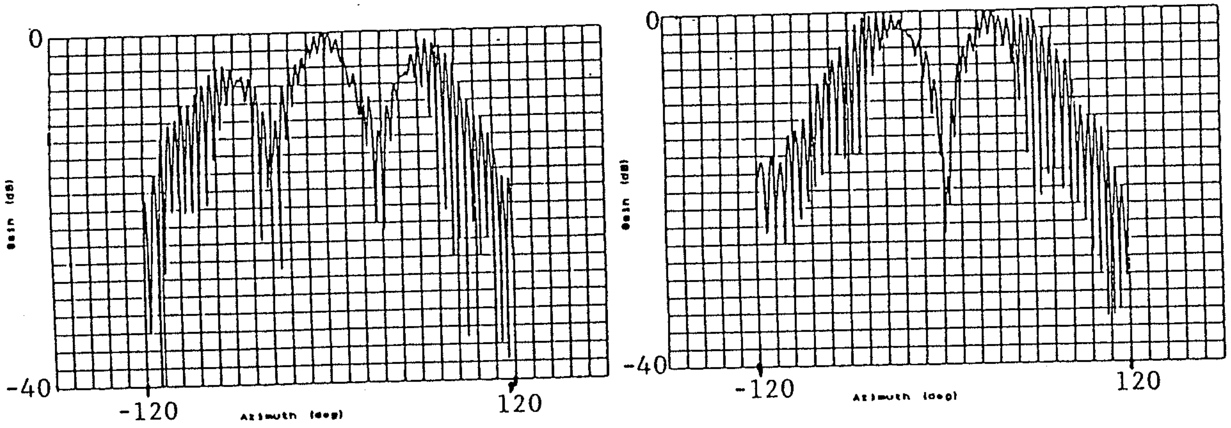

c) φ = 45, 12 degrees per division
Peak Gain = 2.13 dB, 2dB per division

d) φ = 45, 12 degrees per division
Peak Gain = 1.94 dB, 2dB per division

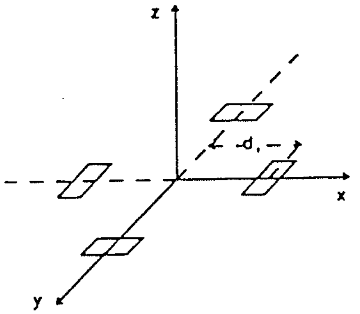

Short ends away from origin

$a = 3.00$ cm
$b = 1.50$ cm
$h = .16$ cm
$f = 2.75$ GHz
$d_i = 7.5$ cm
$= .79\ \lambda_0$
$\varepsilon_r = 2.52$

Figure 4.12 Experimental rotating linear radiation patterns for the dimensions listed
a) φ = 0: 0, 90, 180, 270 feed pattern b) φ = 0: 0, 90, 0, 90 feed pattern
c) φ = 45: 0, 90, 180, 270 feed pattern d) φ = 45: 0, 90, 0, 90 feed pattern

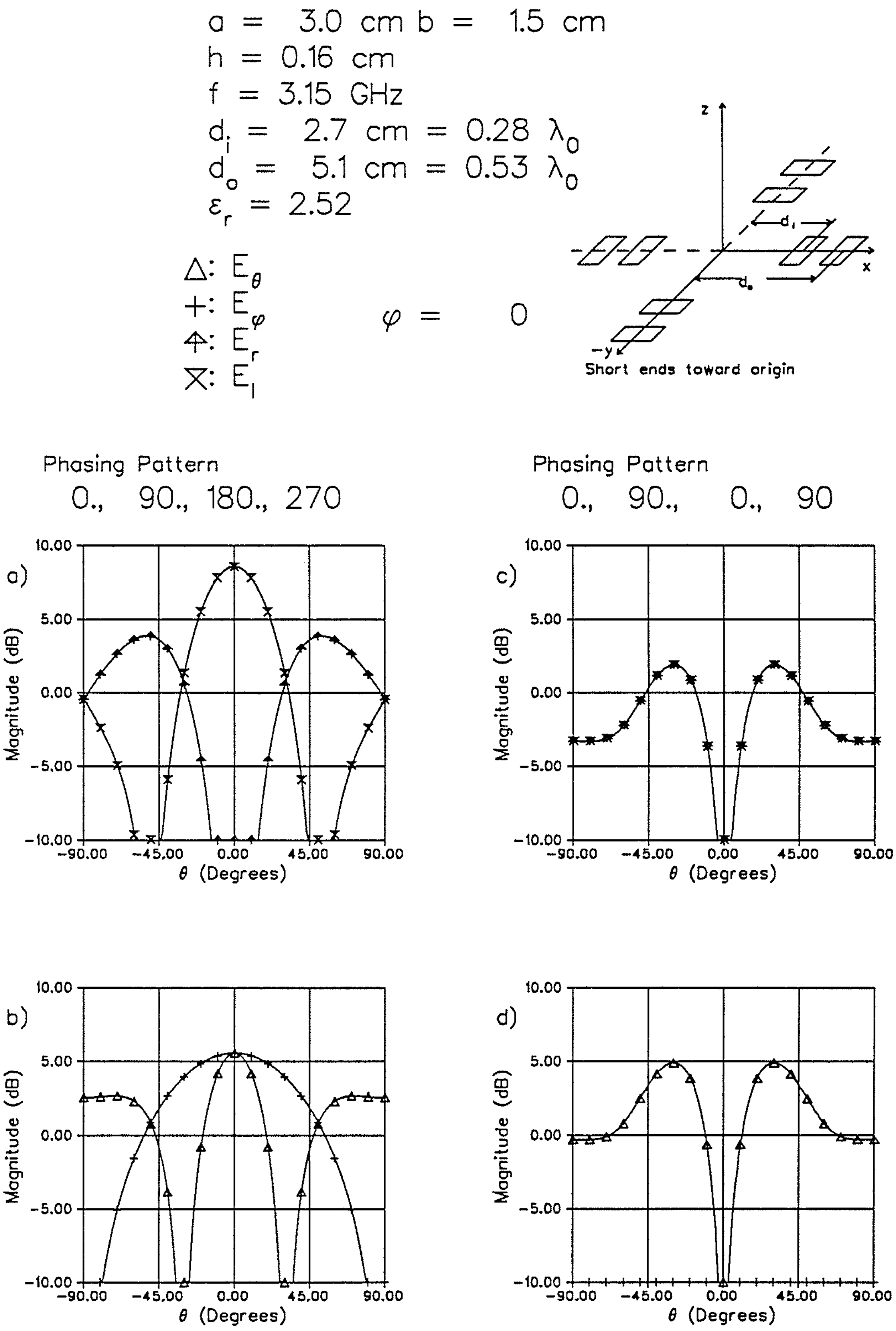

$a = 3.0$ cm $b = 1.5$ cm
$h = 0.16$ cm
$f = 3.15$ GHz
$d_i = 2.7$ cm $= 0.28\ \lambda_0$
$d_o = 5.1$ cm $= 0.53\ \lambda_0$
$\varepsilon_r = 2.52$

△: E_θ
+: E_φ
✧: E_r
⩙: E_l

$\varphi = 0$

Figure 4.13 Theoretical radiation patterns for the dimensions listed above

a) $\varphi =$ 0, circularly polarized pattern, 0, 90, 180, 270 feeding pattern
b) $\varphi =$ 0, linearly polarized pattern, 0, 90, 180, 270 feeding pattern
c) $\varphi =$ 0, circularly polarized pattern, 0, 90, 0, 90 feeding pattern
d) $\varphi =$ 0, linearly polarized pattern, 0, 90, 0, 90 feeding pattern

a = 3.0 cm b = 1.5 cm

h = 0.16 cm

f = 3.15 GHz

d_i = 2.7 cm = 0.28 λ_0

d_o = 5.1 cm = 0.53 λ_0

ε_r = 2.52

◇axial ratio

φ = 0

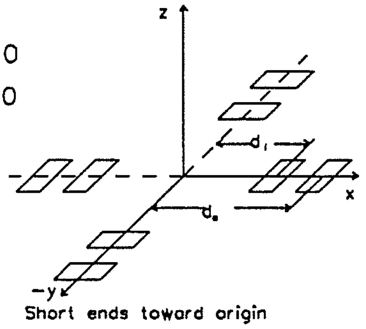

Phasing Pattern

0., 90., 180., 270

e)

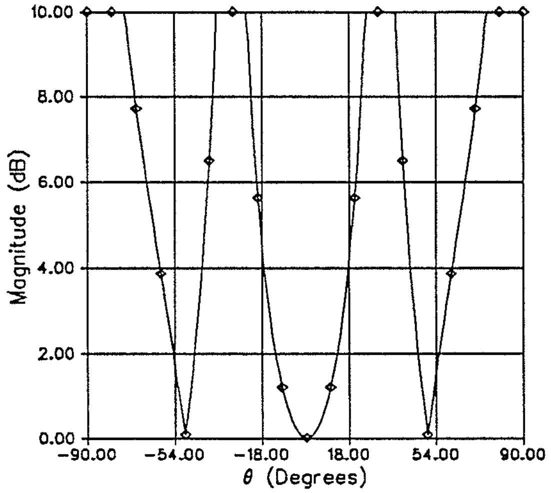

Phasing Pattern

0., 90., 0., 90

f)

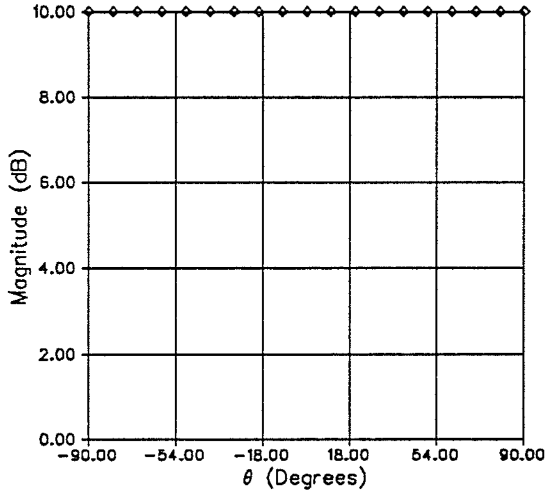

Figure 4.13 Theoretical radiation patterns for the dimensions listed above

e) φ = 0, Axial ratios for 0, 90, 180, 270 feeding pattern

f) φ = 0, Axial ratios for 0, 90, 0, 90 feeding pattern

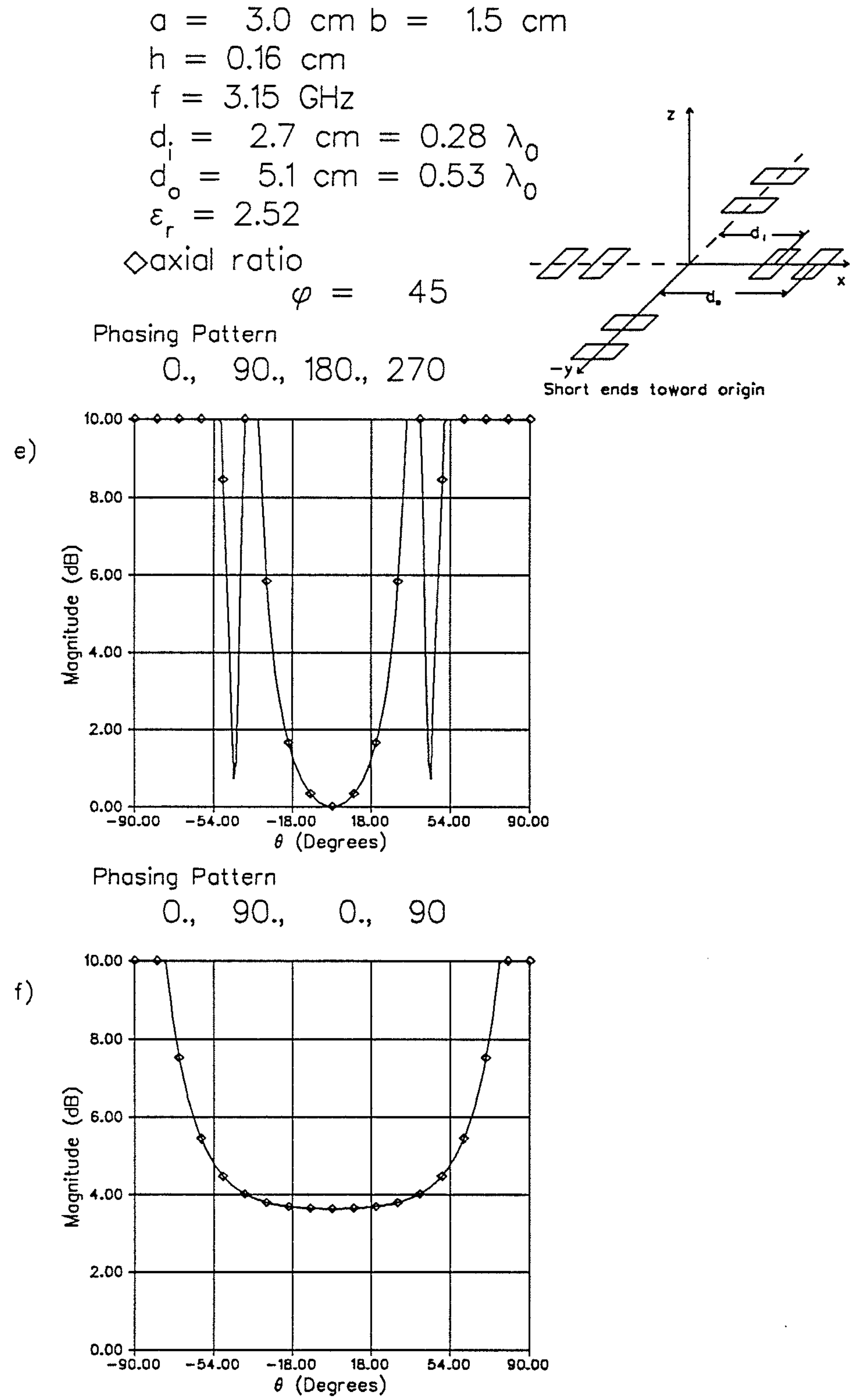

Figure 4.13 Theoretical radiation patterns for the dimensions listed above

e) φ = 0, Axial ratios for 0, 90, 180, 270 feeding pattern
f) φ = 0, Axial ratios for 0, 90, 0, 90 feeding pattern

$a = 3.0$ cm $b = 1.5$ cm
$h = 0.16$ cm
$f = 3.15$ GHz
$d_i = 2.7$ cm $= 0.28\ \lambda_0$
$d_o = 5.1$ cm $= 0.53\ \lambda_0$
$\varepsilon_r = 2.52$

△: E_θ
+: E_φ
4̂: E_r
⩙: E_l

$\varphi = 45$

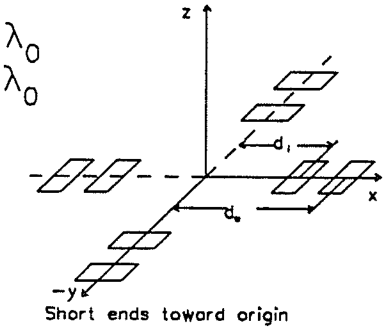

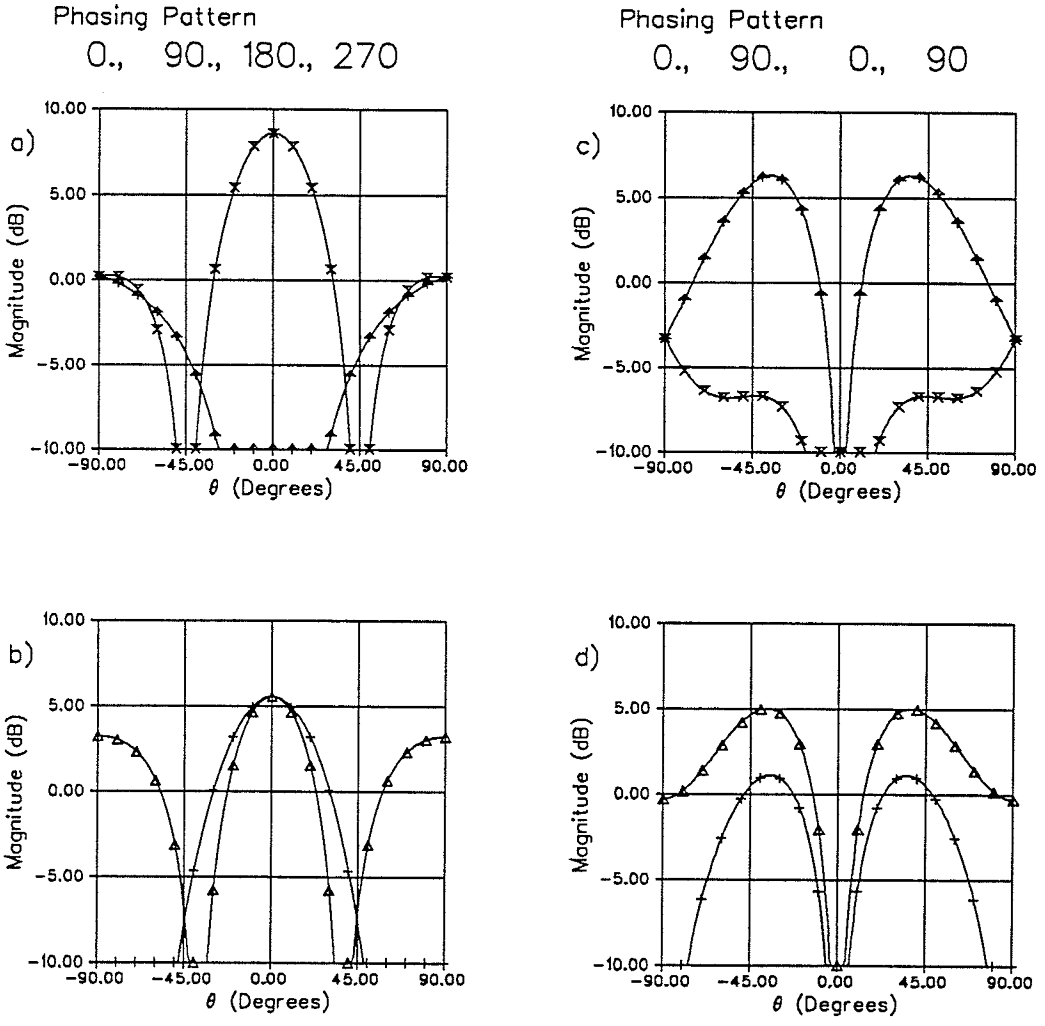

Figure 4.13 Theoretical radiation patterns for the dimensions listed above

a) $\varphi =$ 0, circularly polarized pattern, 0, 90, 180, 270 feeding pattern
b) $\varphi =$ 0, linearly polarized pattern, 0, 90, 180, 270 feeding pattern
c) $\varphi =$ 0, circularly polarized pattern, 0, 90, 0, 90 feeding pattern
d) $\varphi =$ 0, linearly polarized pattern, 0, 90, 0, 90 feeding pattern

$a = 3.0$ cm
$b = 1.5$ cm
$h = 0.16$ cm
$f = 3.15$ GHz
$d_i = 5.1$ cm $= 0.53\ \lambda_0$
$\varepsilon_r = 2.52$

△: E_θ
+: E_φ
⊕: E_r
⊠: E_l
◇axial ratio

$\varphi = 0$

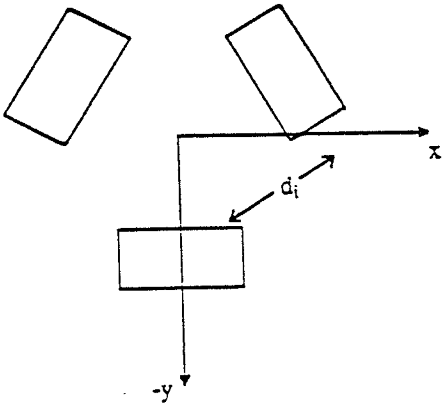

Phasing Pattern
0., 120.,−120.,

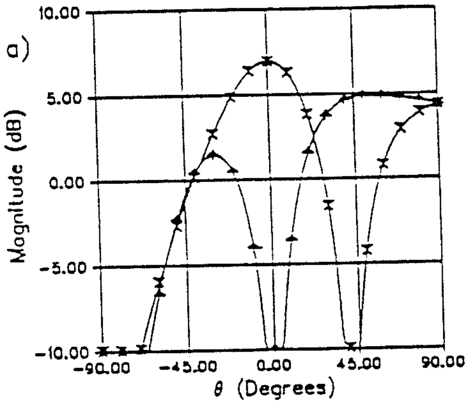

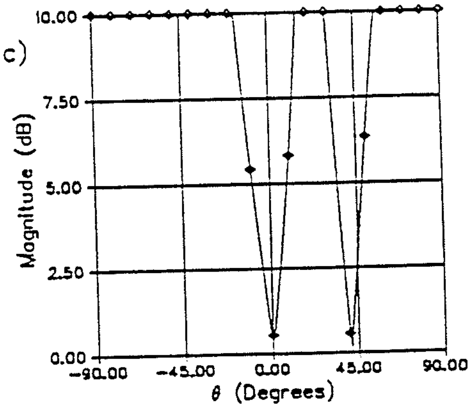

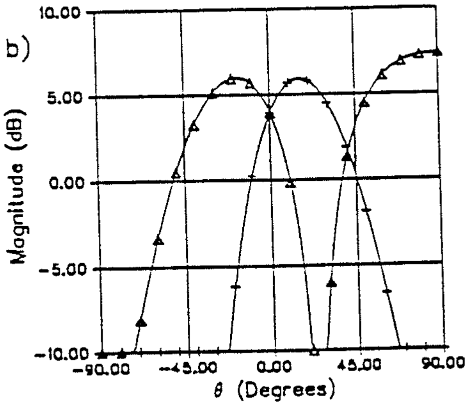

Figure 4.14 Theoretical radiation patterns for the dimensions listed above

a) $\varphi =$ 0, circularly polarized, 0, 120, −120, feeding pattern
b) $\varphi =$ 0, linearly polarized, 0, 120, −120, feeding pattern
c) $\varphi =$ 0, Axial ratios for 0, 120, −120, feeding pattern

$a = 3.0$ cm
$b = 1.5$ cm
$h = 0.16$ cm
$f = 3.15$ GHz
$d_i = 5.1 \text{ cm} = 0.53\ \lambda_0$
$\varepsilon_r = 2.52$

△: E_θ
+: E_φ
$\varphi = 90$
△: E_r
⨯: E_l
◇axial ratio

Phasing Pattern
0., 120.,−120.,

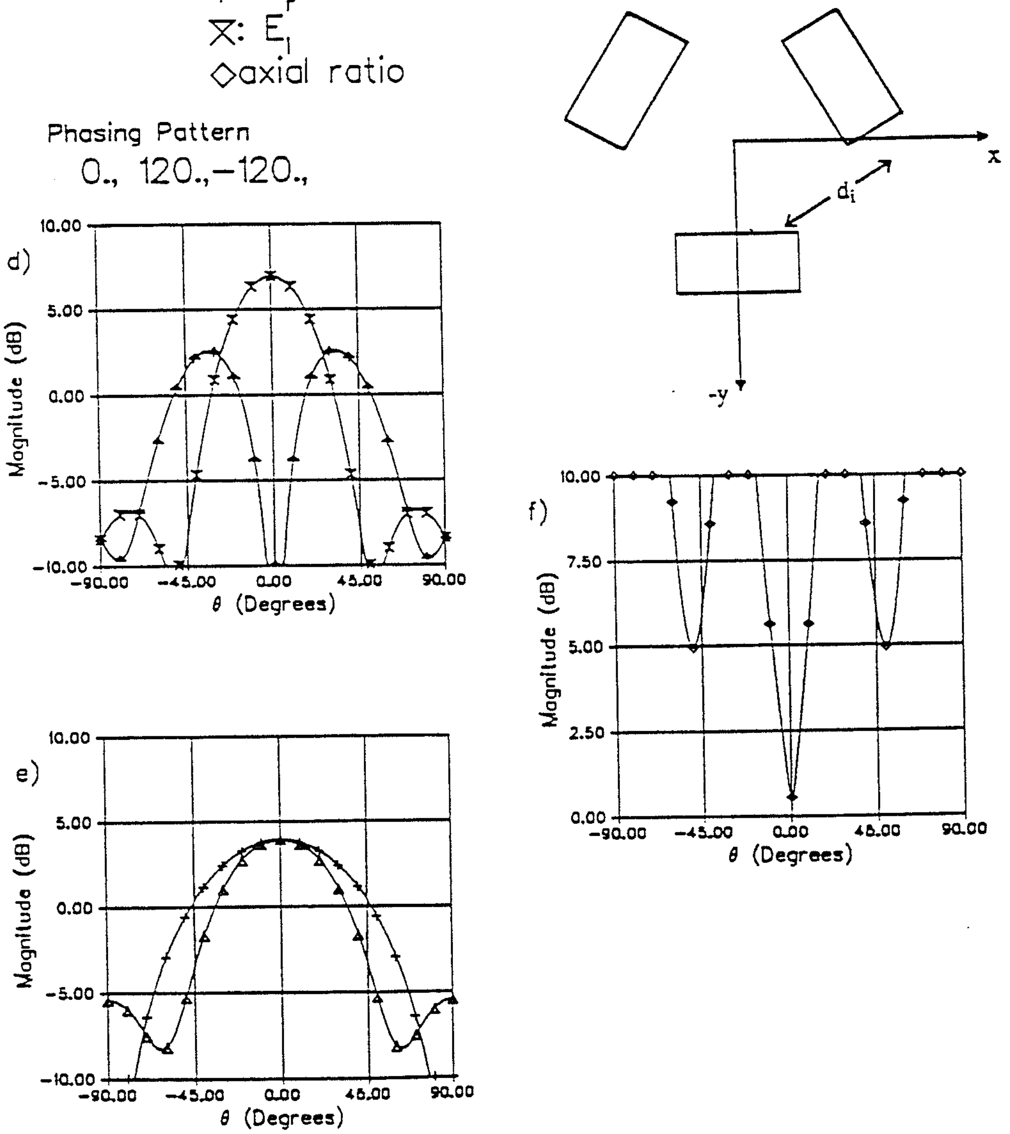

Figure 4.14 Theoretical radiation patterns for the dimensions listed above
d) φ = 90, circularly polarized, 0, 120, −120, feeding pattern
e) φ = 90, linearly polarized, 0, 20, −120, feeding pattern
f) φ = 90, Axial ratios for 0, 120, −120, feeding pattern

$a = 3.0$ cm
$b = 1.5$ cm
$h = 0.16$ cm
$f = 3.15$ GHz
$d_i = 5.1 \text{ cm} = 0.53\ \lambda_0$
$\varepsilon_r = 2.52$

△: E_θ
+: E_φ $\varphi = 0$
✦: E_r
⧖: E_l
◇axial ratio

Phasing Pattern
0., 60., 120., 180., −120., −60.

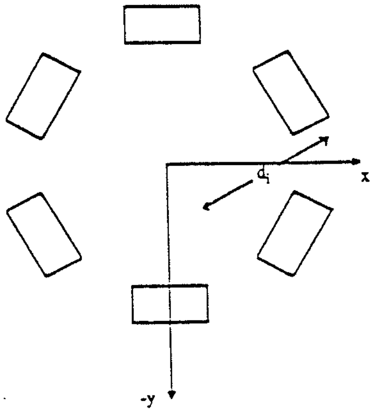

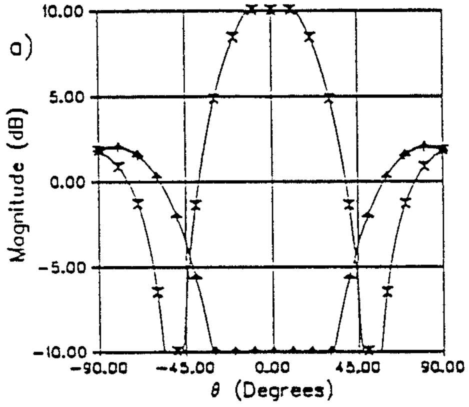

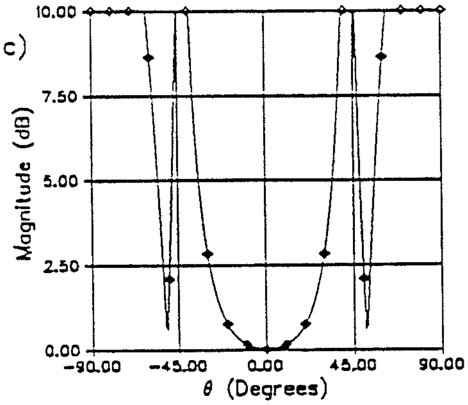

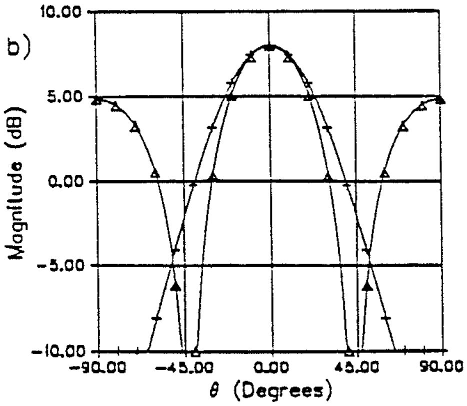

Figure 4.15 Theoretical radiation patterns for the dimensions listed above

a) $\varphi = 0$, circularly polarized, 0, 60, 120, 180, −120, −60, feeding pattern
b) $\varphi = 0$, linearly polarized, 0, 60, 120, 180, −120, −60, feeding pattern
c) $\varphi = 0$, Axial ratios for 0, 60, 120, 180, −120, −60, feeding pattern

$a = 3.0$ cm
$b = 1.5$ cm
$h = 0.16$ cm
$f = 3.15$ GHz
$d_i = 5.1$ cm $= 0.53\ \lambda_0$
$\varepsilon_r = 2.52$

△: E_θ
+: E_φ $\qquad \varphi = 90$
⩚: E_r
⧖: E_l
◇axial ratio

Phasing Pattern
0., 60., 120., 180., −120., −60.

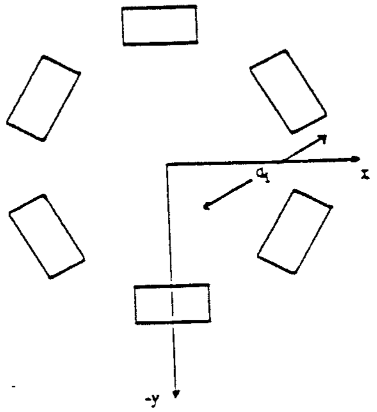

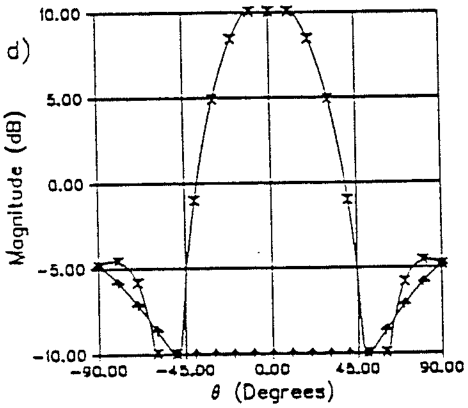

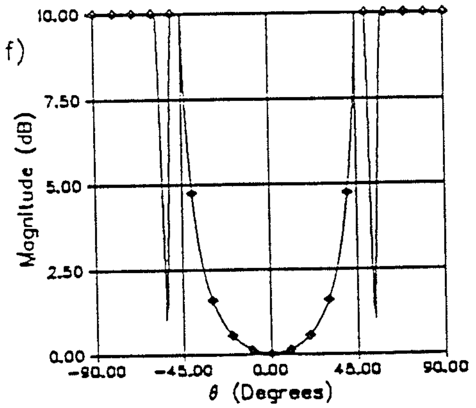

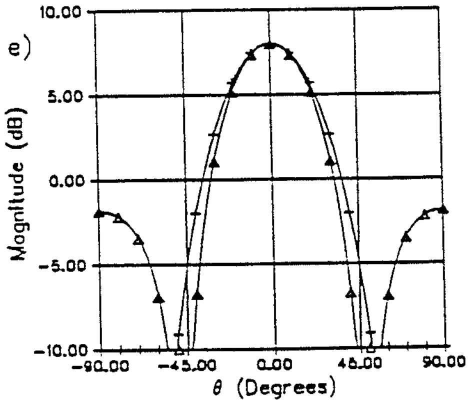

Figure 4.15 Theoretical radiation patterns for the dimensions listed above

d) φ = 90, circularly polarized, 0, 60, 120, 180, −120, −60, feeding pattern
e) φ = 90, linearly polarized, 0, 60, 120, 180, −120, −60, feeding pattern
f) φ = 90, Axial ratios for 0, 60, 120, 180, −120, −60, feeding pattern

4.5.2 Radiation Patterns as a Function of Frequency

In addition to calculating the radiation patterns at the resonant frequency (as calculated by equation (2.16)), theoretical results were evaluated at 80%, 90%, 110% and 120% of the resonant frequency. The beam characteristics, such as peak magnitude, -3 dB beamwidth, range of acceptable axial ratio (≤ 3 dB), have been plotted below. Figures 4.16 to 4.18 show the characteristics of the main beam in both the $\phi = 0°$ plane and the $\phi = 45°$ plane, using the 0° 90°, 180°, 270° feeding arrangement for each of the three values of d_i. Since the peak in each of the planes occurs at $\theta = 0°$, which is the same point for each of the planes, the peak value will be the same, and the plots of the magnitude of E_l will overlap. In addition, the beamwidths for each of the planes are identical for $d_i = 5.1$ cm and 7.5 cm, and thus these plots overlap.

Figures 4.19 and 4.20 show the sidelobe characteristics in the $\phi = 0°$ plane for $d_i = 5.1$ cm and in both the $\phi = 0°$ plane and the $\phi = 45°$ plane for $d_i = 7.5$ cm, using the 0° 90°, 180°, 270° feeding arrangement. In the $\phi = 0°$ plane the sidelobes are right hand circularly polarized, while in the $\phi = 45°$ plane, they are left hand circularly polarized.

Figures 4.21 to 4.23 show the sidelobe characteristics in the $\phi = 45°$ plane for $d_i = 2.7$, 5.1 and 7.5 cm using the 0° 90°, 0°, 90° feeding arrangement. The sidelobes are right hand circularly polarized.

Figures 4.24 and 4.25 show the range over which the axial ratio is ≤ 3 dB in both the $\phi = 0°$ and $\phi = 45°$ planes for $d_i = 2.7$, 5.1 and 7.5 cm using the 0° 90°, 180°, 270° feeding arrangement.These ranges are all centered about $\theta = 0°$.

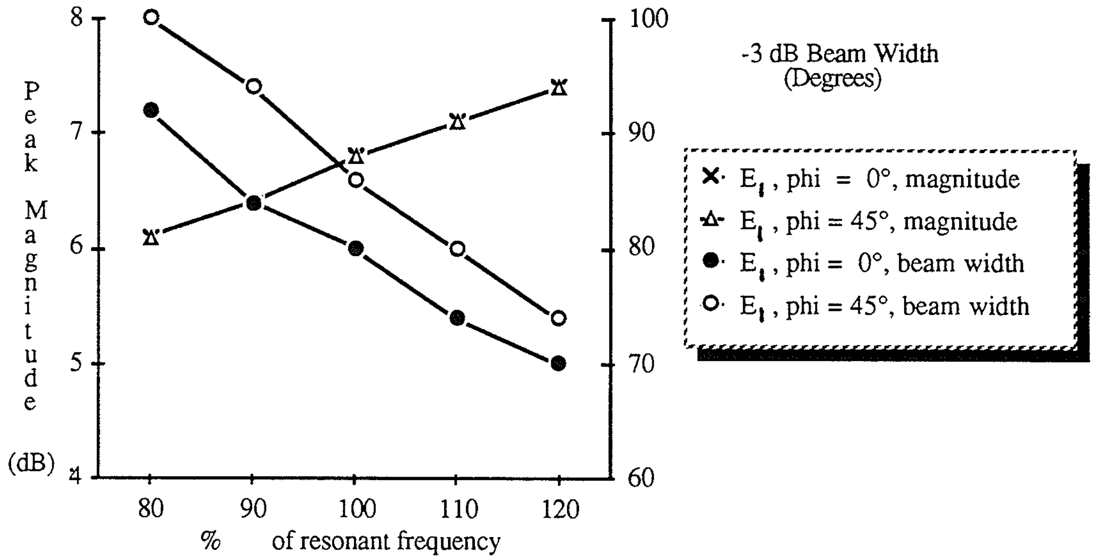

Figure 4.16 Main beam peak magnitude and beamwidth for $d_i = 2.7$ cm. in the $\phi = 0°$ and $\phi=45°$ planes using the 0°, 90°, 180°, 270° feeding pattern. Electric field component is E_l.

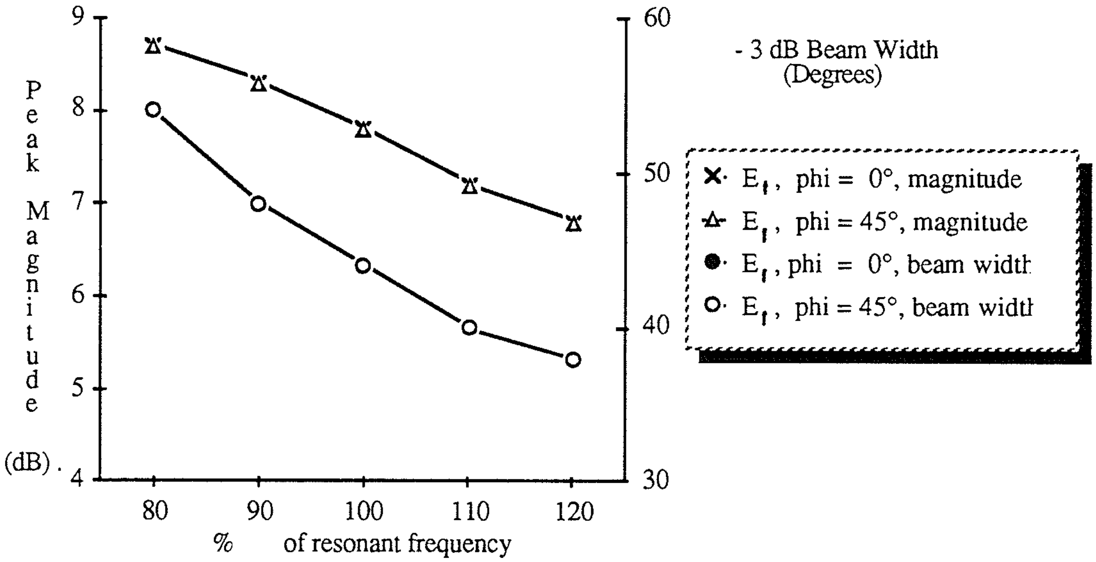

Figure 4.17 Main beam peak magnitude and beamwidth for $d_i = 5.1$ cm. in the $\phi = 0°$ and $\phi=45°$ planes using the 0°, 90°, 180°, 270° feeding pattern Electric field component is E_l.

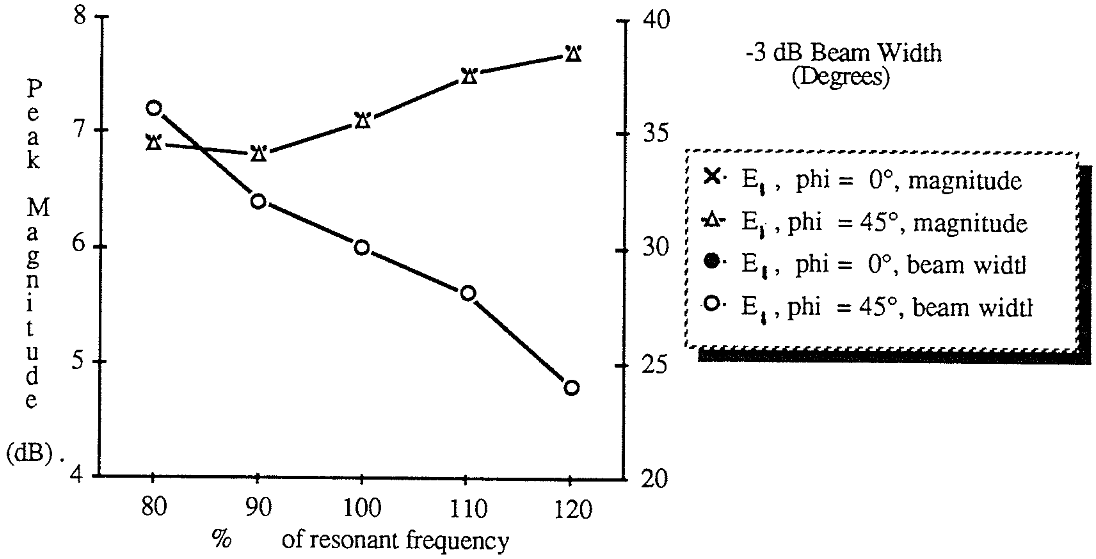

Figure 4.18 Main beam peak magnitude and beamwidth for $d_i = 7.5$ cm. in the $\phi = 0°$ and $\phi=45°$ planes using the 0°, 90°, 180°, 270° feeding pattern Electric field component is E_l.

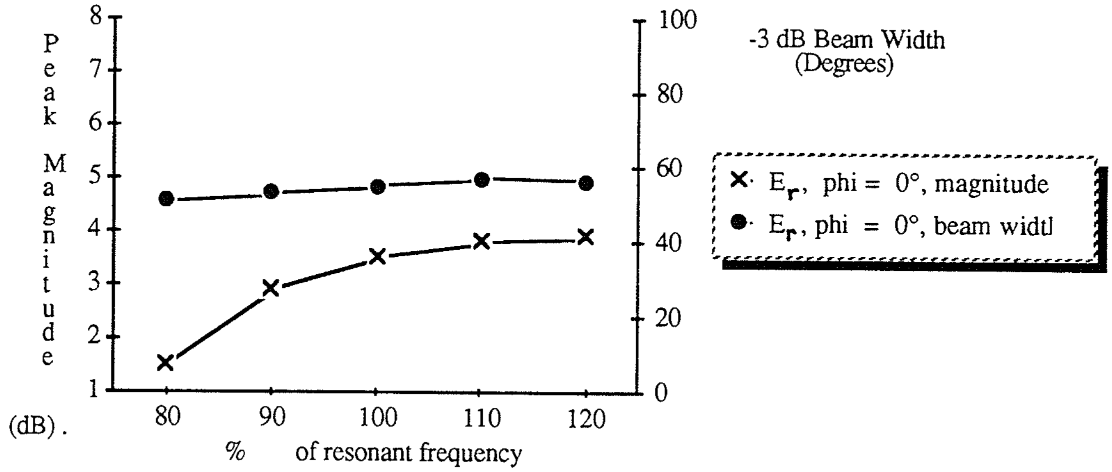

Figure 4.19 Sidelobe peak magnitude and beamwidth for $d_i = 5.7$ cm. in the $\phi = 0°$ plane using the 0°, 90°, 180°, 270° feeding pattern Electric field component is E_r.

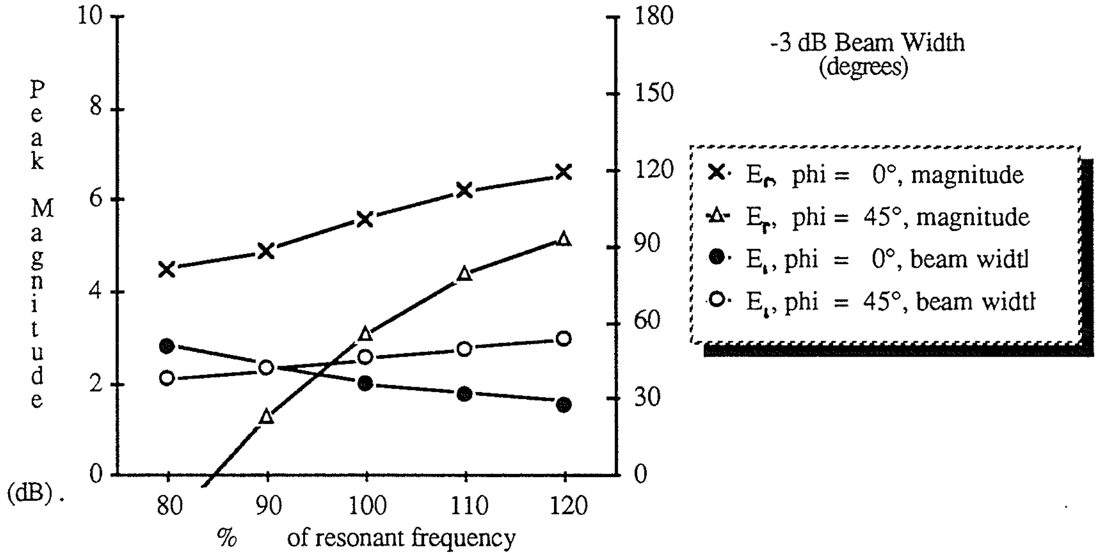

Figure 4.20 Sidelobe peak magnitude and beamwidth for d_i = 7.5 cm. in the $\phi = 0°$ and $\phi=45°$ planes using the 0°, 90°, 180°, 270° feeding pattern

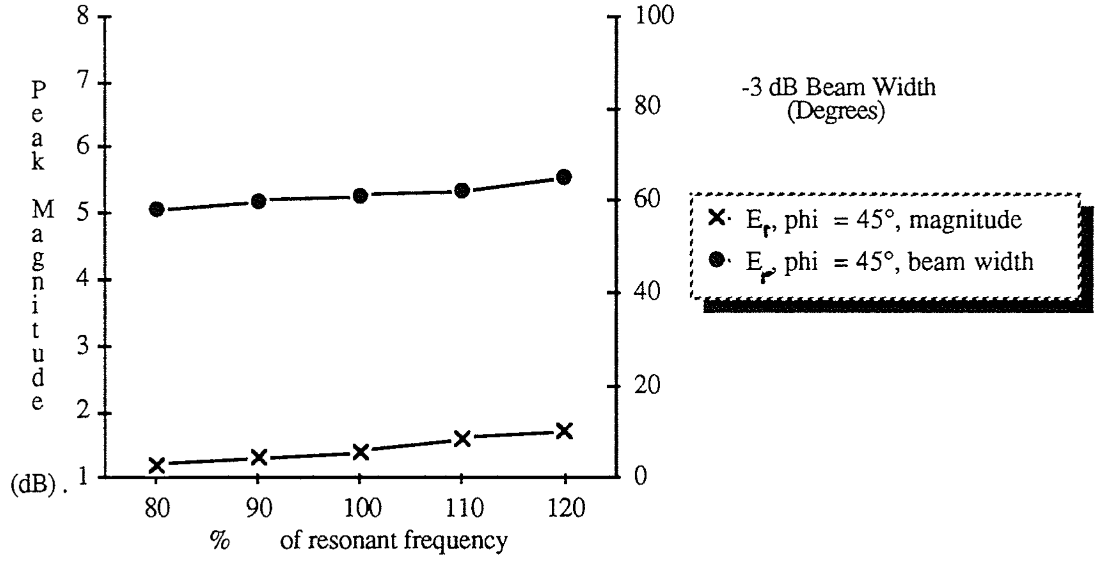

Figure 4.21 Sidelobe peak magnitude and beamwidth for d_i = 2.7 cm. in the $\phi = 45°$ plane using the 0°, 90°, 0°, 90° feeding pattern. Electric field component is E_T.

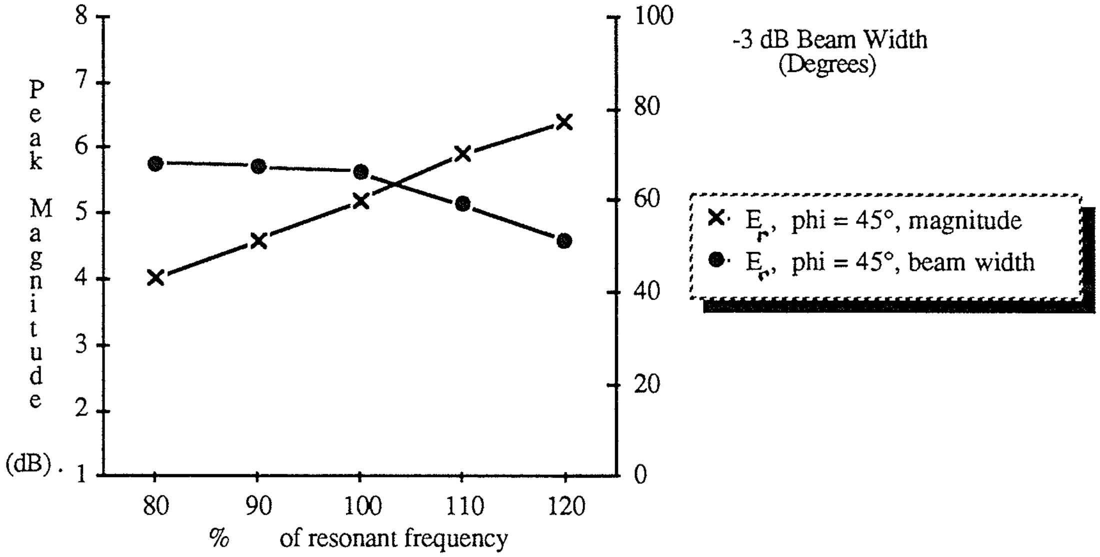

Figure 4.22 Sidelobe peak magnitude and beamwidth for d_i = 5.1 cm. in the $\phi = 45°$ plane using the 0°, 90°, 0°, 90° feeding pattern. Electric field component is E_r.

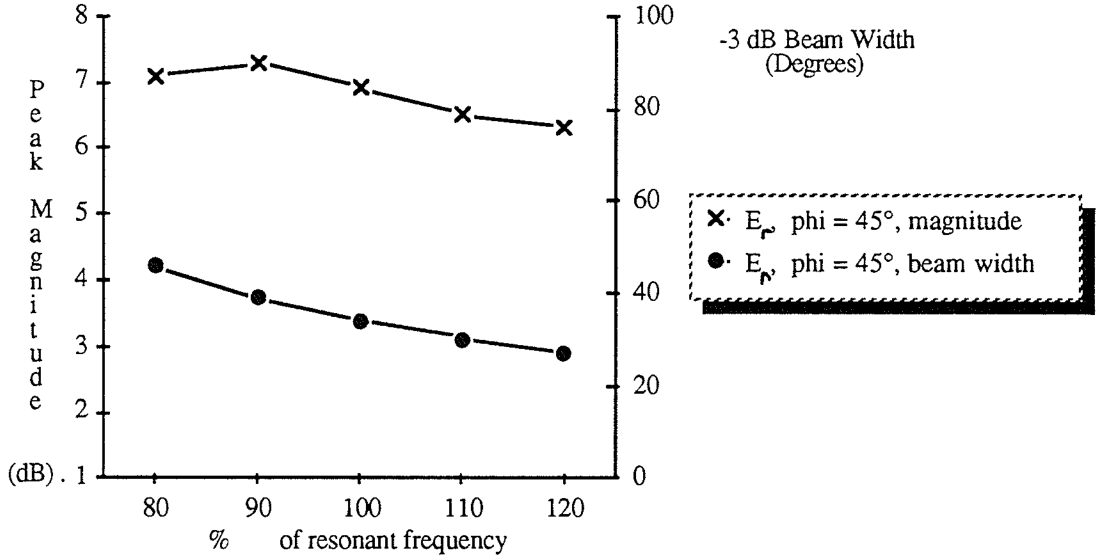

Figure 4.23 Sidelobe peak magnitude and beamwidth for d_i = 7.5 cm. in the $\phi = 45°$ plane using the 0°, 90°, 0°, 90° feeding pattern Electric field component is E_r.

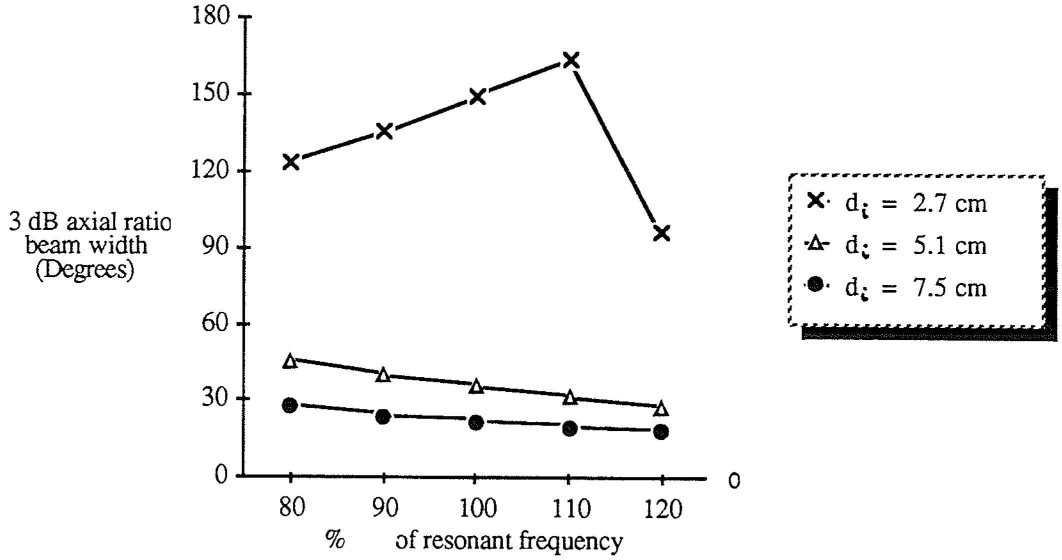

Figure 4.24 3 dB axial ratio beamwidth in the main beam for d_i = 2.7, 5.1 and 7.5 cm. in the $\phi = 0°$ plane using the 0°, 90°, 180°, 270° feeding pattern

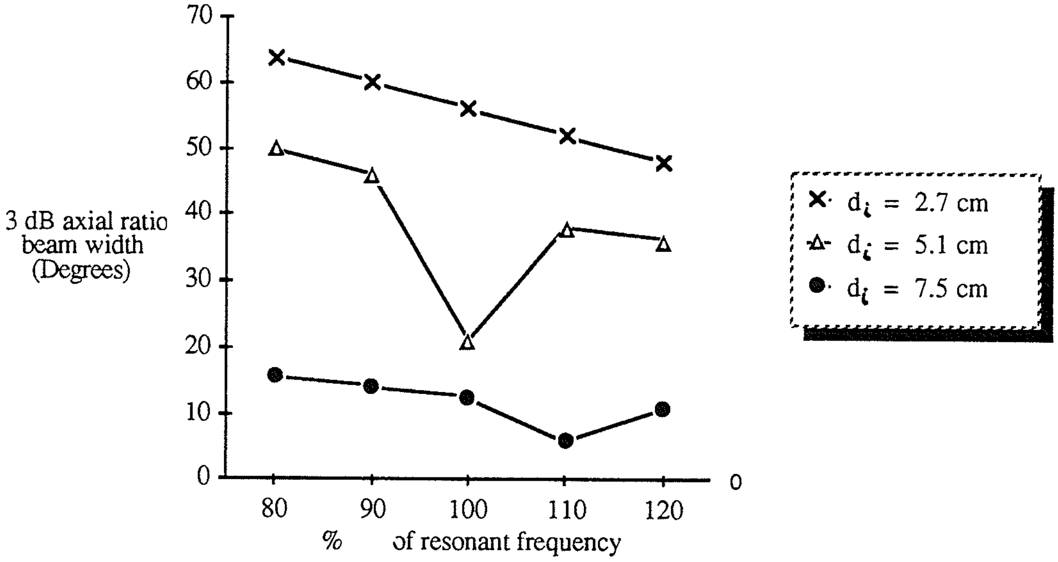

Figure 4.25 3 dB axial ratio beamwidth in the main beam for d_i = 2.7, 5.1 and 7.5 cm. in the $\phi = 45°$ plane using the 0°, 90°, 180°, 270° feeding pattern

4.6 Discussion

In all cases, the radiation pattern for the feeding arrangement 0°, 90°, 0°, 90°, has a null in the boresight direction, while for the 0°, 90°, 180°, 270° feed pattern, it has a maximum. The reason for the null in the former arrangement is that the elements spaced 180° apart will have field components oppositely directed because of the 180° difference in their orientation, resulting in cancellation. In the latter arrangement the 180° difference in orientation will be nullified by the 180° difference in the input rf, and the result is constructive interference.

In the principal plane, for $d_i = .284\lambda_0$, the latter feeding arrangement gives near-perfect circular polarization, while in the ϕ=45° plane it has a 3 dB axial ratio beamwidth of approximately 50°.

In the principal plane, the axial ratio for the 0°, 90°, 0°, 90° feeding arrangement is infinite for all values of d_i, while it is good for a range of θ away from the boresight in the ϕ=45° plane. As d_i, increases, the axial ratio in the ϕ=45° plane improves towards the boresight, and the range of θ off the boresight, over which it is acceptable increases.

As d_i is increased, for the 0°, 90°, 180° 270° feeding arrangement, the main beamwidth decreases, and sidelobes begin to appear. Both the main beam and the sidelobes are circularly polarized. In the ϕ= 0° plane, the sidelobes have the same sense of circular polarization as the main beam, while in the ϕ=45° plane, the sense is opposite. In all cases however, the range of θ over which the axial ratio is satisfactory is very small for the sidelobes. For the 0°, 90°, 0° 90° feeding arrangement, there is a null at θ = 0° in both the ϕ=0° and ϕ=45° planes. In the ϕ=0° plane, as d_i is increased symmetric nulls appear on either side of θ=0°.

In terms of the axial ratio, the experimental results compare well with the theoretical results. At any given angle, the axial ratio for the experimental data can be determined by noting the extent of the local swings in the pattern.

Discrepancies between the theoretical results may be in part accounted for by noting that the four patches in the experimental set up did not match perfectly, resulting in more power to some of the patches. For an azimuth (θ) of 0°, the axial ratio should be identically zero (i.e. a smooth curve in the radiation pattern with no local swings), for both ϕ=0° and ϕ=45° in the 0°, 90°, 180°, 270° feeding arrangement. For these angles, in the $d_i = .28\lambda_0$ case, the axial ratio is measured to be approximately 2 dB. It is satisfying to note however that in the ϕ=45° plane for the ϕ=0°, 90°, 0°, 90° feeding arrangement the axial ratio as measured experimentally decreases to 0 dB, for a certain value of θ off of boresight, for all values of d_i, as expected. It is also noted that for large values of θ the existence of a finite ground plane will cause discrepancies between the measured and theoretical radiation patterns.

Although the shapes of the theoretical and experimental radiation patterns agree in general, the absolute values of given points on the patterns do not. In addition to the possibility of unmatched elements, the discrepancy may be in part explained by the rotating linear measurement set up. The transmitting antenna used to generate the test signal to be measured by the circular array under test is a linearly polarized element. If the circular array is set up to transmit (and by reciprocity receive) circularly polarized waves, the power it will receive will be one half of the available power, or 3 dB down. Thus the absolute value of the power received for regions of near perfect circular polarization in the experimental data will be 3 dB above the indicated value. In addition, the network used to generate the two different feeding patterns introduces a loss of between 1.0 and 1.4 dB. The return loss due to mismatched elements is in the range of .2 to .3 dB. These factors will account for a difference between measured and theoretical gain values of between 4.2 and 4.7 dB for a perfectly circularly polarized wave. For example in Fig. 4.8 a), for which ϕ = 0°, the peak gain is given to be 1.84 dB. Accounting for these factors results in a gain of between 6 and 6.7 dB. The theoretical gain is approximately 7 dB. In Fig. 4.8 c), for which $\phi = 45°$, the peak gain is 2.13 dB. Accounting for the power losses gives a value of between 6.3 and 6.8 dB, within .7 dB of the theoretical gain of 7 dB.

Figure 4.13 shows results which are identical to Fig. 4.9 in the $\phi=0°$ plane. In the $\phi=45°$ plane however the two figures differ greatly. The eight element array (Fig. 4.13), shows a very wide range of near acceptable (< 4 dB) circular polarization for a beamwidth of 80°.

Figures 4.16 to 4.18 show a tendency for the main beamwidth to decrease as the frequency is increased. The peak value of the main beam increased with frequency for two of the three values used for d_i. Figure 4.18 shows the existence of a sidelobe in the $\phi = 45°$ plane which increases in magnitude as frequency increases. The beamwidth is insensitive to changes in frequency, while the position of the sidelobe was found to gradually tend towards the main beam. Since this sidelobe is circularly polarized in the opposite sense to the main lobe, the result is an increasing axial ratio. Figure 4.19 indicates significant sidelobes in both the $\phi = 0°$ plane (where it is in the opposite sense to the main beam), and the $\phi = 45°$ plane (where it is in the same sense as the main beam). In the $\phi = 0°$ plane, the sidelobe beamwidth is decreasing as the peak value of the sidelobe moves towards the main beam. These effects tend to cancel, with the result that the sidelobe of circular polarization in a sense opposite to that of the main beam, will not overlap the main beam and the axial ratio remains low as frequency increases. In the $\phi = 45°$ plane the sidelobes have the same sense of circular polarization as the main beam, and the encroachment of these lobes on the main beam will not affect the axial ratio. Figures 4.24 and 4.25, show that the best circular polarization is obtained for small values of d_i, while there is a tendency for the range of acceptable axial ratio to decrease with increasing frequency.

Chapter 5

Conclusions and Recommendations

5.1 Conclusions

The arrangement of four or more linearly polarized elements in a circular array with a phasing arrangement in the feeding of the elements of 0°, 90°, 180°, 270°, or 0°, 90°, 0°, 90° provides a good means of generating circularly polarized waves. By selecting the feeding pattern it is possible to steer the angular range of satisfactory axial ratio, and the direction of power flow away from the array.

5.2 Recommendations

The antenna array should be tried with different configurations (more elements, different phasing arrangements etc.), and investigated for improved axial ratio, and beam width.

References

[1] Wheeler, Harold A: 'Transmission Line Properties of Parallel Wide Strip by a Conformal Mapping Approximation', IEEE Transactions on Microwave Theory and Techniques, pp 280-289, May 1964

[2] James, J.R., Hall, P.S. and Wood, C.: 'Microstrip Antenna. Theory and Design', Peter Penguins Limited, pp 24, 68, 69, 104, 283, 1981

[3] Wolff, Ingo and Knoppik, Norbert: 'Rectangular and Circular Microstrip Disk Capacitors and Resonators', IEEE Transactions on Microwave Theory and Techniques, vol MTT-22, pp 857-864, 1974

[4] Bhattacharyya, Arun K, and Garg, Ramesh: 'Input Impedance of Annular Ring Microstrip Antenna Using Circuit Theory Approach', IEEE Transactions on Antennas and Propagation, Vol Ap-33, pp 369-374, 1985

[5] Huang, John: 'A Technique for an Array to Generate Circular Polarization with Linearly Polarized Elements', IEEE Transactions on Antennas and Propagation, Vol AP-34, pp 1113-1124

[6] Harrington, R.R.: 'Time Harmonic Electromagnetic Fields', McGraw-Hill Book Company, pp 106-108, 1961

[7] Yano, Sazanimi and Ishimaru, Akira: 'A Theoretical Study of the Input Impedance of a Circular Microstrip Disk Antenna', IEEE Transactions on Antennas and Propagation, Vol Ap-29, pp 77-83, 1989

[8] Dearnley, Russell W and Bard, Alain R.F.: 'A Broad-Band Transmission Line Model for a Rectangular Microstrip Antenna', IEEE Transactions on Antennas and Propagation, Vol Ap-37, pp 6-15, 1989

[9] Shen, Liang C: 'The Elliptical Microstrip Antenna with Circular Polarization', IEEE Transactions on Antennas and Propagation, Vol Ap-29, pp 90-94, 1981

[10] Collin, Robert E.: 'Antenna Theory Part 1', McGraw-Hill Book Company, 1969

[11] Schaubert, D.H., Farrar , F.G., Sindoris, A.R. and Hayes, S.T.: 'Microstrip Antennas with Frequency Agility and Polarization Diversity', IEEE Transactions on Antennas and Propagation, Vol Ap-29, pp 118-123 1981